5-2012

Damage Detection in Metamorphic Stone Blocks Utilizing Impact-echo Testing and Modal Analysis

Alexander C. Jording
University of Nebraska Lincoln, alexjording@gmail.com

DAMAGE DETECTION IN METAMORPHIC STONE BLOCKS

UTILIZING IMPACT-ECHO TESTING AND MODAL ANALYSIS

by

Alexander Charles Jording

A THESIS

Presented to the Faculty of

The Graduate College at the University of Nebraska

In Partial Fulfillment of the Requirements

For the Degree of Master of Science

Major: Architectural Engineering

Under the Supervision of Associate Professor Ece Erdogmus, PhD

Lincoln, Nebraska

May, 2012

DAMAGE DETECTION IN METAMORPHIC STONE BLOCKS

UTILIZING IMPACT-ECHO TESTING AND MODAL ANALYSIS

Alexander Charles Jording, M.S.

University of Nebraska, 2012

Adviser: Ece Erdogmus

Existing buildings decay with the passage of time, and as a result, continually require maintenance or rehabilitation. When considering existing structures, testing is often necessary to complete structural analysis in preparation for rehabilitation or repair. Non-destructive testing provides a structural assessment method applicable to a variety of materials and structures. The hypothesis of this research is that impact-echo testing, one of the many NDT techniques, can be adopted to develop a reliable and standardized method to assess the condition of rectangular metamorphic stones. After the baseline material parameters and general response to impact-echo testing were established, a novel method to perform real-time on-site block assessments was developed. The methodology is developed using an international research project at Antiochia ad Cragum, near present-day Gazipaşa, Turkey, as a case study for structural assessment conditions. Blocks from the 3rd century Imperial Roman temple at Antiochia ad Cragum, serve as the primary reference for this study. Theoretical values based on eigenvalue analysis when compared with finite element analysis results provided a correlation to within 2.4%. Frequencies from impact-echo testing from a sample block cast out of a similar density material are compared with theoretical eigenvalue analysis values, resulting in errors of

less than 6%. As a result of this research, existing impact-echo methods have been validated for applicability on metamorphic stones and mortar blocks. Furthermore, a real-time impact-echo analysis program has been developed to assess stones and characterize their structural integrity simultaneously. These findings will benefit engineering and archaeological research teams wishing to evaluate rectangular stones. In addition, these techniques and methods, with minimal alteration, can be applied to a variety of materials including other types of stone, concrete, and even wood.

This thesis is dedicated to my family for their encouragement and love ad infinitum.

Acknowledgments

Thank you to my family who has been a constant support throughout my life, especially during my graduate studies. Thank you to my wife, Hanna, for her continued support and encouragement throughout the last 9 years. Thank you to those members of my family for their financial support in my education: Mom, Dad, and Grandma and Grandpa Jording.

Thank you to my professors and mentors at the University of Nebraska for sharing their knowledge and advice with me: Dr. Ece Erdogmus for her support in my academic career and for the research opportunities she has provided during my time at the University of Nebraska; Dr. Teri Norton for her knowledge, support, and advice in and out of the classroom. A special thanks to Kelvin Lein for his help in the lab at the University of Nebraska, who provided assistance in the completion of the laboratory testing. Thank you to my professors and friends at the University of Wyoming for their support during my undergraduate years and their continued support as I explored graduate studies at the University of Nebraska; Dr. Anthony Denzer for his continued support, advice, friendship, and unwavering dedication to my success as a student and a person; Dr. Thom Edgar for his support and friendship in and out of the classroom; Tyler Robison for his continued support and friendship.

Thank you to my friends and research partners at the University of Nebraska who aided in the completion of this research. In particular, I want to thank Cody Buckley, Andy Rudeen, and Catherine Armwood for their assistance and advice. In addition, thanks to Sara Robbins and Sean Kirker who are tasked with the continuation of this

study. My thanks those who will implement the methods developed in this study, providing useful information for the preservation effort at Antiochia ad Cragum.

This research was partially funded by a National Science Foundation grant (Award #0623660). Thank you to the National Science Foundation for their financial support in the endeavors of University of Nebraska to further the preservation of Antiochia ad Cragum and its place in the history in the rough Cilicia region of Turkey.

Table of Contents

List of Figures

List of Tables

List of Equations

Chapter 1: Introduction and Background

Non-destructive testing (NDT) is currently utilized by many engineering companies to assess the condition of existing structures, but it has also become increasingly popular in new construction due to its discreet application for quality control measures. NDT can determine some of the characteristics of a structure or structural member without causing damage. This benefit makes NDT a very appealing solution for conducting analysis on historical structures.

Currently there is a restoration effort underway near Gazipaşa, Turkey, with the objective of reconstructing and restoring a 3rd century ancient Roman temple. The temple has experienced complete collapse and is currently under archaeological excavation and evaluation, with the ultimate goal of a partial reconstruction.

Figure 1: Temple Block Field at Antiochia ad Cragum

Figure 1 illustrates the project site where main building stones for the temple have been documented and moved into block fields for further study. These stones have varying flaws, voids, and discontinuities ranging from hairline cracks to large cross-sectional fractures. In order to progress with the restoration, the stones need to be evaluated for their structural integrity to determine the need for structural rehabilitation. After reviewing multiple NDT techniques, impact-echo was chosen as the most promising NDT technique for evaluation of these stones due to its low cost and its availability to the project team. The purpose of this research is to evaluate the effectiveness of impact-echo testing and develop a system to categorize the stones in reference to their structural integrity. Once completed, it is believed that this research will provide a novel in-situ assessment method for the structural analysis of all of the temple's stones. The condition assessment of the stones can then be used in the design of the strengthening methods to be used for the blocks and eventually the design of the reconstruction of the temple. The broader impact of the assessment methods developed here and to the temple project is future application of the method to numerous complex excavation sites around the world.

1.1 Objectives

The ultimate goal of this research is to develop an effective, non-destructive evaluation technique to determine the structural integrity of historic metamorphic stone blocks (limestone, marble, etc…). The research can be broken down into the following objectives:

1. Compile an understanding of the field conditions of typical historic building stones
2. Determine which non-destructive testing (NDT) method will be most applicable
3. Correlate selected NDT method with theoretic results in order to determine their applicability to metamorphic stones
4. Develop a reliable NDT setup
5. Develop a tool for real-time analysis of stones

Once accomplished, these objectives will provide a thorough evaluation of the hypothesis following accepted experimental methodologies.

1.2 Thesis Overview

Chapter 1 includes the introduction, background information, and research objectives. A literature review including the different methods used for analysis and NDT is included in Chapter 2. Chapter 3 discusses the research methods and details regarding experiments and analyses particular to this study. Results and discussion are presented in Chapter 4. Conclusions and recommendations for future work are presented in Chapter 5.

Chapter 2: Literature Review

This section presents a review of the literature regarding the use of non-destructive testing (NDT). In particular, the processes and methodologies of impact-echo testing are reviewed. Impact-echo testing was determined to be the testing method of choice due to its availability, practicality in the field, and low cost. Additionally, eigenvalue analysis and modal analysis are discussed.

2.1 Impact-Echo Testing

Impact-echo testing uses impact generated stress waves and their propagation to examine the characteristics of various materials and their associated interaction. The impact-echo method is a knowledge-intensive method requiring the user to understand all aspects of the method. In order to correctly analyze and interpret the results, the user must understand stress waves and their propagation, frequency analysis, wave speed, and the hardware and software being used in testing.

Impact-echo testing has proven to be a reliable method of determining voids, honey-combing, and delaminations in both concrete and masonry (Sansalone & Streett, 1997). The impact-echo method consists of the introduction of a mechanical impact to the specimen creating a stress wave. This stress wave is reflected by internal voids or external surfaces. The reflected stress waves cause displacements on the surface of the specimen. These displacements are measured and recorded with respect to their time and eventually get transformed into the frequency domain by a data acquisition system, often a signal analyzer. From this information, the structural integrity of the specimen can be

obtained by observing predominant frequencies displayed by the specimen (Sansalone & Streett, 1997). A schematic representation of this process is shown in Figure 2.

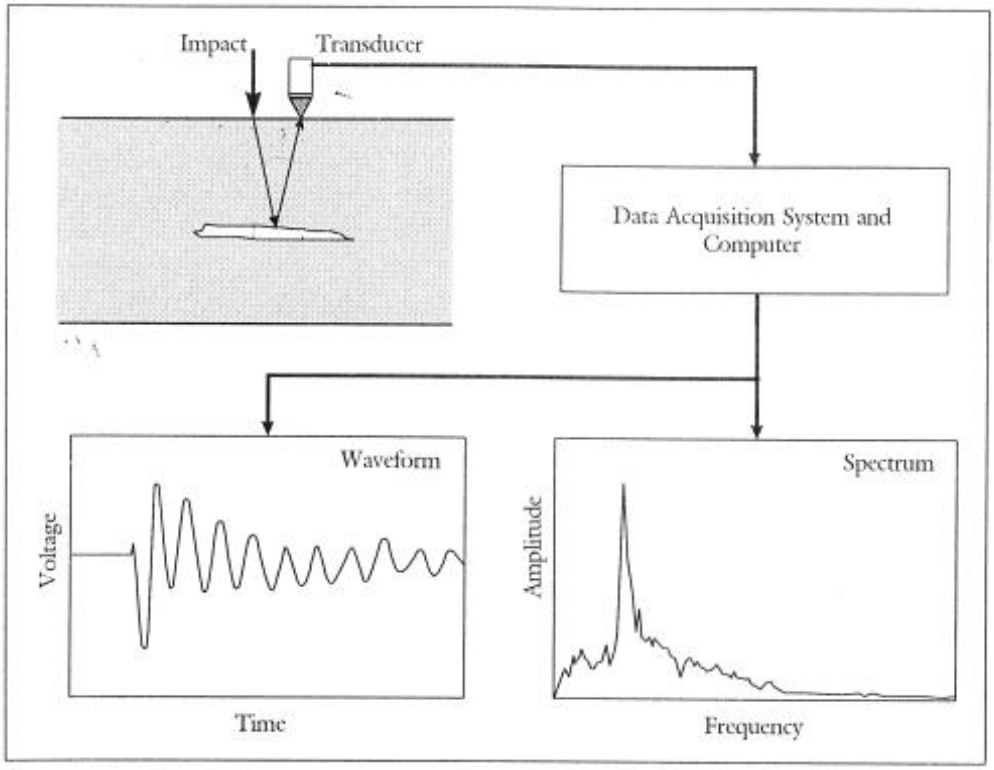

Figure 2: Simplified diagram of the impact-echo method (Sansalone & Streett, 1997)

2.1.1 History of Impact-Echo Testing

The impact-echo method originally developed by Carino and Sansalone was successful due to four breakthroughs in the 1980's. First, the computer simulated analysis using finite-element analysis allowed for a better understanding of stress waves and their behaviors. Second, a reliable method of generating precise stress waves aided in the analysis needed for impact-echo testing. This came by the use of steel ball bearings. Ball bearings provided reliable and predictable contact times and subsequently reliable frequencies (Sansalone & Streett, 1997).

The next key development that allowed for the success of the impact-echo method was the invention of more advanced displacement transducers. The precise nature of impact-echo testing required a very sensitive transducer that would respond accurately to minimal displacements. Use of piezoelectric elements, including an intricate circuit to record displacements in the form of voltage, while keeping them proportional resulted in transducers with adequate sensitivities. The last important development was the use of Fourier transform methods allowing for the transfer of time-domain data to the frequency domain. When data is presented in the time-domain, analysis is very difficult to interpret. This transformation allows for analysis of the amplitude and frequency of multiple reflections (Sansalone & Streett, 1997). After these key advancements, Carino and Sansalone developed and refined the impact-echo method at the Cornell University. Later, Sansalone and Streett published the book *Impact-Echo: Nondestructive Evaluation of Concrete and Masonry*, which serves as a general guide for impact-echo researchers and users.

2.1.2 Stress Waves

The three wave types associated with impact-echo testing include P-waves, S-waves, and R-waves. Figure 3 provides a graphic representation of these waves traveling through a medium.

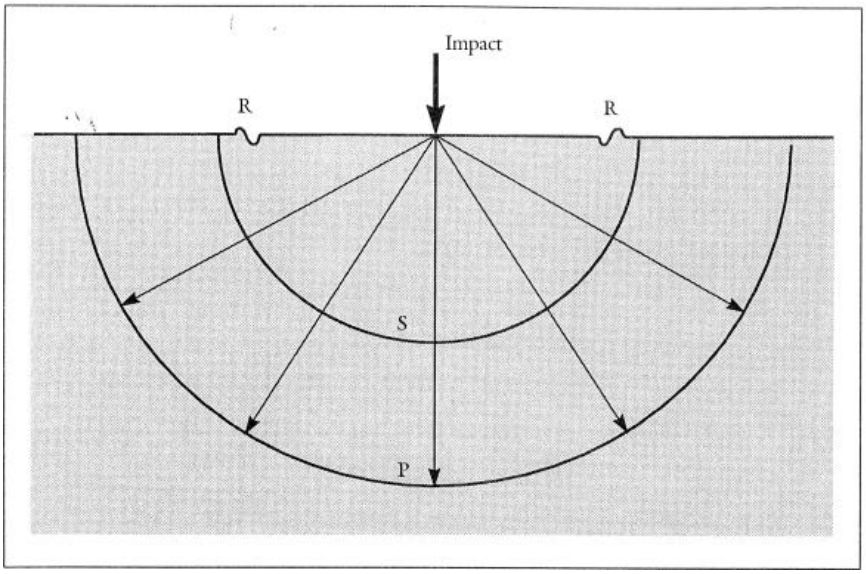

Figure 3: Graphical representation of stress wave propagation

S-waves produce motion perpendicular to the direction of wave propagation while R- waves travel along the surface (Carino, 2001). As Figure 4 illustrates, P-wave displacements measured by the transducer are maximum nearest to the point of impact while S-waves are minimal. This location is ideal for the measurement of P-wave displacements while minimizing S-wave effects. As a result, the ideal location for the transducer and point of excitation (i.e. the location of wave propagation), in an impact-echo test, are adjacent to one another minimizing S-wave effects and maximizing P-wave effects (Sansalone & Streett, 1997).

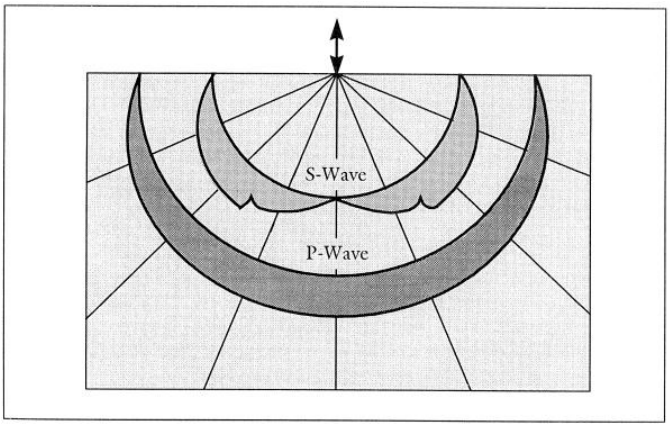

Figure 4: Relative amplitudes of particle displacements produced by a harmonic point source (Sansalone & Streett, 1997)

Wave speeds may be calculated assuming a homogenous, isotropic, and elastic solid given adequate space and surface conditions. The equations for P-wave and S-wave velocities are shown in Equations 1 and 2, respectively (Krautkramer & Krautkramer, 1990):

$$C_p = \sqrt{\frac{E(1-\nu)}{\rho(1+\nu)(1-2\nu)}} \qquad \text{Equation 1}$$

$$C_s = \sqrt{\frac{E}{2\rho(1+\nu)}} \qquad \text{Equation 2}$$

where,

C_p = P-wave velocity,
C_s = S-wave velocity,
E = Young's modulus of elasticity,
ρ = mass density, and
ν = Poisson's ratio.

All of these stress waves (P, S, and R) also follow the basic wave principle of:

$$C = f\lambda \qquad \text{Equation 3}$$

where,

C = wave velocity,
f = frequency, and
λ = wavelength.

The reliability of determining voids and flaws depends on the ability to observe them. In order to observe a flaw or void, the wavelength, λ, must be equal to or less than the length of the flaw (Sansalone & Streett, 1997). Equation 3 can be utilized to calculate a wavelength (*λ), based on C (wave speed) and f (frequency), so that the user is aware of the minimum flaw length that will be detected.*

As opposed to directly calculating P-wave speeds based on material properties, P-wave speeds may also be determined by direct measurement. The procedure for measuring the wave velocity is to place transducers a known distance, L, away from each other. Then introducing a stress wave and measuring the times at which accelerometers encounter the P-wave. This testing setup can be seen in Figure 5 while sample P-wave measurements can be seen in Figure 6. ASTM C1383-04 stipulates that two accelerometers be placed 300mm apart in a "spacer device", and the point of impact or excitation is at a minimum 150mm ±10mm from the first accelerometer (ASTM

International, 2010). Following the guidelines provided in ASTM C1383-04, C_p can be calculated using Equation 4:

$$C_p = \frac{L}{t_2 - t_1} \qquad \text{Equation 4}$$

where,

C_p = P-wave velocity
L = distance between transducers, and
t_1 and t_2 = arrival times at corresponding transducers.

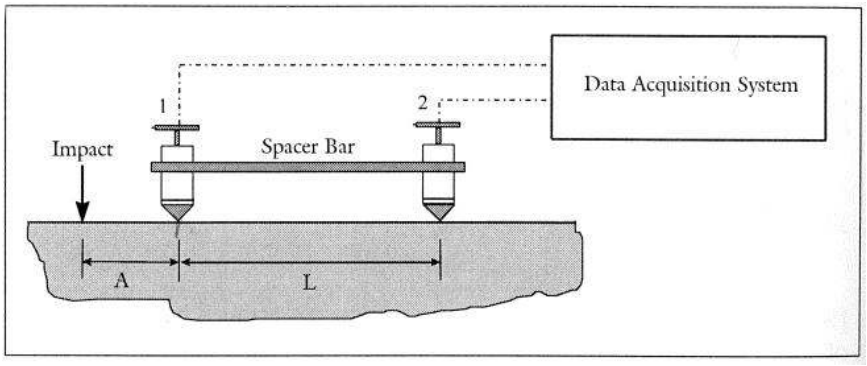

Figure 5: Schematic representation of straight-line velocity test set-up for wave speed measurements (Sansalone & Streett, 1997)

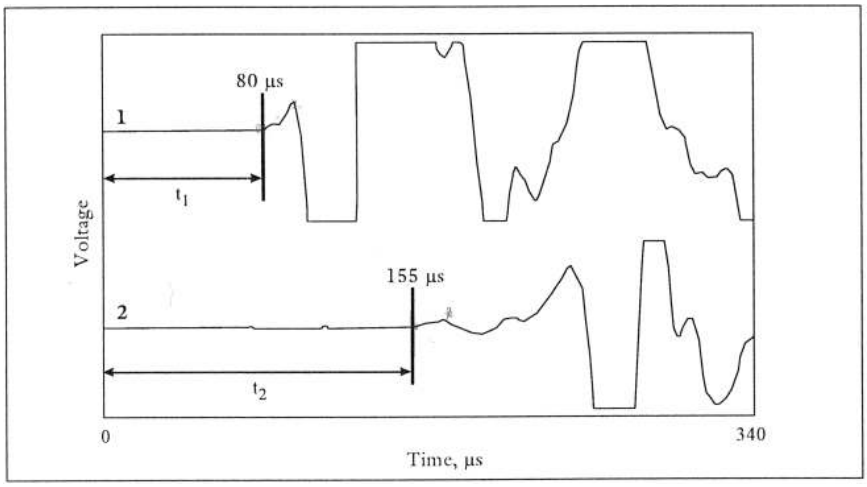

Figure 6: Example waveforms for straight-line velocity wave speed calculations (Sansalone & Streett, 1997)

As P-waves travel throughout the specimen they reflect on internal flaws and external surfaces. As a result, the impact-echo method is beneficial in that it only requires access to one side of the specimen. The travel time and frequency can be computed by the following equations:

$$t = \frac{2D}{C_p} \qquad \text{Equation 5}$$

$$f = \frac{1}{t} \qquad \text{Equation 6}$$

where,

t= elapsed time for reflection of one P-wave
D= distance to internal defect or opposite face
C_p= P-wave speed
f = frequency

Combining Equation 5 and Equation 6 and adding a shape correction factor yields the fundamental equation for impact-echo:

$$f = \beta \frac{C_p}{2D}$$ Equation 7

The variable β represents the shape factor correction, which corresponds to varying dimensions of specimens. The shape factor, β, will be discussed further in section 2.1.5 while reviewing the spatial considerations related to impact-echo testing.

One important safeguard in dynamic testing is ensuring that the accelerometers/transducers used are never exposed to vibrations beyond their resonant frequency (Carino, 2001). This important safety measure ensures that the testing equipment is not damaged. In order to know what ranges of frequencies are being excited in an impact-echo test, it is necessary to know the excitation frequency range.

The excitation frequency range of a dynamic test can be calculated by observing the Fourier transform of the force-time curve of the impact force. In order to adequately excite a particular frequency range, the Fourier transform must be limited to at least 1.25 times the highest desired frequency. This is done by taking the maximum excitation frequency (the value where the FFT approaches 0) and dividing it by 1.5. This will give the contact time. Then 1.25 is divided by the contact time to achieve the reliable frequency range (Sansalone & Streett, 1997). The shaded portion of Figure 7 depicts the reliable frequency range.

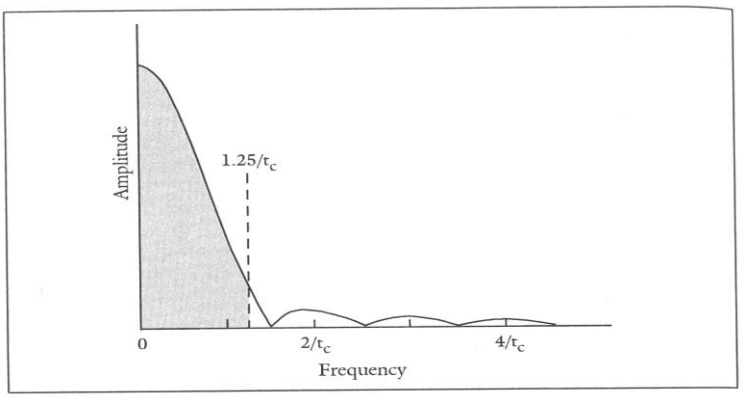

Figure 7: Fourier transform of an elastic impact curve

Shorter force contact durations create higher useful frequency ranges while long contact times produce lower useful frequency ranges (Chopra, 2007).

2.1.3 Impact-Echo Instrumentation

Impact-echo hardware varies greatly between companies, but the general principles of impact-echo testing still apply. When conducting dynamic testing, it is necessary to normalize the vibration generation and the amplitude of excitation (Tuan, 2004). Normalizing impacts in impact-echo testing is often done by spring-rod displacement, where a small metal sphere is displaced a certain distance on a metal rod and released. When using impact hammers for excitation often times they are equipped with a load cell to normalize the impact response (Sridharan, Muralidharan, Balasubramaniam, & Krishnamurthy, 2006).

Accelerometers are the other main part of impact-echo instrumentation. Accelerometers must provide adequate frequency ranges and adequate sensitivities. If an accelerometer is not sensitive enough to record small variations, an accelerometer with higher sensitivities would be required. This same concept works in reverse as well. If an

accelerometer is too sensitive to the excitation provided it will overload and create erroneous data. The specific mounting technique of an accelerometer can affect how sensitive it is as well (PCB Piezotronics, 2002).

Various mounting techniques are available for attaching accelerometers to the specimen including magnetic mounts, mounting pads, and stud mounting. Due to the sensitive nature of the some projects, non-damaging adhesive mounting is often chosen as the mounting technique of choice (Erdogmus, Boothby, & Smith, 2007).

2.1.4 Frequency Analysis

In the time domain, analyses of waveforms are often difficult due to their complexity. The complexity arises primarily from the reflections on multiple surfaces, interfaces, and flaws causing displacements of varying frequencies and amplitudes. In order to analyze the data, the time-domain data is converted using Fourier transforms to sum the sine curves with varying amplitudes and frequencies (Figure 8a). This Fourier transform then renders an amplitude spectrum similar to Figure 8b (Sansalone & Streett, 1997).

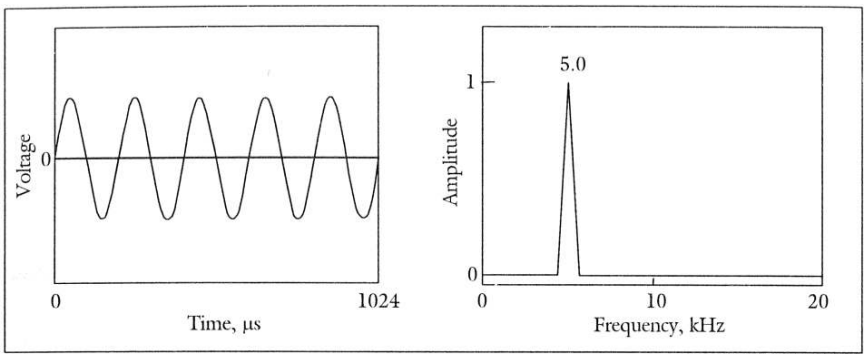

(a) (b)

Figure 8: (a) Waveform consisting of a simple sine wave, and (b) the corresponding amplitude spectrum (Sansalone & Streett, 1997)

With the use of digital signal analysis media, Fourier transformations are executed by the software using a technique known as Fast Fourier Transform, FFT (Sansalone & Streett, 1997).

2.1.5 Digital Signals

Impact-echo testing results are typically described by surface displacement, in the form of accelerations, instead of time graphs. This result is not a direct measurement, but is computed by a signal analyzer, which converts the analog voltages recorded by the transducer/accelerometer from analog to digital. This data is used in frequency analysis and can be converted with a FFT to obtain amplitude spectrums.

There are two main parameters that must be considered when acquiring data: sampling interval and the number of samples recorded. The sampling interval determines the maximum frequency that can be observed in a waveform. In order to obtain the sampling interval, Equation 6 must be reciprocated. Sansalone and Streett (1997) recommend a sampling interval that is twice the reciprocal of the maximum frequency to

be observed. Obtaining more accurate results requires the use of higher sampling intervals. Ideally, a minimum of 10 samples per cycle, at the highest frequency of interest, should be used to limit error.

The number of samples recorded is the number of times in a test that data is gathered. Often times, the number of samples recorded are a function of record length and frequency resolution within a signal analyzer. Record length determines the total time in which signals are being received by the transducer and recorded. Frequency resolution is the difference between samples in the amplitude spectrum, often in units of hertz (Sansalone & Streett, 1997). It is impossible to specifically choose frequency resolution, number of samples, or sampling interval independently based on the needs of the experiment as they are all related to one another and often limited by the signal analyzer's capability. For example, the number of samples is dependent on the sampling rate and the frequency range measured. In addition, the frequency resolution is dependent on the number of samples and the frequency range. When conducting impact-echo tests, choosing the frequency range is often the deciding parameter, while the number of samples is limited by the signal analyzer, therefore fixing most of the remaining parameters.

2.1.6 Spatial Considerations

Elements of varying cross-sectional properties with bar-like qualities respond uniquely to the reflection of stress waves. Bar-like qualities include specimens of approximately square cross-sections of which the length is approximately 3 times the largest cross-sectional dimension. During impact-echo testing, various modes of

vibration are excited. In circular and square cross sections of bar-like specimens, these modes of vibrations are unique in that they represent the characteristic cross-sectional modes of vibration rather than the typical flexural modes of vibration observed in typical impact-echo/modal analysis. These modes of vibration become apparent with the requirement that the length of the element is at least three times the largest dimension of the cross-section (bar-like) (Sansalone & Streett, 1997).

As previously stated in Equation 7, the vibration response observed in bar-like structures is dependent on β, the shape factor. In elements with rectangular cross-sections, similar to the marble stones of this study, β is a function of the depth to breadth aspect ratio. This aspect ratio can be described as D/B with D referring to the dimension of the face parallel to the direction of impact, and B referring to the dimension of the face of impact as seen in Figure 9.

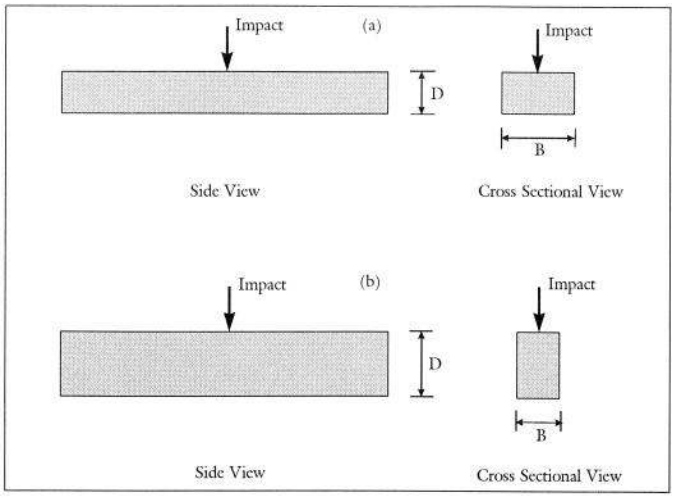

Figure 9: Impact-echo test orientation on a beam: (a) impact in the direction of the shorter cross-sectional dimension; (b) impact in the direction of the longer cross-section dimension (Sansalone & Streett, 1997)

Through past experimental data, it has been determined that the cross-sectional modes of vibration are dominant within a range of 0.6 to 2.0 for the D/B ratio. At aspect ratios smaller than 0.6 the specimen begins to display some plate-like behaviors, where a predominant frequency correlating to the thickness of the specimen dominates the response. At an aspect ratio of 2.0, the specimen begins to behave more like a rod, where vertical flexural modes of vibration can dominate the response (Sansalone & Streett, 1997). Spatial variation between different specimens compelled Sansalone and Streett to conduct a parametric study of varying aspect ratios by eigenvalue analysis.

Eigenvalue analysis, which will be discussed in section 2.2, as it relates to specimens with aspect ratios varying from 0.6 to 2.0, has allowed for a more concise presentation of the predicted modes of vibration. Table 1 is based on values from Sansalone and Streett (1997) and lists the equation for the fundamental mode of vibration and the coefficients required to obtain the next five expected modes of vibration for a specific D/B ratio. The corresponding shape factor is also included. The following five expected modes of vibration are calculated by multiplying the fundamental mode by a designated coefficient, while the fundamental mode frequency can be calculated using Equation 7. These coefficients vary for each mode within a specific D/B ratio. These expected modes of vibration allow for comparison with the experimental values.

Table 1: Relationships for calculating the frequency of the fundamental modes and the next five higher mode frequencies for rectangular structures with cross sections between 0.6 and 2.0 (Sansalone & Streett, 1997)

Aspect Ratio (D/B)	β	Fundamental Mode	Mode 2 Coefficient	Mode 3 Coefficient	Mode 4 Coefficient	Mode 5 Coefficient	Mode 6 Coefficient
0.60	0.84	$f_1 = \beta \frac{C_p}{2D}$	1.07	1.43	1.48	1.86	1.91
0.75	0.87		1.19	1.6	1.66	1.98	2.02
0.80	0.75		1.45	1.96	2.01	2.41	2.46
0.83	0.77		1.44	1.94	1.98	2.38	2.44
0.87	0.8		1.43	1.93	1.95	2.36	2.41
0.91	0.82		1.42	1.92	1.92	2.34	2.47
1.00	0.87		1.41	1.9	2.45	2.83	2.34
1.10	0.9		1.43	1.92	2.34	2.52	2.69
1.20	0.92		1.45	1.94	2.38	2.58	2.73
1.33	0.94		1.49	1.98	2.02	2.45	2.62
1.67	0.95		1.66	2.11	2.32	2.74	2.74
2.00	0.96		1.81	2.06	2.23	2.56	2.92

The variation in the frequency response and the corresponding modes of vibration can be used to detect flaws and determine the general internal characteristics of a specimen. Flaws in rectangular cross sections are characterized by four main results (Sansalone & Streett, 1997).

1. *Reduced amplitudes of the initial cross-sectional modes of vibration:*

   Corresponds to a general loss of stiffness in the specimen reflecting the presence of an internal flaw or flaws. As seen in Figure 10, the altered response of the section with a void depicts an unexpected low frequency peak at 4.4 kHz (#1) and an unexpected high frequency peak at 12.7 kHz (#2).

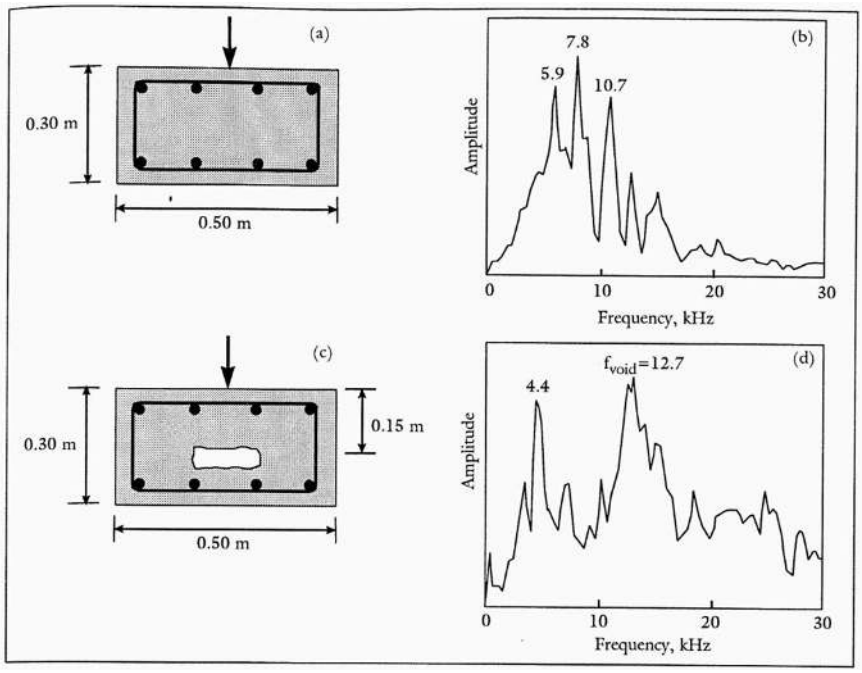

Figure 10: Impact-echo response of a rectangular beam: (a) and (b) solid cross-section with an aspect ratio of 0.6, and (c) and (d) cross-section containing a void (Sansalone & Streett, 1997)

2. *Unexpected modes of vibration with higher peak frequencies*

   Corresponds to continued P-wave reflections in a specimen typically resulting from a surface flaw/delamination, a shallow internal flaw, or honeycombing in concrete. Figure 11 shows a specimen with honeycombing and its associated response spectrum.

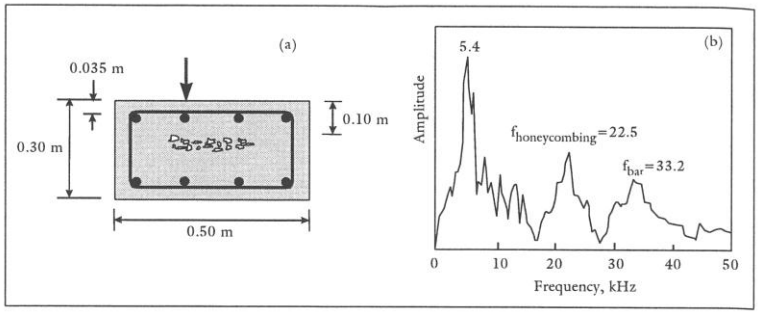

Figure 11: (a) Concrete cross-section with honeycombing and the associated (b) impact-echo response spectrum (Sansalone & Streett, 1997)

3. *Expected high frequency mode shapes disappear*

   Corresponds to those modes not being excited due to higher damping or general lack of stiffness

4. *Unexpected low-frequency peaks*

   Corresponds to a thin layer above a flaw or a delamination that is responding with a flexural mode of vibration. An example of a thin delamination can be seen in Figure 12.

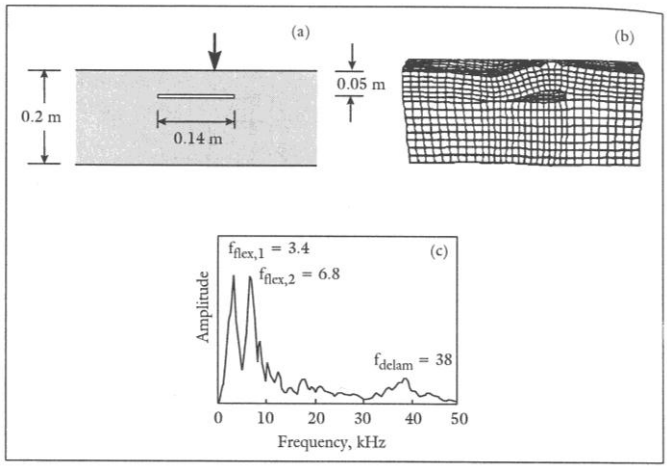

Figure 12: Impact-echo response of a flexural mode of vibration response: (a) thin delamination in a slab, (b) finite element model, (c) amplitude response spectrum (Sansalone & Streett, 1997)

Any one of these results can reflect voids or flaws in the specimen, however all are subject to interpretation. Thus, while a general understanding of the condition of the specimen can be gathered using impact-echo, it may need to be combined with other methods for studies where accuracy in type of flaw is desired.

2.2 Various Past Research Utilizing Impact-Echo Methods

Impact-echo instrumentation has been used in many different applications with varied success. Recently, impact-echo testing has been used in conjunction with chain-dragging, thermal image scanning, and ground penetrating radar to inspect bridge decks. Impact-echo testing has also been used to detect flaws in concrete cubes and internal grouted ducts in concrete beams.

A study for the Wyoming Department of Transportation utilized multiple techniques including impact-echo testing to determine the delamination in bridge decks across the state of Wyoming. In this particular study, impact-echo testing was conducted on bridge decks in a grid where the results were mapped and correlated to other testing methods. The other methods utilized in this study included chain-dragging, thermal image scanning, and ground penetrating radar. It was Robison's conclusion that impact-echo testing was a vigorous testing method and provided more detailed delamination results than any other technique, but it was more time demanding for such a large specimen (Robison, 2010).

Another study utilizing impact-echo testing methods, measured the responses of concrete cubes when subjected to excitation. This particular study focused on the

changes in the cross-sectional vibration response spectrums when flaws were present in concrete cubes. The study utilized finite element analysis (FEA) and eigenvalue analysis to evaluate the concrete cubes prior to impact-echo testing. In addition, this study utilized impact-echo equipment to determine P-wave speeds in the concrete cubes. This study concluded that both FEA and eigenvalue analysis provided similar results to impact-echo testing. Furthermore, this study verified the flaw detection recommendation, provided by Sansalone and Streett (1997), that internal flaws will shift the response spectrum and create a higher frequency peak at the depth of the flaw (Hsiao, Cheng, Liou, & Juang, 2008).

One more recent study utilized impact-echo testing and FEA to determine the grouting characteristics of ducts in concrete structures. In this particular study, grouted and ungrouted ducts were placed into a large concrete beam and tested. The authors utilized a two-dimensional FEA to determine the variation in response spectrums between both ducts. The conclusions of this study stated that the FEA provided a good correlation with their impact-echo results. In addition, the authors stated that the frequency of the dominant cross-sectional mode of vibration was the primary source for determining whether a duct embedded in a concrete beam was grouted or open (Hill, McHugh, & Turner, 2000).

2.3 Eigenvalue Analysis

Eigenvalue analysis is a method that utilizes the dynamic equation of motion to determine the natural frequencies experienced in a structure. In eigenvalue analysis, an equation of motion is considered and manipulated to combine both the modal mass and

modal stiffness of a structure into one equation. With this combined equation one can find the applicable natural frequencies and mode shapes. In eigenvalue analysis, structures can be considered single-degree-of-freedom (SDOF) systems or multiple-degree-of-freedom (MDOF) systems, based on their geometric complexity and boundary conditions as discussed in the next two sections.

2.3.1 Single Degree-of-Freedom Systems

When looking at a single degree-of-freedom system, the assumption made requires that there be one mass, which is lumped into one location. This lumped mass constitutes the only node for the structure. This assumption is made based on the primary direction of displacement. The basic equation of motion can be seen in Equation 9. Examples of SDOF systems include simplified water towers, flag poles, and radars to name a few, where the mass of the system is consolidated into one single location at the top of the structure. This equation can be simplified for the understanding of eigenvalue analysis by assuming no damping (c=0) (Chopra, 2007). Damping is the ability of a structure or specimen to dissipate dynamic energy. Equation 9 represents the simplified version of Equation 9 where there is no damping.

$$m\ddot{u} + c\dot{u} + ku = 0 \qquad \text{Equation 8}$$

$$m\ddot{u} + ku = 0 \qquad \text{Equation 9}$$

where,

m = mass
k = stiffness
c = damping
$\ddot{u}$ = acceleration
$\dot{u}$ = velocity
u = displacement

The free vibration of this system with respect to its displacement can be described by its mode shapes and a harmonic motion function as seen in Equation 10 and Equation 11 (Chopra, 2007).

$$u(t) = q_n(t)\Phi_n \qquad \text{Equation 10}$$

where,

$u(t)$ = displacement with respect to time
$q_n(t)$ = simple harmonic function
Φ_n = mode shape
n = nth mode

The simple harmonic function is defined as:

$$q_n(t) = A_n \cos \omega_n t + B_n \sin \omega_n t \qquad \text{Equation 11}$$

where,

$q_n(t)$ = simple harmonic function
ω_n = natural frequency
t = time

In Equation 11, A_n and B_n are constants and are dependent upon the initial conditions.

Equation 10 and Equation 11 can be combined, resulting in Equation 12.

$$u(t) = (A_n \cos \omega_n t + B_n \sin \omega_n t q_n(t))\Phi_n \qquad \text{Equation 12}$$

where,

$u(t)$ = displacement with respect to time
$q_n(t)$ = simple harmonic function

ω_n = natural frequency
t = time
Φ_n = mode shape

Substituting Equation 12 into Equation 11 and by taking its second derivative and substituting the result for ü, Equation 13 is obtained.

$$(-\omega_n^2 m\Phi_n + k\Phi_n)q_n(t) = 0 \qquad \text{Equation 13}$$

where,

$q_n(t)$ = nth simple harmonic function
ω_n = nth natural frequency
Φ_n = nth mode shape
m = mass
k = stiffness

A simple solution for Equation 13 would be to assume $q_n(t)$ to be 0. Assuming 0 for $q_n(t)$ would assume the harmonic function was 0 rendering no vibration; therefore the assumption of 0 for the harmonic function can be discarded. With this understanding, Equation 13 can be simplified. Equation 14 factors out Φ_n understanding that the mode shape also cannot be 0 (a value of 0 for the mode shape would assume no deflection).

$$k - \omega_n^2 m = 0 \qquad \text{Equation 14}$$

where,

ω_n = natural frequency
M = mass
k = stiffness

By solving for Equation 14, the characteristic equation for eigenvalue analysis has been obtained. In order to solve for the natural frequencies, the determinant of Equation 14 is taken and the positive roots of ω_n^2 depict the natural frequencies. In the case of the water tower (SDOF), the support system would be assumed to have no mass and the water

container would be assumed to have a lumped mass at the top of the tower. In this simplified case, there would only be one natural frequency due to the single degree-of-freedom.

2.3.2 Multiple Degree-of-Freedom Systems

The previous illustration of eigenvalue analysis considers a single degree-of-freedom (SDOF) system with no damping. When considering a multiple degree-of-freedom (MDOF) system with damping, the analysis follows the same steps but becomes much more complicated. MDOF systems vary from SDOF systems in that they have more than one node. MDOF systems can range from steel framed structures to complex church vaults. The fundamental equation of motion is similar to Equation 9 except the mass and stiffness of the system should be in matrix form to consider all the nodes. Equation 15 and Equation 16 apply to eigenvalue analysis used in impact-echo testing, where there is damping and an applied force, $\{p(t)\}$. Equation 15 depicts the general equation of motion. Equation 16 is the characteristic equation for eigenvalue analysis for MDOF systems (Chopra, 2007).

$$[m]\{\ddot{u}\} + [c]\{\dot{u}\} + [k]\{u\} = \{p(t)\} \qquad \text{Equation 15}$$

$$[k] - \omega_n^2[m] = 0 \qquad \text{Equation 16}$$

where,

[m] = mass matrix
[k] = stiffness matrix
[c] = damping matrix
{ü} = acceleration matrix
$\{\dot{u}\}$ = velocity matrix
$\{u\}$ = displacement matrix

Eigenvalue analysis allows for the solution of all possible mode shapes and natural frequencies. The results from an eigenvalue analysis are used in modal analysis to determine a system's response to a particular excitation which will be discussed in following chapter.

An example of a multiple degree-of-freedom system could be a 2D freebody diagram of a structural frame in a building. In this example, the mass of each floor is lumped at the center of the floor and the columns are assumed to have no mass. As you can see in Figure 13, a MDOF system has more than 1 natural frequency and has multiple stiffness values (k) and masses (m). This particular example would have 2x2 matrices in Equation 15 and 16.

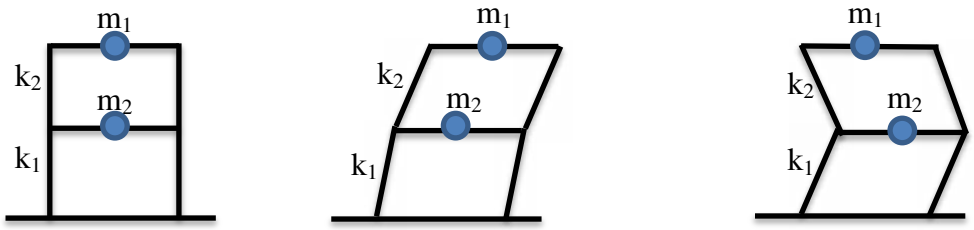

Figure 13: (a) Simplified MDOF system with 2 degrees of freedom, (b) 1st mode shape, (c) 2nd mode shape

2.4 Modal Analysis

Modal analysis as defined by Chopra (2007) is an analysis method that allows for the determination of the dynamic response of a system subjected to an external force. In impact-echo testing this external force is often characterized by a sinusoidal force equivalent to a half-sine cycle. The half-sine cycle best represents an impact from a sphere or an impact hammer (Hill, McHugh, & Turner, 2000). Modal analysis includes eigenvalue analysis initially and uses that data to then compute the nodal displacements

($u_n(t)$). Once nodal displacements are computed, the total response can then be obtained (Chopra, 2007).

2.4.1 Modal Participation Factors

Modal participation factors provide an understanding of how a system will behave and which modes or natural frequencies contribute the most to a prescribed response (Chopra, 2007). The modal participation factor for a system is calculated using Equation 17.

$$\Gamma_n = \frac{\Phi_n^T\{s\}}{M_n} \qquad \text{Equation 17}$$

where,

Γ_n= nth mode participation factor
Φ_n^T= transpose of the nth mode shape matrix
M_n= normalized mass matrix
$\{s\}$=spatial distribution matrix

As seen in Equation 17, the participation factor for a specific mode is dependent upon the modal mass matrix, the mode shape for that particular natural frequency, and the spatial distribution matrix. The mode shape and modal mass matrix are completely independent of the force induced on the system. In order to account for the various forces in a dynamic analysis, the spatial distribution matrix is required. The spatial distribution matrix illustrates how a specific force affects the entire system. In short, the spatial distribution matrix displays the force distribution in the system according to a specific natural frequency and force input.

Chapter 3: Methodology and Testing

This chapter describes the research methodology used in this study. Impact-echo testing was completed both in the field in Turkey and in the University of Nebraska's structural laboratory. The eigenvalue analysis provided by Sansalone and Streett serves as the basis for the theoretical analysis. Lastly, the finite element model was completed using a commercial software (ANSYS) to perform a parametric study on various cross-sections. Figure 14 provides a schematic representation of the process followed for the study.

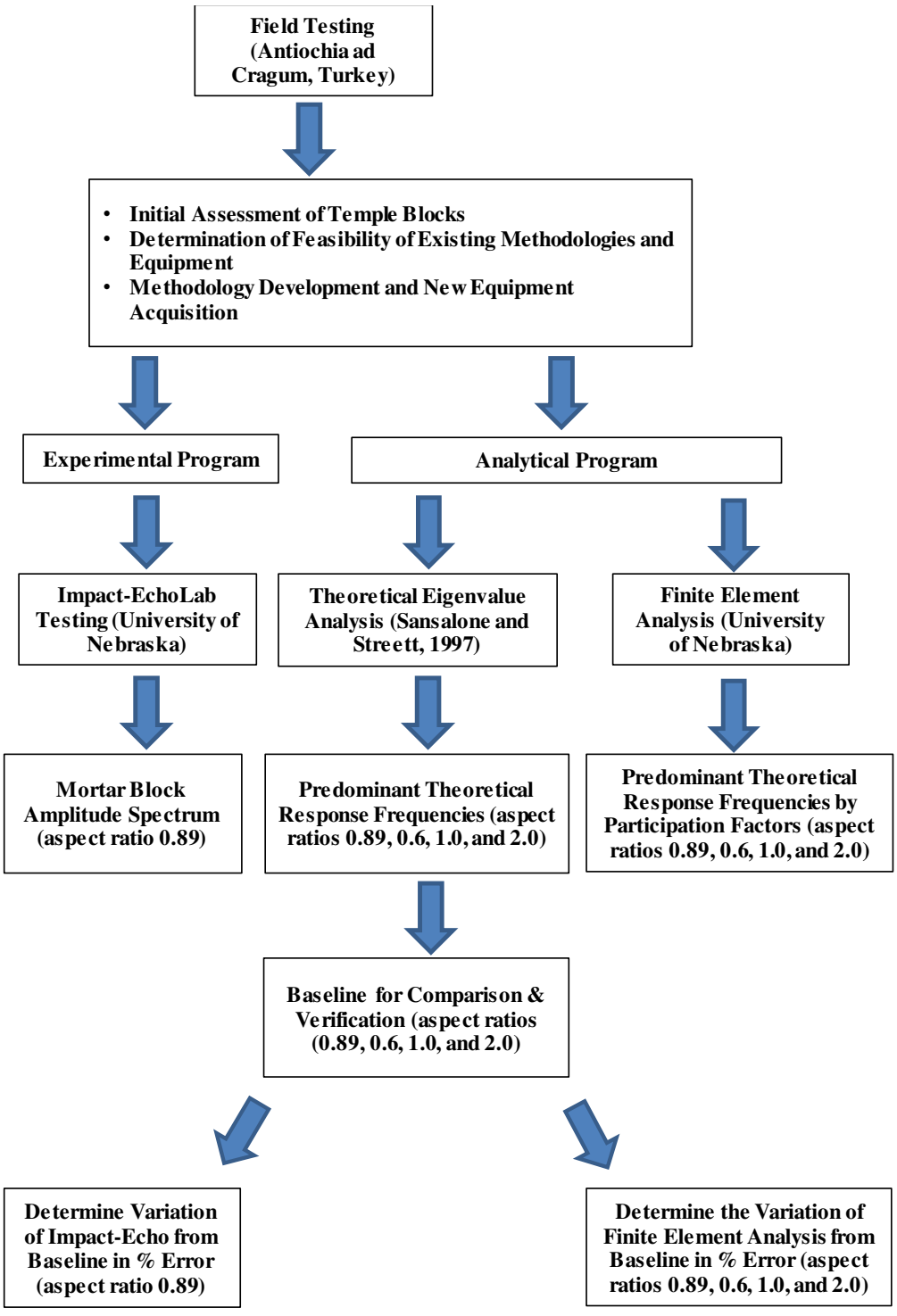

Figure 14: Schematic of complete study

3.1 Impact-Echo Testing

Impact-echo testing was conducted both in the laboratory at the University of Nebraska and in the field at Antiochia ad Cragum. The testing sessions used a variety of equipment and testing methods. Field testing at Antiochia ad Cragum provided the parameters and the basis of the study. Lab testing at the University of Nebraska allowed for the development of the proposed block assessment tool in a controlled setting.

3.1.1 Field Testing

Field testing at Antiochia ad Cragum was conducted during July and August of 2011. Multiple tests were conducted during the research session and various test setups were utilized to assess the applicability of the existing equipment. The equipment available at the time of field work consisted of an array of accelerometers, an impact hammer, and SIGLAB.

3.1.1.1 Impact Hammer

The impact hammer used was PCB Piezotronics model 086D20. This hammer includes 3 different tips with varying head densities. Model 086D20 has a maximum resonant frequency of 12 kHz and has a variable frequency excitation range between 400 Hz and 1200 Hz with the hardest tip provided (PCB Piezotronics, 2007). Figure 15 shows the predicted frequency excitation for a model 086D20 impact hammer for specific impact tips. The model 086D20 impact hammer is equipped with a load cell. The hardest tip was used in the field testing to obtain the highest possible excitation frequency.

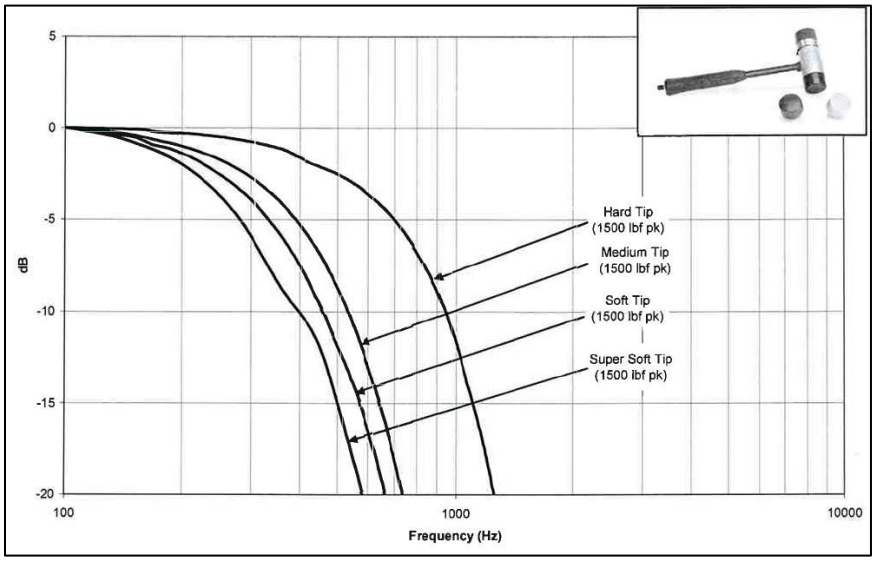

Figure 15: Predicted frequency excitation of a model 086D20 impact hammer (PCB Piezotronics, 2007)

3.1.1.2 Accelerometers

Four PCB Piezotronics model 393A03 accelerometers were available during field work in Turkey. These accelerometers have a resonant frequency of 10 kHz or greater. The measurement range for these accelerometers ranges from 0.5 Hz up to 6000 Hz. Sensitivities for a model 393A03 accelerometer range from ±5% of 1000mV/g.

The accelerometers were affixed to the stones with typical reusable adhesive putty found in office supply retailers. According to the accelerometer operating manual, this mounting setup will produce a 40 dB increase in sensitivity at 80 kHz (PCB Piezotronics, 2002). This sensitivity dissipates as the frequency range decreases. Between 20 kHz and 1 Hz, there is no noticeable change in the sensitivity. Figure 16 illustrates the predicted

change in sensitivity for each mounting method and is applicable to all PCB accelerometers.

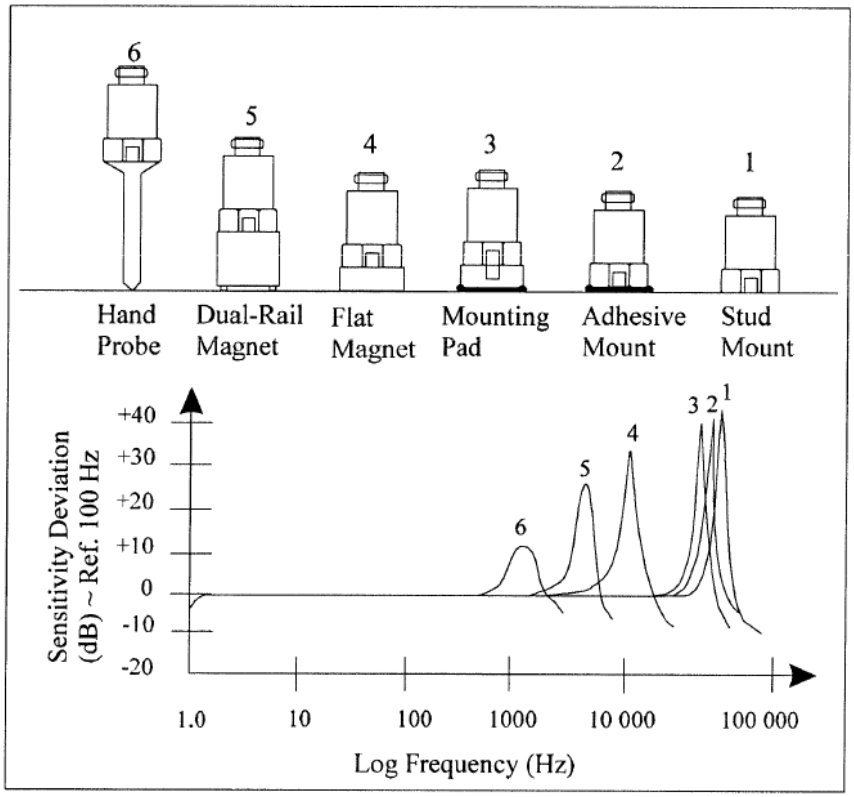

Figure 16: PCB accelerometer mounting sensitivity deviation (PCB Piezotronics, 393A03 Installation and Operating Manual, 2002)

3.1.1.3 SIGLAB and MATLAB

The dynamic signal analyzer, SIGLAB, used for the duration of this study is a product of Spectral Dynamics. SIGLAB, in conjunction with MATLAB constitute the analysis software and hardware. MATLAB, a programming environment, is utilized by SIGLAB for the data analysis and processing. The specific test setup for each lab test is available in Appendix A: Supplemental Field Testing Reference Material.

During the field and lab testing, SIGLAB's Dynamic Signal Analyzer (VNA) was used. SIGLAB's VNA allows for a variety of channel measurements including time histories, coherence, impulse responses, and FFTs. As previously discussed in Chapter 2.1.3 and Chapter 2.1.4, the frequency resolution, the number of samples, and the sampling interval are often related. This is indicative of SIGLAB as used in field testing, where the sampling frequency is always decided upon by the user's bandwidth selection. The sampling frequency is always 2.56 times the selected bandwidth as seen in Equation 18 (Spectral Dynamics, 2001). This allows for an acceptable sampling frequency as described by Sansalone and Streett. Equation 18 is unique to SIGLAB's sampling frequency.

$$FS = 2.56BW \qquad \text{Equation 18}$$

where,

FS=sampling frequency
BW=bandwidth selection

The number of samples is calculated by dividing the record length by 2.56 plus one as seen in Equation 19. Equation 19 is also unique to the particular signal analyzer used in this study, SIGLAB.

$$N = \frac{RL}{2.56} + 1 \qquad \text{Equation 19}$$

where,

N=number of samples
RL=record length

Testing in the field utilized the first channel (where the impact hammer with a load cell is connected) in SIGLAB as the trigger while the subsequent channels were used for accelerometers. All channels were calibrated according to the device data provided by PCB Piezotronics. Accelerometers were all adjusted according to their calibration data and their input was set to BIAS, while the impact hammer was also set to BIAS. The BIAS selection in SIGLAB simply provides power to the accelerometers and the load cell in the impact-hammer.

3.1.1.4 Test Specimens

The specimens tested in the field, totaling 30, consisted of a variety of metamorphic stone blocks. Many of the blocks showed damage and weathering of varying degrees. Damage in the stone blocks ranged from minimal hairline cracking to complete deterioration and separation. The stones in the field were arranged in block fields and typically were simply supported on timbers at each end. The stones in the field had varying orientations regarding the bedding of the layers in the stones. The coloration and composition varied between stones as did the degree and type of weathering. Surface conditions of each block ranged from smooth to very rough. Blocks selected for testing represented a uniform coloration and a uniform visual structural condition in order to minimize variation in wave speeds. Figure 17 shows a sample test setup in the field.

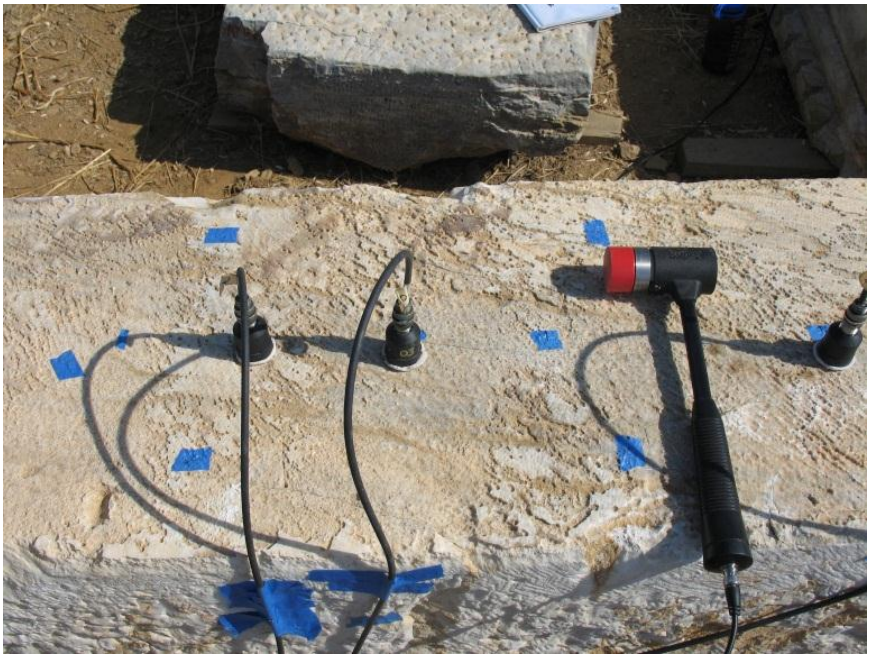

Figure 17: Impact-echo field testing impact hammer and accelerometers

3.1.1.5 Traditional Impact-Echo Testing

Traditional impact-echo testing as described in this study includes the use of an impact hammer and an accelerometer located in the same cross-sectional plane of a specimen. Traditional impact-echo testing, as it pertains to this study is concerned primarily with the cross-sectional response rather than the flexural response, as previously discussed in Chapter 2.1.5. Further reference to traditional impact-echo testing refers to the use of one or more accelerometers in conjunction with an impact hammer to testing the cross-sectional vibration of a specimen near the center of the specimen. In addition, traditional impact-echo testing as described in this study also refers to the use of averaging and normalizing of the response, where the average is based upon 5 separate excitations from the impact hammer.

Traditional impact-echo testing was conducted in the field and the results were analyzed for a variety of stones. Modal testing was also attempted in the field. Varying locations were selected for the sensor array and multiple impact points were tested. Each test conducted in the field, including the straight-line velocity tests and used 5-test averaging. This setup requires 5 individual tests to be conducted with the same setup. After all 5 tests are completed, SIGLAB outputs the normalized average response for the setup. All aspects of the testing process were documented including the weather, the testing setup, which stone was being tested, and which accelerometers were being used. The results and discussion for these tests are presented in section 4.1.1.

3.1.1.6 Straight-Line Velocity Testing

Straight-line velocity testing was also conducted according to ASTM C1383-04. The straight-line velocity test was initially conducted on every stone to determine the properties and wave speeds of each specimen, but thorough straight-line velocity tests were conducted on only a small sample of stones. Discussion of these tests is included in section 4.1.1.

3.1.2 Lab Testing

Laboratory testing at the University of Nebraska was conducted from October of 2011 through February of 2012. A rectangular block was cast to best represent the geometric properties of the stones tested in Turkey, while providing an easily measurable set of properties (ρ, ν, and E). The equipment used during the testing phase consisted of one accelerometer, an impact hammer, and SIGLAB. Figure 18 shows the laboratory testing setup.

Figure 18: Impact-echo laboratory testing impact hammer and accelerometer

3.1.2.1 Mortar Block Casting

In order to provide a control specimen for developing a reliable testing setup, a block with discernible properties and dimensions was needed. The material needed to be homogenous in nature, and similar to the density of the stones in Turkey. According to previous tests, the stones in the field were determined to have a density of 2600 kg/m^3. It was then determined that either a concrete mix with limited coarse aggregate or a mortar mix would provide a density close to the field stones. Type-N mortar was chosen as the material due to its availability and because of its relatively homogenous character when cured (i.e. no coarse aggregate to alter wave propagation). Type PL-01 mortar, a Portland lime and sand mortar, manufactured by SPEC MIX was used. This mix meets ASTM C 270 for type-N mortar (SPECMIX, 2011).

Formwork was constructed and the block was poured over a period of 3 hours. Each 80 lb. bag was mixed with 1.75 gallons of water. Mixing was conducted according to the manufacturer's specifications. This mixing procedure specified adding 75% of the water to the mixer in addition to the 80 lbs. of mortar mix and mixing for 4 minutes. Mixing concluded with adding the remaining water and mixing for one additional minute. A mechanical mixer was used as specified by the manufacturer (SPECMIX, 2011). Two 4 in diameter cylinders were also cast to provide material properties. The cylinders were cast in the third lift and the second to last lift. The cast block measures approximately 0.49 m x 0.56 m x 1.5 m, weighing approximately 9800 N (1000 kg) and will be hereafter referred to as *mortar block*. The mortar block resulted in an aspect ratio of 0.89 and is shown in Figure 19.

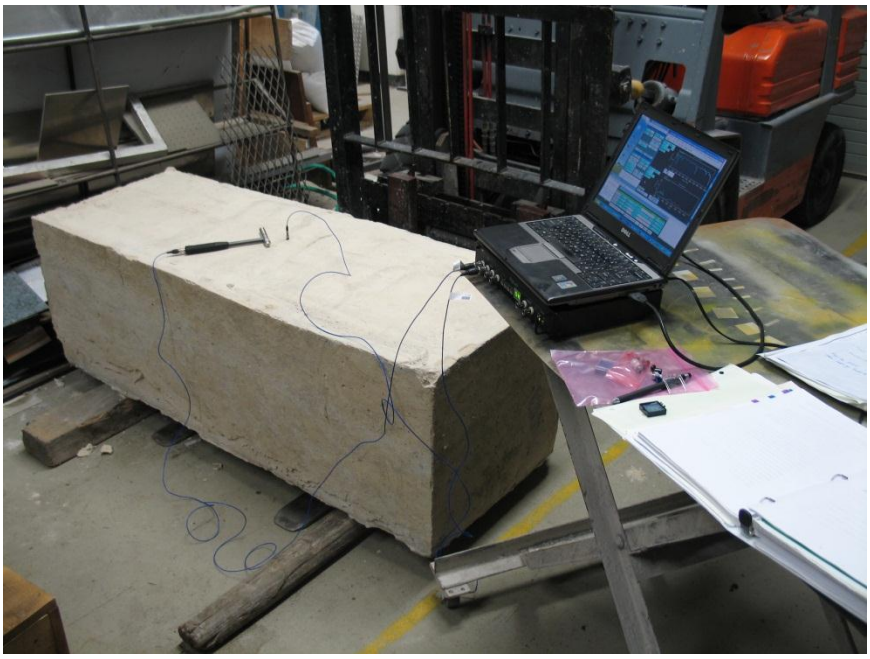

Figure 19: Mortar block and lab testing setup

3.1.2.2 Impact Hammer

Testing in the laboratory utilized a PCB Piezotronics, Inc. model 086C01 impact hammer. This hammer has multiple impact heads and coverings to provide a variety of excitation frequencies. The model 086C01 impact hammer has a range of 400 Hz up to 15 kHz. Figure 20 shows the predicted frequency excitation for a model 086C01 impact hammer for specific impact tips. In order to obtain a higher frequency, tips were used without covers to provide shorter impact durations. The resonant frequency for a 086C01 impact hammer is greater than 15 kHz. The model 086C01 impact hammer is equipped with a load cell and an extender mass to increase the amplitude of a response.

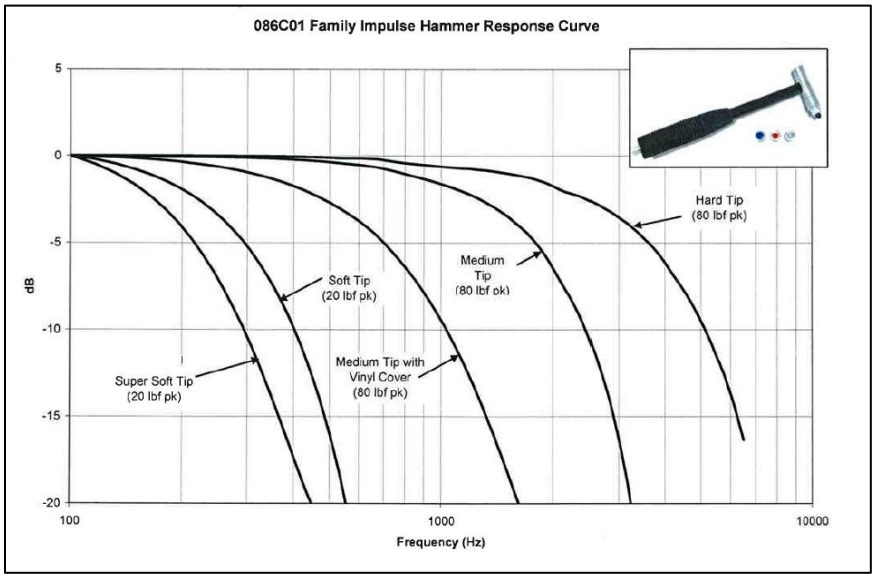

Figure 20: Predicted frequency excitation of a model 086C01 impact hammer (PCB Piezotronics, 086C01 Installation and Operation Manual, 2007)

3.1.2.3 Accelerometers

The two accelerometers used in laboratory testing were a model 352C68 accelerometer and a model 353B33 accelerometer. Both accelerometers are products of PCB Piezotronics, Inc. Model 352C68 accelerometers have a resonant frequency of 35 kHz and their measurement range is 0.5 Hz to 20,000 Hz. Sensitivities for a model 352C68 accelerometer range from ±10% of 100mV/g (PCB Piezotronics, 2002). Model 353B33 accelerometers have a resonant frequency of 22 kHz or greater. The measurement range for a 353B33 accelerometer ranges from 1 Hz up to 12,000 Hz and they have a sensitivity of ±5% of 100mV/g (PCB Piezotronics, 2002). Table 2 provides a summary of the accelerometer used in lab testing.

Table 2: Summary of accelerometers used in lab testing

Accelerometer	Manufacturer	Resonant Frequency	Measurement Range	Sensitivity
352C68	PCB Piezotronics	35 kHz	0.5 Hz - 20,000 Hz	±10% of 100 mV/G
353B33	PCB Piezotronics	22 kHz	1 Hz - 12,000 Hz	±5% of 100 mV/G

Both PCB Piezotronics accelerometers come with a standard stud mount, which would require drilling and semi-permanent attachment to a specimen. In order to best represent the conditions in the field, the accelerometers were mounted using an additional flush mounting bracket, which is attached to the mounting stud on the accelerometer. This mounting bracket, shown in Figure 21, allows for the wax adhesive, provided by PCB Piezotronics, to be applied to the bottom of the accelerometer in order to affix it to a specimen without altering the testing surface.

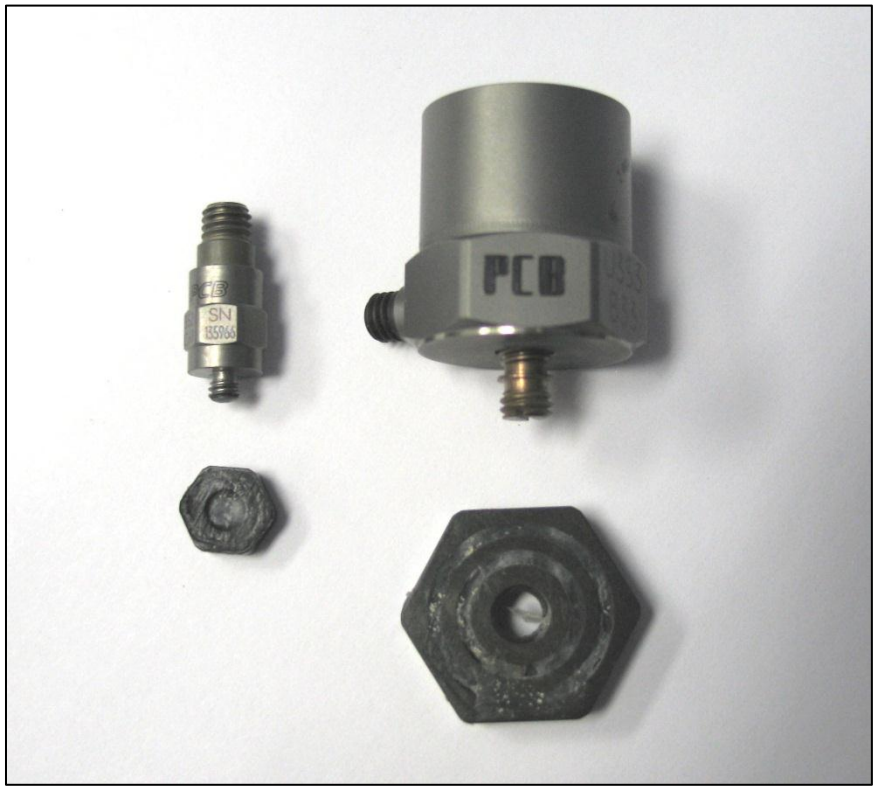

Figure 21: PCB Piezotronics Inc. adhesive mounts for accelerometer models 353B33 (right) and 352C68 (left)

Similarly to the 393A03 accelerometer, the sensitivity of the 352C68 or the 353B33 accelerometers also is unaffected by an adhesive mounting setup (PCB Piezotronics, 2002).

3.1.2.4 SIGLAB and MATLAB

SIGLAB and MATLAB were used for the analysis software. As in the field testing, SIGLAB's Dynamic Signal Analyzer (VNA) was used. The specific test setup for each lab test is available in Appendix B: Supplemental Lab Testing Reference Material. Testing in the lab utilized the first channel (with the impact hammer and load

cell) in SIGLAB as the trigger while the second channel was used for the accelerometer. In straight-line velocity tests, accelerometers were connected to channels two and three, while channel one contained the impact hammer. As in the field testing, all channels were calibrated according to the device data provided by PCB Piezotronics. BIAS selection was used for all channels in the lab testing.

3.1.2.5 Material Property Identification

The cylinders cast during the mixing phase were used to determine the density of the mortar and the modulus of elasticity. Poisson's ratio was not included in the property identification due to its minimal impact on the response of a specimen (Popovics, 1997).

These cylinders were allowed to cure in the same environment as the mortar block. In order to determine the density of the mortar block, the two cylinders were weighed and their lengths and diameters measured. Each cylinder's diameter was measured at each end and the middle. These diameters were averaged and the cross-sectional area was determined. The volume was calculated by multiplying the cross-sectional area by the length. Finally, the density was determined by dividing the weight by the volume. Both of these values were averaged to determine an average density.

In order to determine the modulus of elasticity, each cylinder was fitted with a strain gauge and tested in compression. The strain gauges were applied vertically and adhered with the cyanoacrylate adhesive prescribed by Tokyo Sokki Kenkyujo Co., Ltd., the strain gauge manufacturer. The strain gauges were type PL-60-11 as shown in Figure 22. The cylinders were placed on top of a steel plate to evenly distribute the load on the

load cell beneath. The compression machine used was manufactured by Tinius Olsen. The strain gauge and load cell data were collected via universal testing software provided by Tinius Olsen. The cylinders were tested to failure.

Figure 22: PL-60-11 strain gauge attached to a cylinder

Figure 22 shows the cylinder after testing to failure. The compression and strain data were exported for determination of the modulus of elasticity. Output from the test was converted from a force (lb.) to a stress (psi). The strain was recorded in micro strain (με). The modulus of elasticity was obtained using ASTM C469/C469M.

3.1.2.6 Traditional Impact-Echo Testing

Traditional impact-echo testing was conducted on the mortar block with a variety of impact hammer tips, however only one tip offered substantial results. As a result, the impact-echo testing conducted in the lab displays the results from an impact generated by the metal tip provided for the model 086C01 impact hammer.

3.1.2.7 Straight-Line Velocity Testing

Straight-line velocity tests were also conducted on the mortar block in order to determine C_p, the P-wave speed. Straight-line velocity tests were conducted in accordance with ASTM C1383-04. In order to best represent a "spacer device", as prescribed by ASTM C1383-04, the model 352C68 and the model 353B33 accelerometers were placed 300mm apart and then measured to the center of each accelerometer. Each straight-line velocity test was conducted individually without averaging. After testing, the time-series data was imported into Microsoft Excel and P-wave speed was calculated. P-wave speed was calculated using ASTM C1383-04. Wave speed was assumed to be uniform for the entire specimen per the assumption of homogeneity.

3.2 Theoretical Eigenvalues

Theoretical modes of vibration were calculated based upon the equations presented in Table 1. These equations were computed for varying D/B ratios using the same values for ν, E, and ρ as the FEM model to allow for comparison of results. The first modes of vibration were calculated for every D/B ratio using their respective shape factors for the fundamental modes. Each of the 5 subsequent modes was calculated based on Table 1. The calculated modes of vibration can be seen in Table 3 with their respective D/B ratios and their shape factors.

Table 3: Frequencies for the theoretical fundamental modes of vibration for aspect ratios 0.6, 1.0, and 2.0

Aspect Ratio D/B	Beta	Fundamental Mode (Hz)	Mode 2 (Hz)	Mode 3 (Hz)	Mode 4 (Hz)	Mode 5 (Hz)	Mode 6 (Hz)
0.60	0.84	1711	1831	2447	2533	3183	3269
1.00	0.87	2127	2999	4041	5211	6019	4977
2.00	0.96	1173	2124	2417	2617	3004	3426

3.3 Finite Element Modeling

Modal analysis through ANSYS, a finite element modeling software, was conducted to correlate the eigenvalue analysis, previously completed by Sansalone and Streett, with FEA results. FEA was also used to correlate the impact-echo testing conducted on the cast mortar block with FEA results. An array of block sizes was selected for the verification of the eigenvalue analysis including aspect ratios of 0.6, 1.0, and 2.0. The aspect ratios of 0.6, 1.0, and 2.0 make up FEA Set 1. In addition, FEA Set 2 was created with the dimensions of the laboratory block cast from mortar (aspect of 0.89). Figure 23 shows a schematic representation of the FEA process.

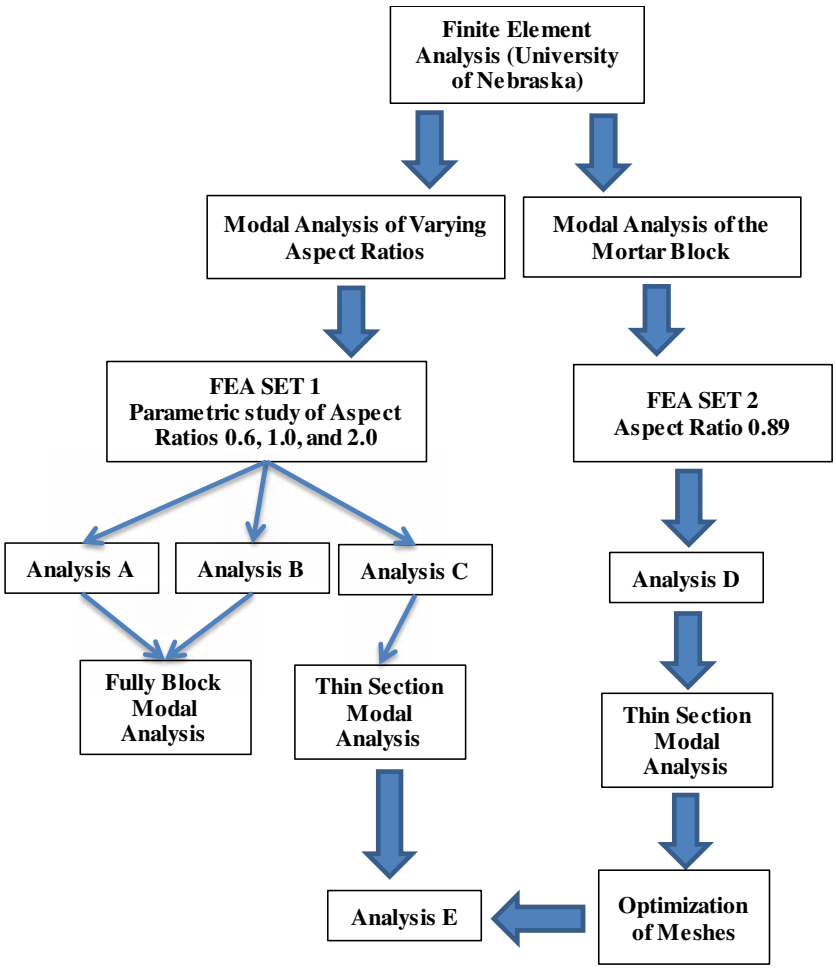

Figure 23: Schematic of FEA process

3.3.1 Modal Analysis of Varying Aspect Ratios (FEA Set 1)

The dimensions of the finite element models are shown in Table 4. The length of each specimen was determined to satisfy the length requirements for bar-like specimens as previously discussed Chapter 2.1.5 (i.e. the length of specimen must be equal to or greater than three times the largest cross-sectional dimension).

Table 4: FEA model dimension summary

Model Number	Dimensions (m)	Aspect Ratio (D/B)
1	0.6 x 1.0 x 3.0	0.60
2	0.5 x 0.5 x 1.5	1.0
3	1.0 x 0.5 x 3.0	2.0
4	0.5 x 0.56 x 1.5	0.89

Each of these aspect ratios was used in ANSYS to create 4 different finite element models. Each finite element model was discretized with Solid 186 elements as recommended in the ANSYS Structural Analysis Guide (ANSYS, Stuctural Analysis Guide, 2009). Solid 186 elements provide increased accuracy due to the large number of nodes per element. Figure 24 depicts the Solid 186 element as used in ANSYS Mechanical APDL (ANSYS, ANSYS Mechanical APDL, 2011).

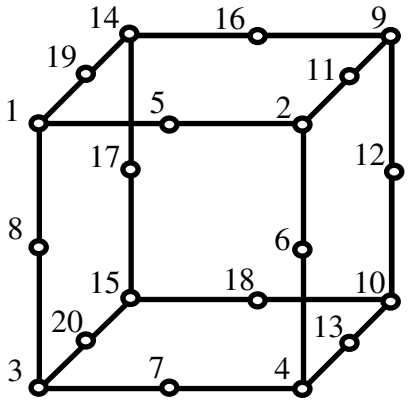

Figure 24: Solid 186 element and nodes

Solid 186 elements, which perform well naturally in a rectangular form, provide a reliable mesh due to their correlation with the square rectangular shape of the finite

element models (ANSYS, ANSYS Workbench, 2011). Figure 25 illustrates the finite element models used in Analysis A and B within FEA Set 1.

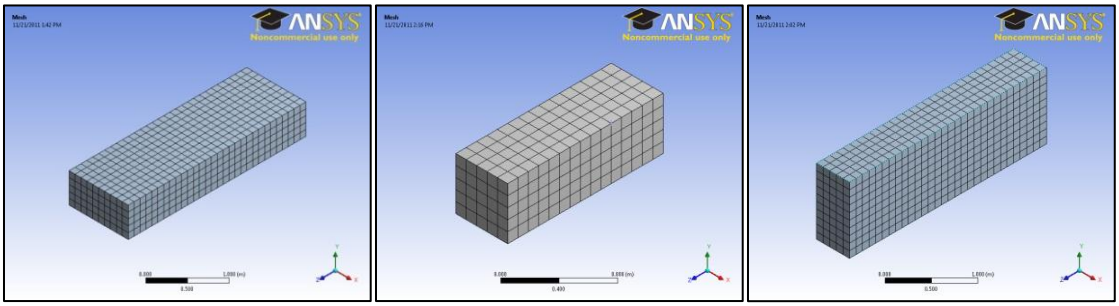

(a) (b) (c)

Figure 25: Meshed Solids for aspect ratios (a) 0.6, (b) 1.0, (c) 2,0

All models were constructed using values for ν (Poisson's ratio), E (modulus of elasticity), and ρ (density) gathered from literature or laboratory testing of the mortar cylinders. Table 5 lists the values used for these properties and their source.

Table 5: Mortar material properties

Property	Value	Source
Density (ρ)	2500 kg/m^3	Lab Testing
Modulus of Elasticity (E)	1.42x10^{10} Pa	Lab Testing
Poisson's Ratio (ν)	0.15	Essom Equipment for Engineering, 2007

Various support conditions were considered including simply supported at thirds, to represent the current configuration of wooden supports. It was decided that simple supports would present the most valuable information for a variety of sites and specimens due to its practical application. Once meshed, each model was subjected to a range of modal analyses. Four sets of analyses were conducted on each model. Table 6 describes each analysis and their associated boundary conditions.

Table 6: Description of each individual analysis and associated boundary conditions

	Description	Boundary Conditions
Analysis A	Whole block models with full dimensions (aspect ratios 0.6, 1.0, and 2.0)	All nodes free in all directions
Analysis B	Whole block models with full dimensions(aspect ratios 0.6, 1.0, and 2.0)	Z-axis displacement restricted on all nodes
Analysis C	Thin cross-section of block models (aspect ratios 0.6, 1.0, and 2.0)	Z-axis displacement restricted on all nodes
Analysis D	Thin cross-section of block with mortar block dimensions (aspect ratio 0.89)	Z-axis displacement restricted on all nodes
Analysis E	Thin cross-section of block models (aspect ratios 0.6, 1.0, and 2.0)	Z-axis displacement restricted on all nodes

In these analyses, up to 300 modes of vibration were recorded with a specified range of 0 Hz to 10,000 Hz. The use of 300 possible modes of vibration was used for every finite element analysis. Participation factors were recorded for these analyses at a node located at the centroid of the top face. Participation factors in the y-direction were the only factors considered because the uniaxial accelerometers used in impact-echo testing only record y-axis displacement.

In order to better represent the results from an impact echo test, where the accelerometer and the transducer are located in the same cross-sectional plane, Analysis B was conducted where the longitudinal direction of motion (z-axis) was restrained for each node. The restraint in the z-axis was conducted with expectation of limiting the flexural behaviors, which in cross-sectional vibration analysis, are less indicative of internal structural conditions (Sansalone & Streett, 1997). In Analysis B, participation

factors were gathered for each frequency at a node located near the centroid of the top surface similar to Analysis A. Participation factors corresponding to the y-direction were the only factors considered. As previously stated, this is due to the uniaxial nature of the provided accelerometers.

After further investigation, it was determined that Sansalone and Streett used thin sections of specimens to complete their eigenvalue analysis. As a result, three additional models were created and analyzed to further understand their dynamic behaviors. These models retained the original aspect ratios, but were modeled as 0.2 m thick in order to correlate with the eigenvalue analysis provided by Sansalone and Streett. This set of analyses comprises Analysis C.

Figure 26 depicts the sections used for Analysis C. Just as in the second set of tests, only the y-axis participation factors were recorded at a node located near the centroid of the top face.

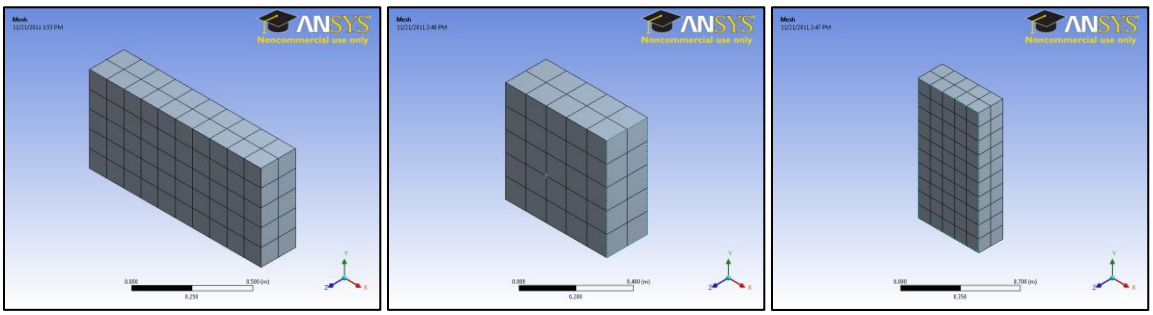

(a) (b) (c)

Figure 26: Mesh of finite element model with an aspect ratio of (a) 0.6, (b) 1.0, (c) 2,0

Analysis E was conducted based upon the results from Analysis D associated with Chapter 3.3.2, where the discretization of meshes was optimized using an aspect ratio of

0.89. Using aspect ratios of 0.6, 1.0, and 2.0, thin sections were created using optimized mesh characteristics. The new finite element models were 0.1 m thick with meshes composed of elements with edge lengths of 0.05 m. Figure 27 shows the meshes associated with Analysis E.

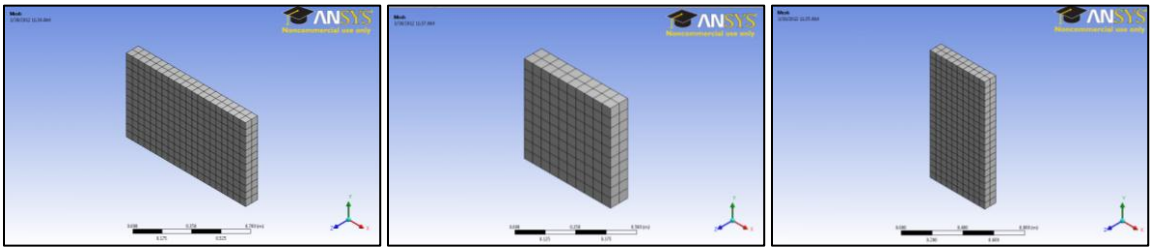

(a) (b) (c)

Figure 27: Optimized mesh for the FEM with an aspect ratio of (a) 0.6, (b) 1.0, (c) 2.0

These models were subjected to modal analysis and participation factors were extracted for the y-axis direction and recorded corresponding to the mode of vibration.

3.3.2 Modal Analysis of the Mortar Block (FEA Set 2)

The laboratory mortar block resulted in an aspect ratio that did not match the previous finite element models (0.89); a new set of finite element analyses was created based on an aspect ratio of 0.89, which corresponds to the mortar block. These analyses are part of Analysis D. The same values for ν, ρ, and E, as seen in Table 5, were used for Analysis D. Three thin sections with dimensions of 0.50 m x 0.56 m were created with thicknesses of 0.1 m.

All models were discretized with Solid 186 elements. Table 7 lists the number of elements tall, wide, or thick of a particular mesh size. The minimum edge length is also provided in Table 7.

Table 7: Model 4 FEA mesh summary

Mesh	Minimum edge length (m)	Elements Tall	Elements Wide	Elements Thick
Coarse	0.0500	10	12	2
Medium	0.0250	23	20	4
Fine	0.0125	45	40	8

The three meshes (coarse, medium, and fine) are illustrated in Figure 28.

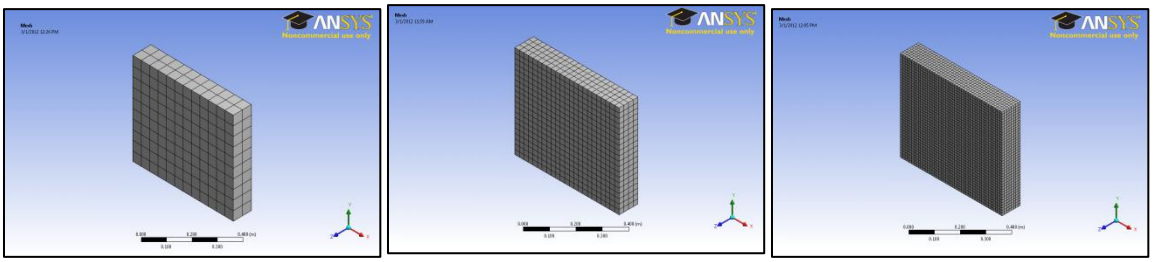

(a) (b) (c)

Figure 28: (a) Coarse, (b) medium, and (c) fine meshes of the finite element model with an aspect ratio of 0.89

The coarse, medium, and fine mesh finite element models were subjected to the same modal testing as Analysis A, B, and C. Y-axis participation factors were recorded from a node located near the centroid of the top face of each model as in Analysis A through C.

Chapter 4: Results and Discussion

Chapter 4 presents the results of this project along with a discussion of results. The results from impact-echo testing in the field and in the lab are covered first. Included in the "Impact-Echo Testing" section are the required tests to calibrate the equipment and determine material properties. Following the impact-echo results, the finite element analysis results are discussed. In addition, comparison of the results are included, as is the development of a real-time impact-echo analysis prog

4.1 Impact-Echo Testing

Impact-echo testing conducted on the blocks of the temple of Antiochia ad Cragum in Turkey provided an understanding of the applicability of the impact-echo methods to the large blocks and the conditions of metamorphic stones on an archeological dig site. Testing results from the field consist of multiple traditional impact-echo tests and attempts at straight line velocity tests. Lab testing at the University of Nebraska on a mock physical model includes material property identification, traditional impact-echo tests, and straight-line velocity tests. Lab testing was developed using the knowledge gained in the field and with the use of a controlled specimen, results could be verified via analytical methods.

4.1.1 Field Testing

The typical impulse of the impact hammer on the stones in the field is depicted in Figure 29.

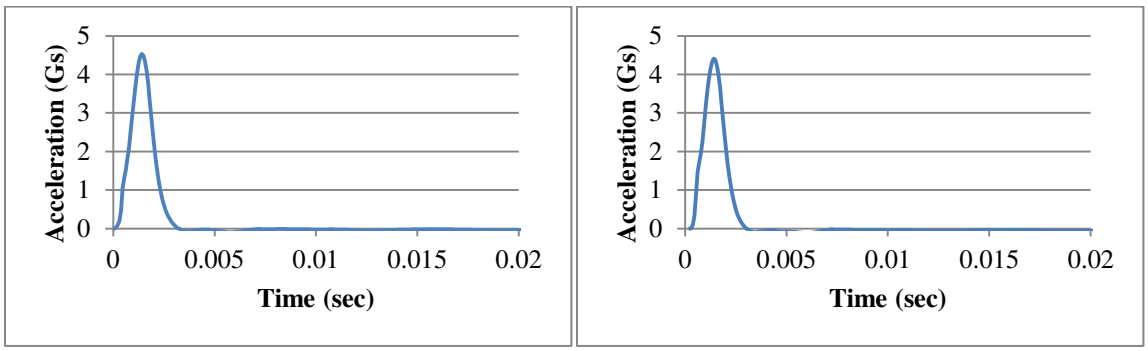

(a) (b)

Figure 29: Impact-hammer elastic impact of (a) field test 1 and (b) field test 2

Figure 30 and Figure 31 illustrate the excitation frequency range by showing the FFTs of the elastic impact data.

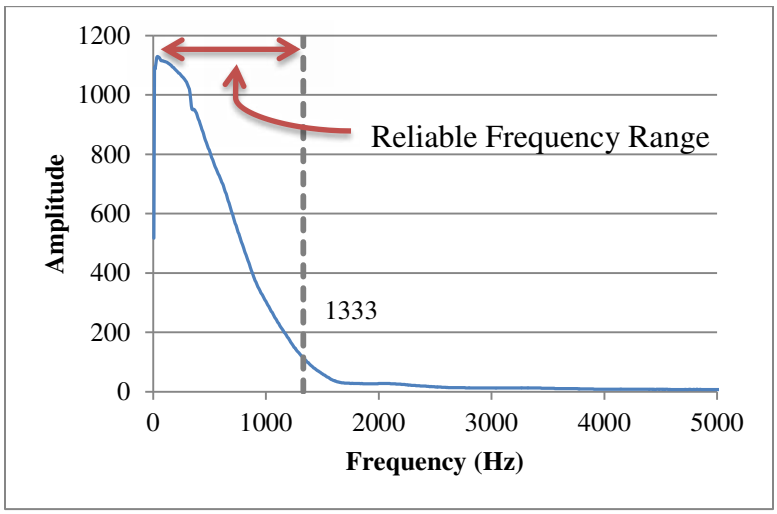

Figure 30: FFT of elastic impact on field test 1

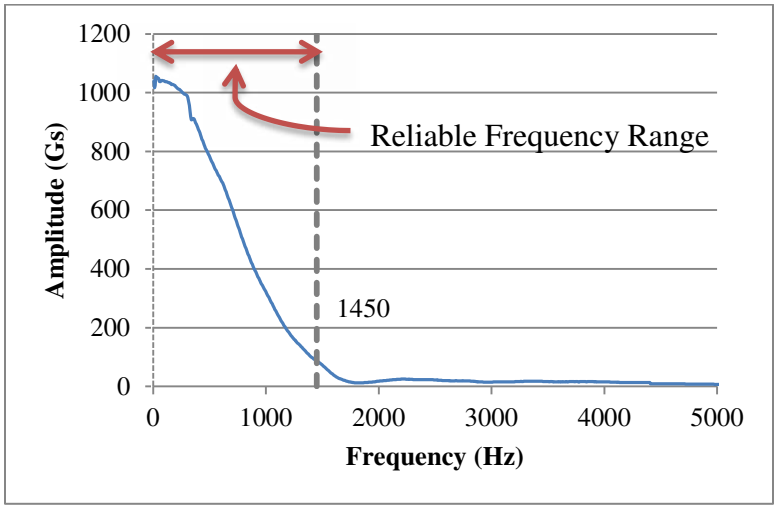

Figure 31: FFT of elastic impact on field test 2

As can be seen in Figure 30 and Figure 31, the impact hammer, a model 086D20, available at the time of field testing provided excitation frequencies (where the graph approaches 0) of 1600 Hz for test 1 and 1750 Hz for test 2. Consequently, this limited the reliable frequency range to 1333 Hz and 1450 Hz, based on Sansalone's and Streett's (1997) conclusion that useful frequencies are only obtained below a frequency of 1.25 divided by the contact time (see section 2.1.4). The maximum useful frequency range for test 1 and test 2 is shown by the dotted line on Figure 30 and Figure 31, respectively.

As can be seen in Figure 32 and Figure 33, the coherence of the field tests decreases dramatically as it passes 1500 Hz, illustrating the useful frequency range, reinforcing Sansalone's and Streett's conclusion. Since the expected vibration response for the cross-section of the metamorphic blocks in the field was between 2000 Hz and 6000 Hz (Table 3), none of the required response spectrum was observed.

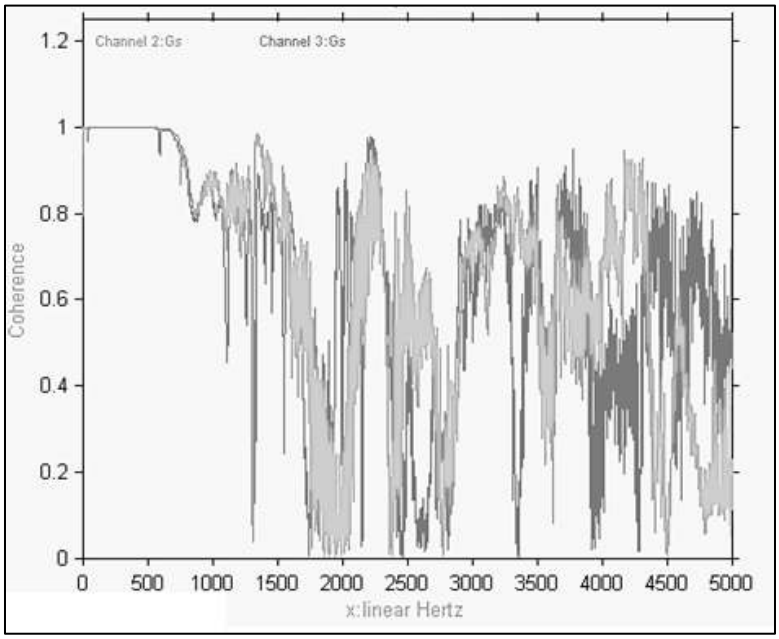

Figure 32: Coherence of impact-echo lab test 1

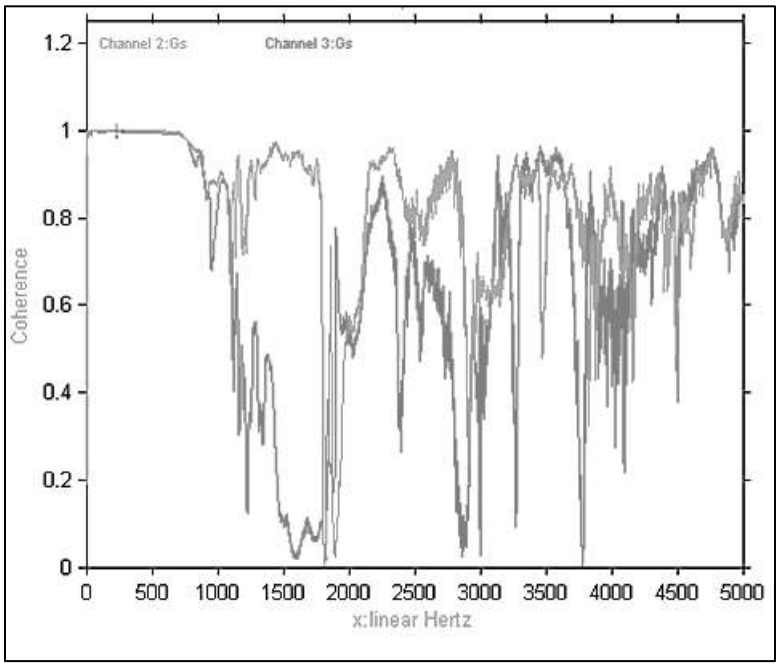

Figure 33: Coherence of impact-echo lab test 2

The lack of recorded vibration response is particularly explicit in Figure 34 and Figure 35. Both figures illustrate a large peak around 100 Hz and no other response.

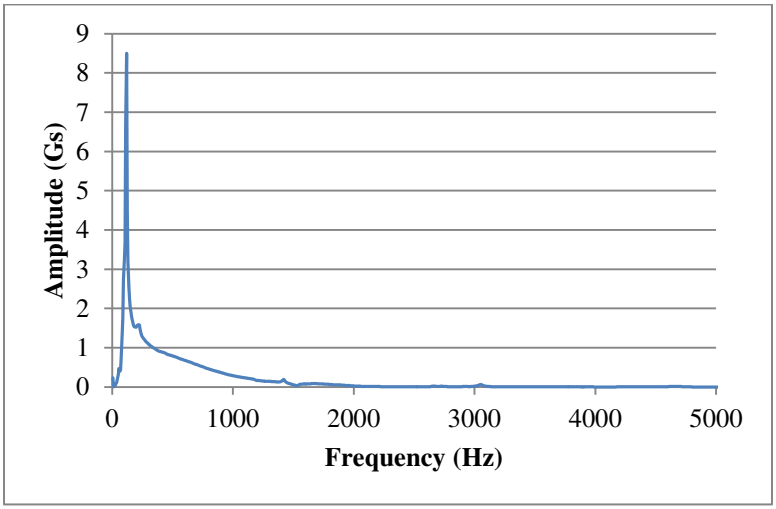

Figure 34: Amplitude spectrum for impact-echo field test 1

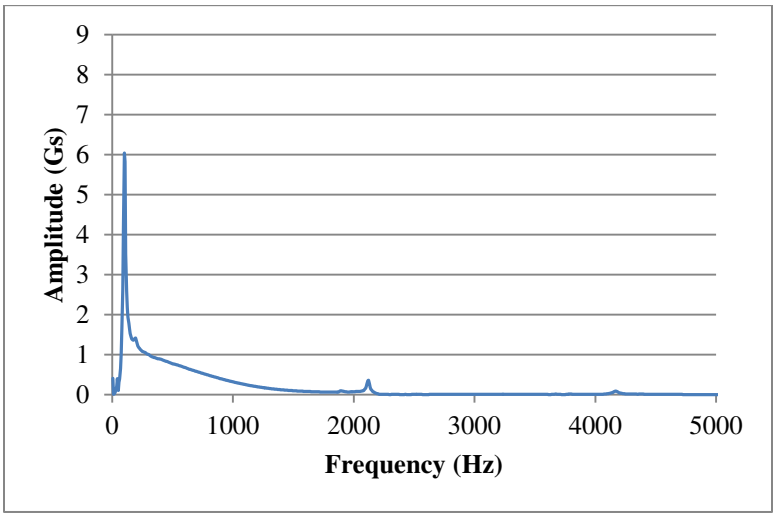

Figure 35: Amplitude spectrum for impact-echo field test 2

Coupled with the complications implicit with the impact hammer, the accelerometers were designed with a useful frequency range of 0.5 Hz up to 6000 Hz and

a resonant frequency of 10,000 Hz (PCB Piezotronics, 2002). The frequency range of 0.5 Hz up to 6000 Hz would be applicable for some of the tests conducted, where the frequency range is low, but when testing stones with varying cross sections and varying properties, it is often the case that the frequencies above 6000 Hz are relevant. Figure 36 illustrates this possibility where a stone with the given properties and cross-sectional dimensions of 0.4m requires a frequency range of 3700 Hz up to 10700 Hz. The values from Figure 36 were calculated based on theoretical eigenvalues as described in section 2.3. Figure 36depicts the user interface of the real-time impact-echo program (RIAP) discussed in section 4.4.

Theoretical Fundamental Mode Shapes

*0.6≤D/B≥2.0 *L≥3(Maximum of D or B)

Density (ρ)	2000	kg/m^3	Depth (D)	0.4	m
Poisson's Ratio (v)	0.25		Width(B)	0.4	m
Modulus of Elasticity (E)	2.00E+10	Pa	Length(L)	1.5	m
Cp(P-Wave Speed)	3464.102	m/s	D/B	1	
Cs(S-Wave Speed)	2581.989	m/s			

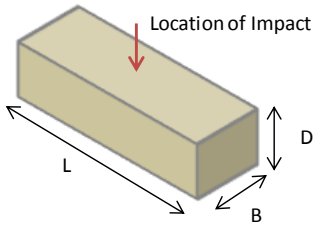

Aspect Ratio D/B	Beta	Fundamental Mode f1 (Hz)	Mode 2 (Hz)	Mode 3 (Hz)	Mode 4 (Hz)	Mode 5 (Hz)	Mode 6 (Hz)
1.00	0.87	3767	5312	7158	9230	10661	8815

Figure 36: Expected modes of vibration for a prospective stone specimen

With a resonant frequency of 10000 Hz, the model 393A03 accelerometer is limited to a reliable range of frequencies below 8000 Hz to minimize possibly resonant damage in the accelerometer, therefore limiting its applicability.

The testing in the field provided:

- Insight into the typical conditions particular to metamorphic stones in an ancient archeological site.

- The ability to observe the stones in the field allowing for a more in depth understanding of what difficulties researchers will experience in the future and how they may be addressed.
- Verification on the feasibility of the proposed method in terms of preserving the ancient blocks, ease of equipment transport, and the time required to conduct tests.
- Insight needed to acquire new testing equipment for use in lab testing and to develop the methodology for the rest of the study

On the other hand, due to equipment limitations, very little insight into the material properties of the stones or the structural characteristics of the stones could be obtained.

4.1.2 Lab Testing

Testing in the lab was conducted on a mortar block of dimensions 0.49 m x 0.56 m x 1.5 m, as discussed in section 3.1.2.1. Figure 37 depicts the mortar block and its supports.

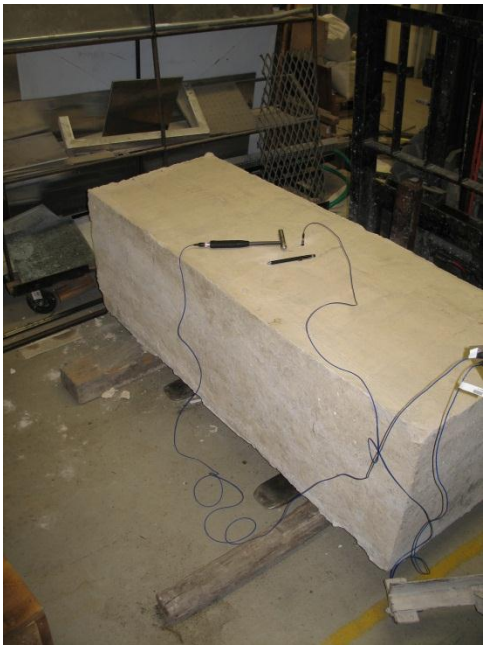

Figure 37: Mortar block on wooden supports

Two cylinders were cast to determine the material properties. After the mortar's material properties were determined, impact-echo testing was conducted on the mortar block. Lab testing results and discussion will be covered in this section, which includes material property determination, traditional impact-echo testing, and straight-line velocity tests.

4.1.2.1 Material Property Determination

Lab testing began with the casting of the mortar block and determination of the material properties. As previously discussed, the mortar block and two cylinders were cast simultaneously. The imperfect dimensions, resulting in an aspect ratio of 0.89, were the product of a formwork failure. While vibrating the mortar in the formwork, one of the corners burst and some loss of mortar occurred. The mortar formwork was repaired, as best as possible, but was unable to be repaired to its original state. As a result of this failure, finite element models with varying mesh sizes were created with identical

dimensions to the mortar block. It should be noted that the cross-section of the mortar block is not consistent throughout and it is unknown to what extent this variation may affect the impact-echo results.

The weight, volume, and density for each of the two cylinders, cast in conjunction with the mortar block, can be found in Table 8. The average density for both cylinders is also found in Table 8.

Table 8: Cylinder material properties

	Cylinder 1	Cylinder 2
Weight (kg)	4.091	4.134
Volume (m^3)	0.00164	0.00164
Density (kg/m^3)	2500	2515
Average Density (kg/m^3)	2508	

The density of the mortar block was very close to the goal density of stones in the field. The goal density, previously determined from field samples, was 2600 kg/m^3. Determination of the modulus of elasticity was done according to ASTM C469/C469M. The unabridged compression testing results for both mortar cylinders are presented in Figure 38.

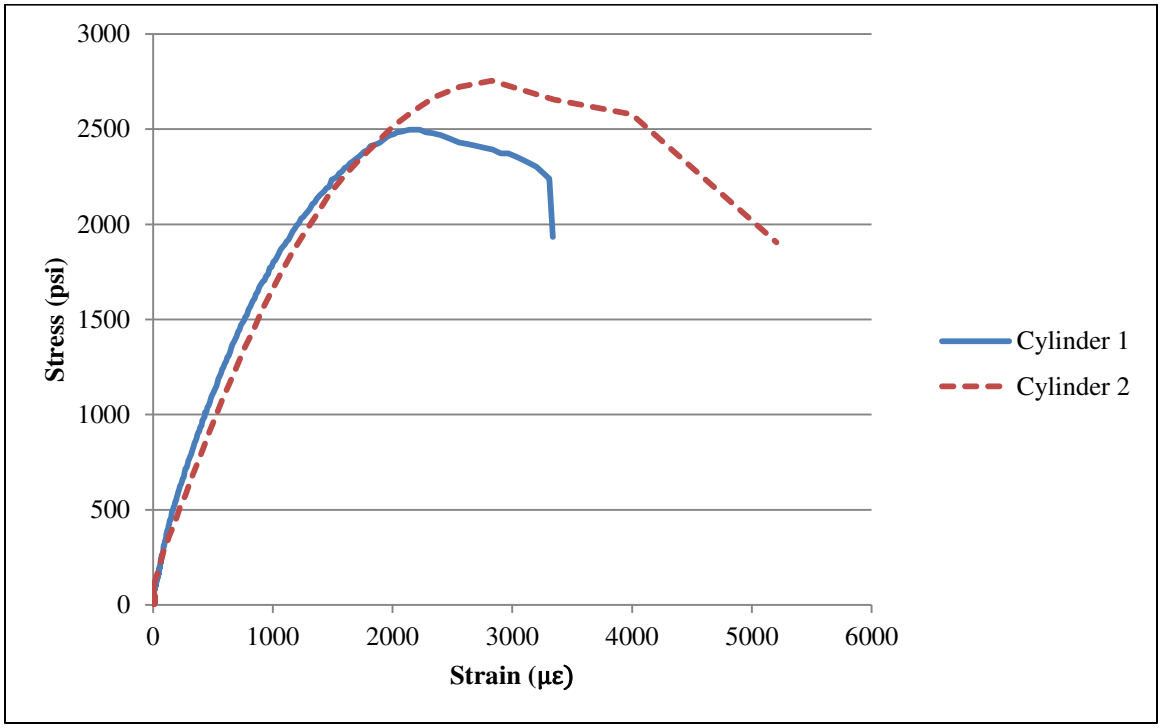

Figure 38: Complete stress vs. strain data of compression tests conducted on mortar cylinders

According to the ASTM standard, 40% of the ultimate load is to be considered in analysis (ASTM International, 2010). Figure 39 illustrates each cylinder's compression data within the applicable range as determined by ASTM C469/C469M.

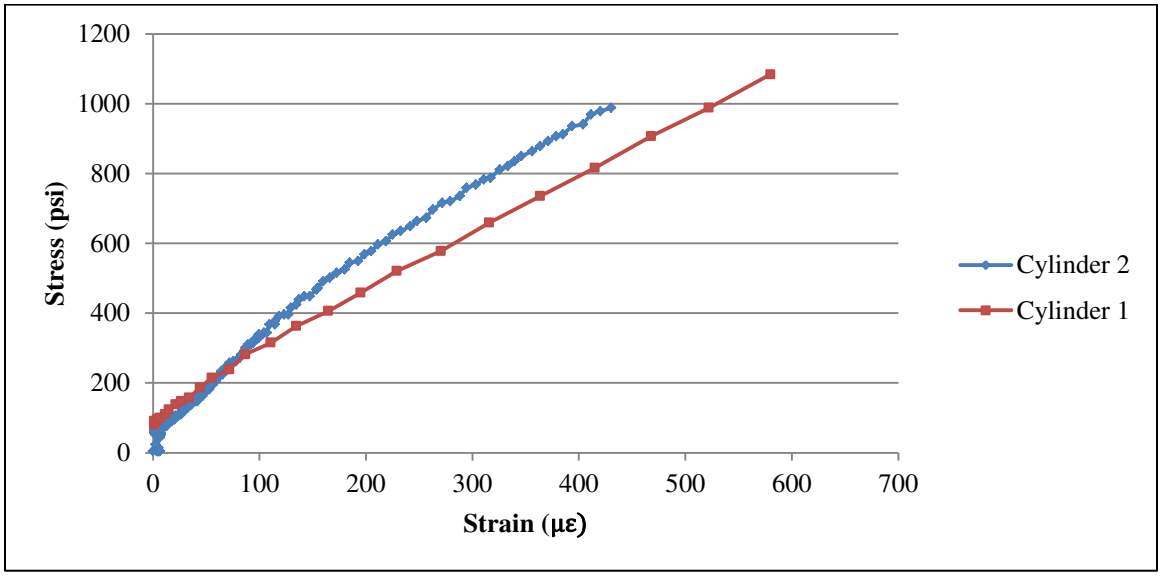

Figure 39: Stress vs. strain data of compression tests conducted on mortar cylinders following ASTM C469/C469M

The calculated moduli of elasticity and the average modulus of elasticity based upon the data from Figure 39 can be found in Table 9.

Table 9: Cylinder modulus of Elasticity

	Cylinder 1	Cylinder 2
Modulus of Elasticity (Psi)	1.725E+06	2.380E+06
Modulus of Elasticity (Pa)	1.189E+10	1.641E+10
Average Modulus of Elasticity (Pa)	1.42E+10	

In order to find the modulus of elasticity, the slope of the linear best-fit line was determined and recorded as the modulus of elasticity (E). The modulus of elasticity for each cylinder was initially recorded in pounds per square inch (Psi) per micro strain (με), which was converted to Psi and eventually converted to Pascal (Pa). The average

modulus of elasticity for the mortar block was determined to be 1.42E10 Pa, as seen in Table 9. This value is within the expected range of modulus of elasticity for a Portland-cement based material. Modulus of elasticity will vary depending on the water-cement ratio in any Portland-cement based product, and the mortar in this study reflects this variation with a variance of 17% from the expected value of 1.7E10 Pa (Essom Equipment for Engineering, 2007).

4.1.2.2 Traditional Impact-Echo Testing

Impact-echo testing in the lab on the mortar block provided information as to the coherence of each set of data, the excitation frequency, and the associated amplitude spectrums. As seen in Figure 40 and Figure 41, the typical coherence in the lab testing remained close to the desired value of unity (1.0) up to 8000 Hz. This covers the required frequency range based on expected natural frequencies determined through eigenvalue analysis.

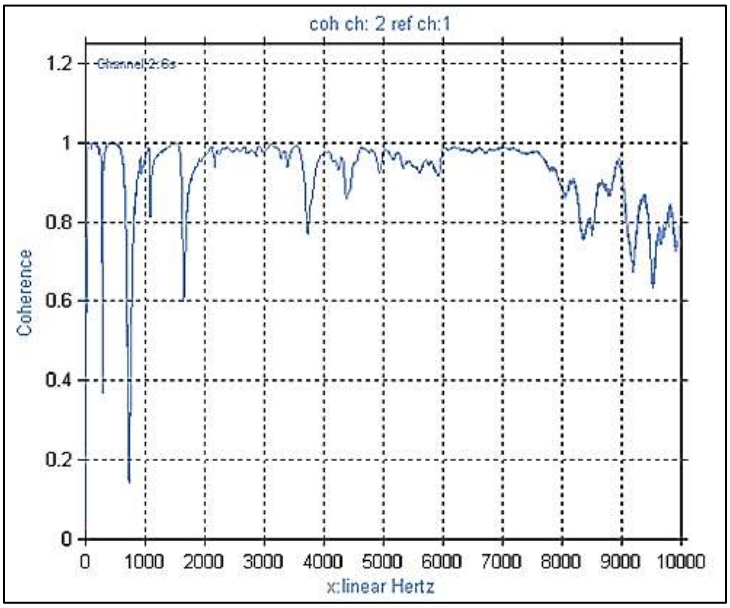

Figure 40: Coherence of impact-echo lab test 1

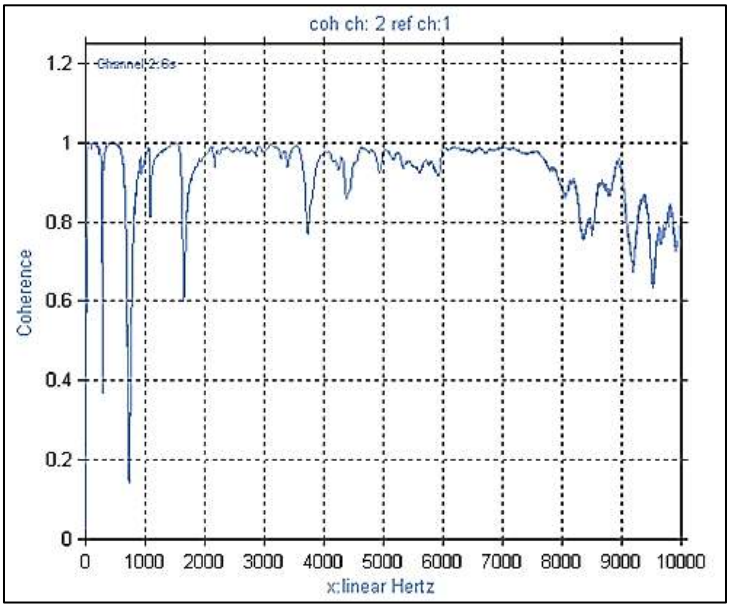

Figure 41: Coherence of impact-echo lab test 2

Figure 42 shows the elastic impact curves of the impact hammer excitation.

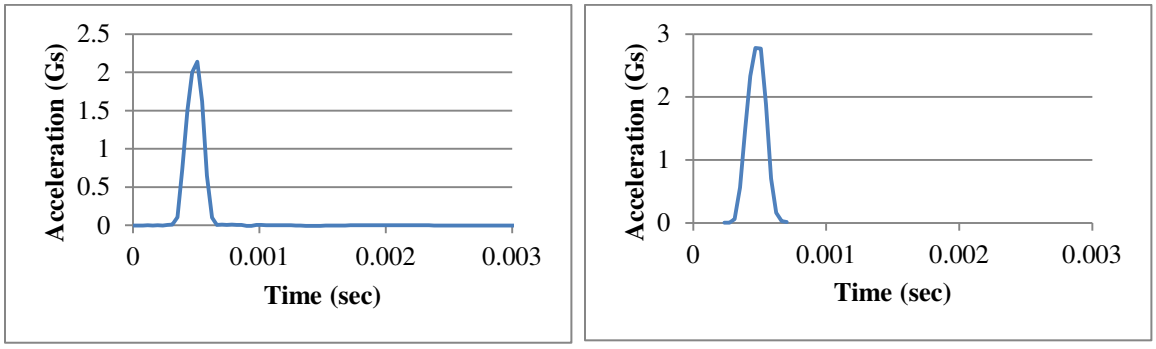

(a) (b)

Figure 42: Impact-hammer elastic impact of (a) lab test 1 and (b) lab test 2

By taking a FFT of the elastic impact data, the excitation frequency ranges were obtained. Test 1 had a maximum excitation frequency range of 6000 Hz and Test 2 had a maximum excitation frequency range of 6000 Hz. Following Sansalone's and Streett's recommendation, this allows for a useful range anywhere below 5000 Hz. The useful frequency range for lab testing is to the left of the dotted line.

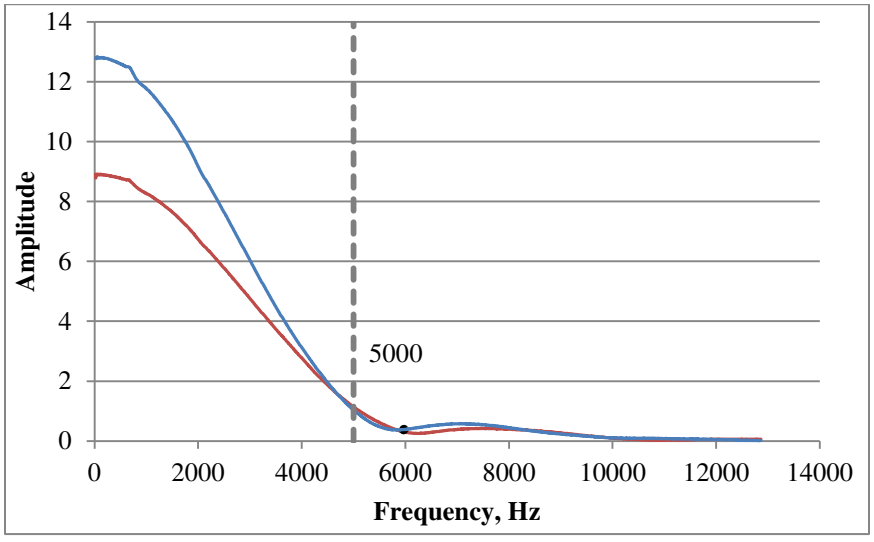

Figure 43: FFT of elastic impact on lab test 1 and 2

Straight-line velocity test conducted on the mortar block are represented by 3 select tests. The straight-line velocities as calculated in Table 10 provide an average p-wave speed of 2438 m/s.

Table 10: Straight-line velocity data

	Test 1	Test 2	Test 3	Average
Δt (sec)	0.000137	0.000117	0.000117	
P-Wave Speed (m/s)	2194	2560	2560	2438

It is important, with the current capabilities of SIGLAB, to keep in mind that the sampled frequency for these tests was 25600 Hz with a record time of 8192. Based upon these P-wave travel times, the sampled frequency, and the record time, expected systematic errors can reach 33% (Spectral Dynamics, 2001). SIGLAB restricts the user in this manner by having a maximum analysis bandwidth selection of 20,000 Hz.

The limitations of SIGLAB are especially important when considering the measurement of P-waves. When P-waves serve as the primary source of information for material property determination or in calculating the predicted response, the wave speed error will affect the accuracy of the results. While conducting straight-line velocity tests was inconclusive, regarding the particular velocities of the mortar block, the validity of the process has been previously established as a reliable means of wave speed determination (Hsiao, Cheng, Liou, & Juang, 2008). Another consideration for the straight-line velocity tests is the variation in the accelerometers used. The accelerometers used were not identical models and as a result experienced the excitation differently. The size of each accelerometer is different in addition to the volts per G that each

accelerometer measures. This creates a large spread in the time-series amplitudes and makes P-wave travel time analysis difficult.

The amplitude spectrums, obtained in lab testing, were analyzed over the cross-sectional range and eliminated the flexural modes of vibration. This allowed for an amplitude spectrum with a practical vertical scale. The amplitude spectrums were obtained by manually performing a FFT of the time-series data. Due to the difficulty of exporting a FFT from SIGLAB, FFTs were performed independently for ease of graphing.

The predominant frequencies in the amplitude spectrums were determined from Sansalone's and Streett's recommendations. The first mode was marked according to the statement that for a D/B ratio of 0.89, the first mode of vibration will be of considerably lower magnitude. The following modes of vibration were determined based solely upon the amplitude of the response spectrum (Sansalone & Streett, 1997). Two typical lab testing amplitude spectrums are presented in Figure 44 and Figure 45.

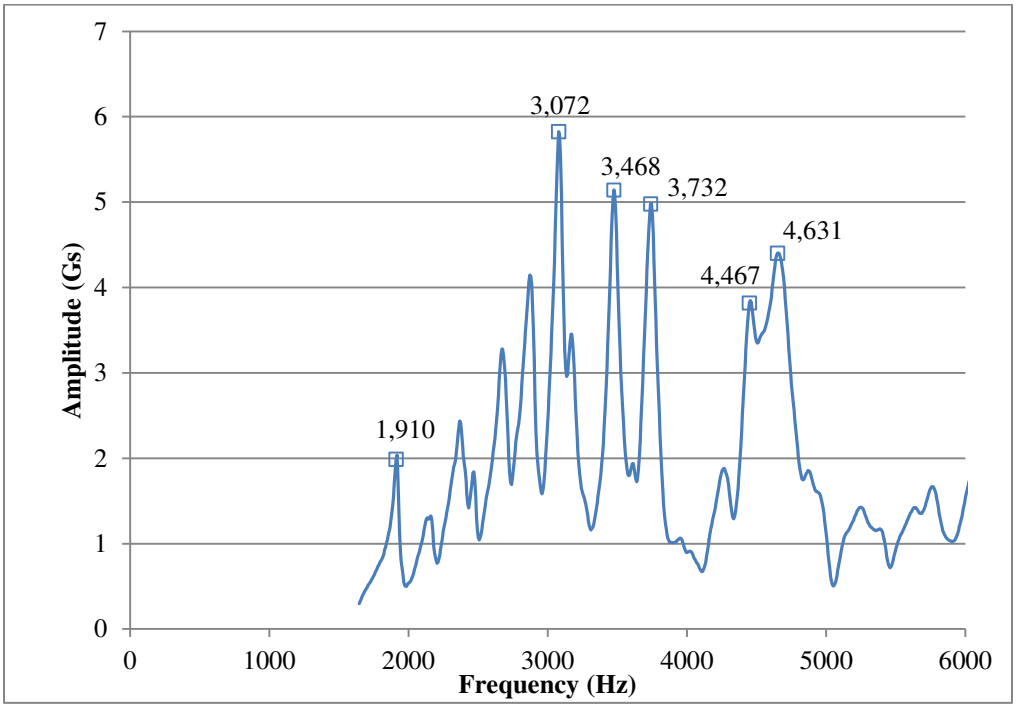

Figure 44: Amplitude spectrum for impact-echo lab test 1

Table 11 lists the predominant frequencies obtained in analysis of Figure 44.

Table 11: Predominant frequencies for lab test 1

Predominant Frequencies (Hz)					
Mode 1	**Mode 2**	**Mode 3**	**Mode 4**	**Mode 5**	**Mode 6**
1910	3072	3468	3732	4467	4631

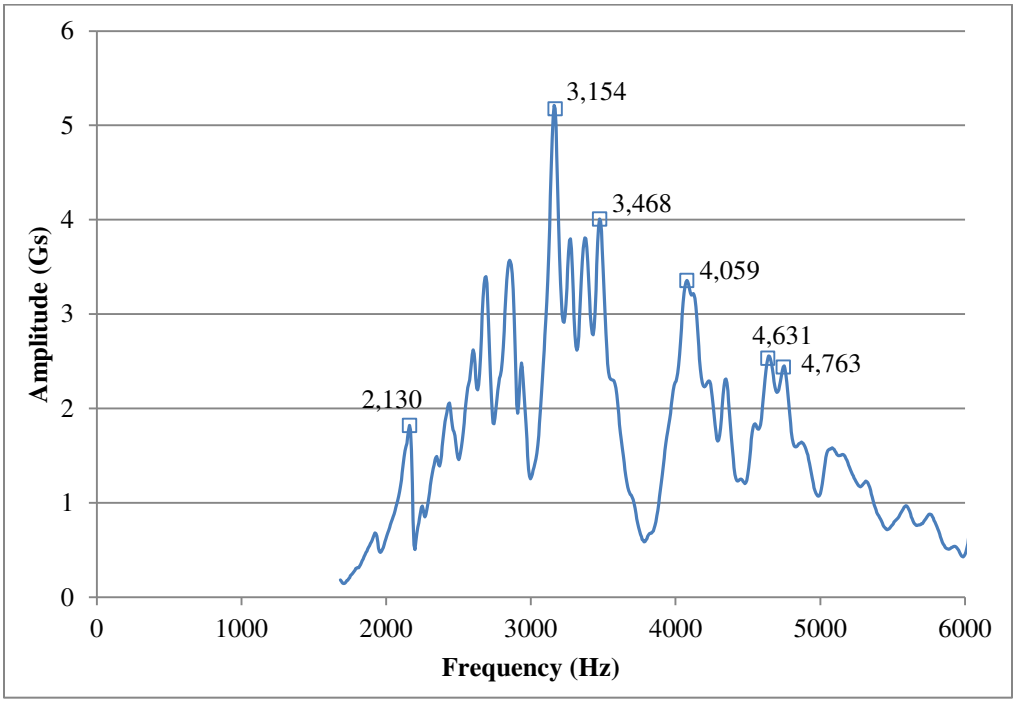

Figure 45: Amplitude Spectrum for impact-echo lab test 2

In Figure 45, the amplitudes of various frequencies are shown for a second impact-echo test. The predominant frequencies in this test are shown in Table 12. The values in Table 11 and Table 12serve as the primary frequency responses for impact-echo testing in the lab.

Table 12: Predominant frequencies for lab test 2

Predominant Frequencies (Hz)					
Mode 1	Mode 2	Mode 3	Mode 4	Mode 5	Mode 6
2130	3154	3468	4059	4631	4763

Possible combining of modes was accounted for in the analysis of the response spectrum. The limited frequency resolution of SIGLAB can combine multiple modes

into one mode if the resolution is too large. In order to avoid the issue of combined modes, a smaller frequency resolution would be necessary (Erdogmus, 2004).

As mentioned in section 2.1.5, the minimum length of a specimen should be 3 times the largest cross-sectional dimension for the theory used. In the case of the mortar block, for the eigenvalue analysis to be applicable, the length was determined to exactly match the minimum requirement. The cross-sectional dimensions were designed to be 0.5 m, but as a result of the formwork failure the dimensions were 0.49 m and 0.56 m. These dimensions require a minimum length of 1.68 m. The mortar block cast in the lab was spatially restricted to 1.5 m, due to the formwork. As a result, the mortar block is 0.18 m short in length to meet this requirement. Inadequate mortar block dimensions require special consideration when viewing the results. This variation in length affects the response spectrum. Traditional impact-echo testing conducted on a specimen with a specimen length at or near the minimum will present high flexural responses (Hill, McHugh, & Turner, 2000). This can be observed in the complete unabridged impact-echo results from the lab found in Appendix B: Supplemental Lab Testing Reference Material.

Impact-echo testing in the lab allowed for direct measurement of the excitation frequency. With the observation of coherence close to 1.0 over the cross-sectional vibration range, it was determined that the amplitude spectrums were reliable during lab testing. The frequency values obtained in the impact-echo testing are compared later in this chapter with the theoretical eigenvalue results and the finite element model results.

4.2 Finite Element Modeling

In this section, the finite element analysis results will be discussed. The FEA was conducted using the commercial software ANSYS. First, the data from FEA Set 1,the finite element models of varying aspect ratios, is covered, which includes Analysis A, B, C, and E. Next, the finite element models of the mortar block, FEA Set 2, are presented. FEA Set 2 includes one model with three different mesh sizes.

4.2.1 Modal Analysis of Varying Aspect Ratios (FEA Set 1)

Modal analysis was conducted on aspect ratios of 0.6, 1.0, and 2.0, and modal participation factors were recorded for every analysis. Figure 46 through Figure 48 are representative of the y-axis participation factors for all three aspect ratios. The results from each aspect ratio's analysis mimic the general trends presented in Figure 46 through Figure 48 and are available in Appendix C and Appendix D. Figure 46 illustrates the data from Analysis A, where all degrees-of-freedom were left free except for the connection to the supports. Table 6, found on 51explains the details of each test.

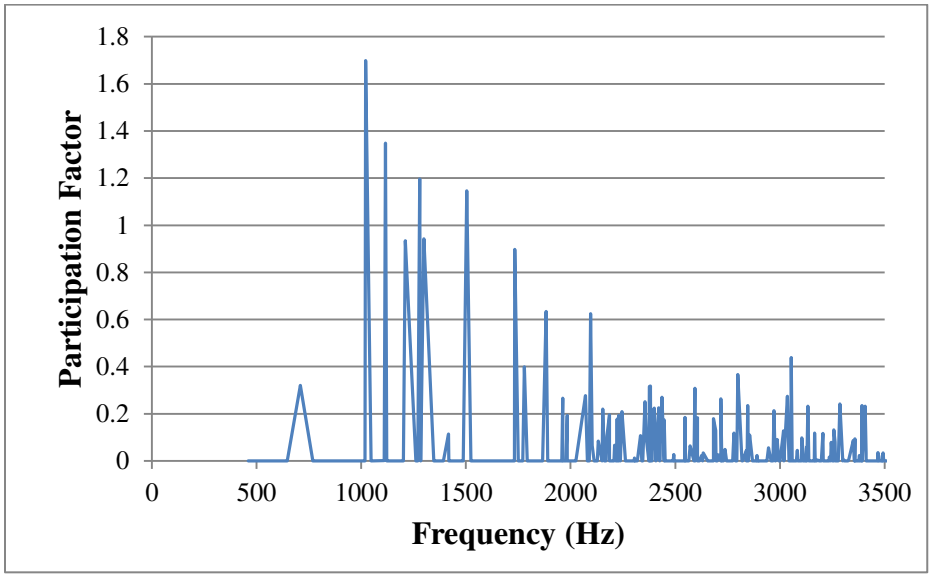

Figure 46: Typical participation factors for Analysis A

As observed in Figure 46 there are a large number of modes participating in the y-axis response. Selecting particular frequencies from Figure 46, correlating to the cross-sectional modes of vibration, would provide substantial difficulty due to the large number of frequencies with high participation factors and would be subjective. Analysis B was completed in response to these results.

Figure 47 illustrates the typical results from the Analysis B. In the Analysis B, the longitudinal degrees of freedom (z-axis) were restricted in addition to the specimen's connection to the supports. As seen in Figure 46, there are still a large number of modes with high participation factors.

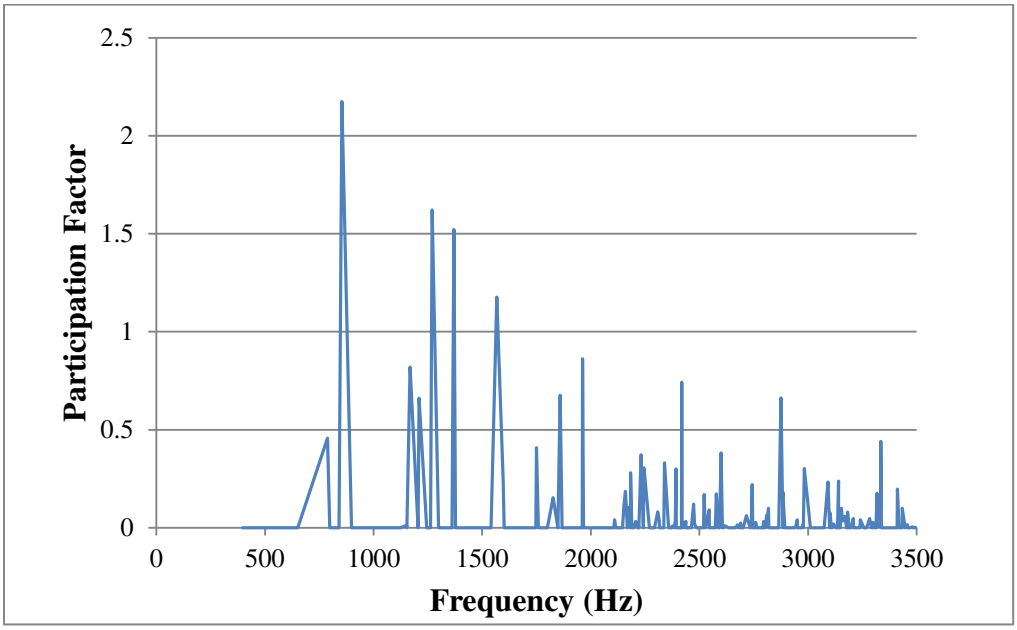

Figure 47: Typical participation factors for Analysis B

After completing these two analyses, further research was completed and it was then determined that thin sections would be most applicable to this study as described by Sansalone and Streett. Figure 48 depicts the results from Analysis C, where a thin slice of each model was analyzed. In Figure 48, the prominent frequency modes are graphed according to their participation factors.

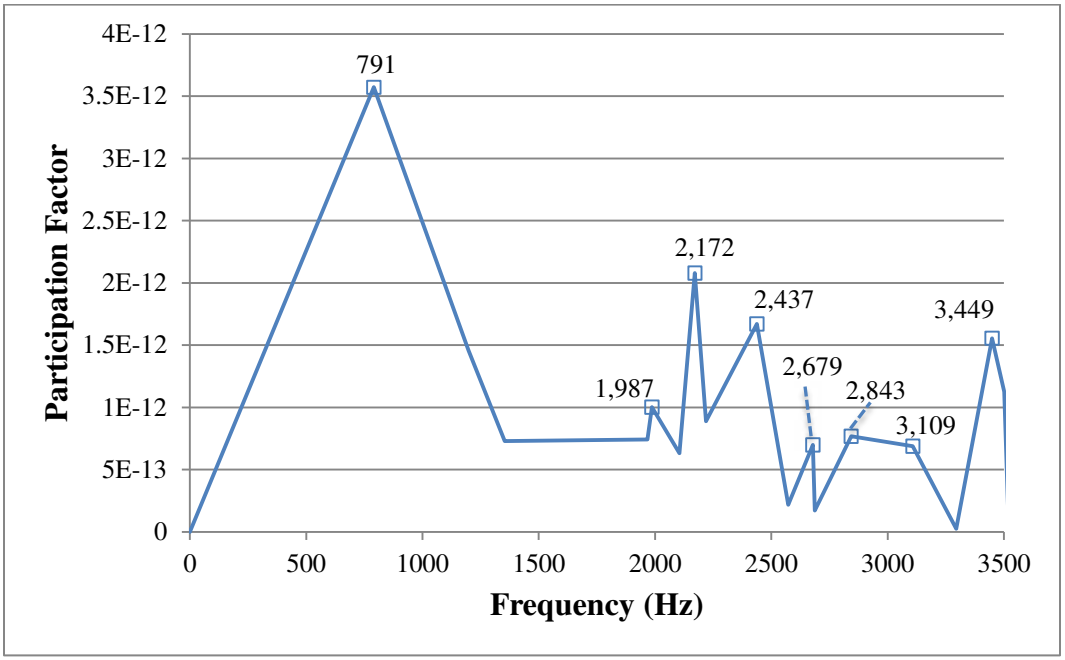

Figure 48: Typical participation factors for FEA set 3

The predominant frequencies are easily observed through their participation factors in Figure 48. These frequencies were recorded for each aspect ratio in order to compare with the theoretical eigenvalue analysis results. Table 13 shows the predominant frequencies of vibration according to their participation factors observed in Analysis C of FEA Set 1.

Table 13: FEA predominant frequencies of varying aspect ratios

	Aspect Ratio (D/B)		
	0.6	1	2
Mode 1 (Hz)	855	2004	791
Mode 2 (Hz)	1890	3107	2172
Mode 3 (Hz)	N/A	3874	2437
Mode 4 (Hz)	2601	5137	2679
Mode 5 (Hz)	3079	5862	2843
Mode 6 (Hz)	3354	4972	3449

Analysis E utilized optimized finite element meshes. These optimized meshes were the result of continued optimization of the finite element meshes in Analysis D, which corresponds to the mortar block (aspect ratio of 0.89). The optimization of meshes is covered in the following section. The results from the Analysis E are presented in Table 14. Each mode was selected based on the participation factors associated with that frequency. Sample mode shapes observed in Analysis E are shown in Figure 49. Only the mode shapes corresponding to the thin section analysis (Analysis E) are shown for each aspect ratio.

Table 14: Predominant frequencies of varying aspect ratios with optimized meshes

	Aspect Ratio (D/B)		
	0.6	1	2
Mode 1 (Hz)	1804	2002	1284
Mode 2 (Hz)	1905	3104	2130
Mode 3 (Hz)	2503	4097	2375
Mode 4 (Hz)	2503	5303	2651
Mode 5 (Hz)	2786	5732	2770
Mode 6 (Hz)	3270	4870	3173

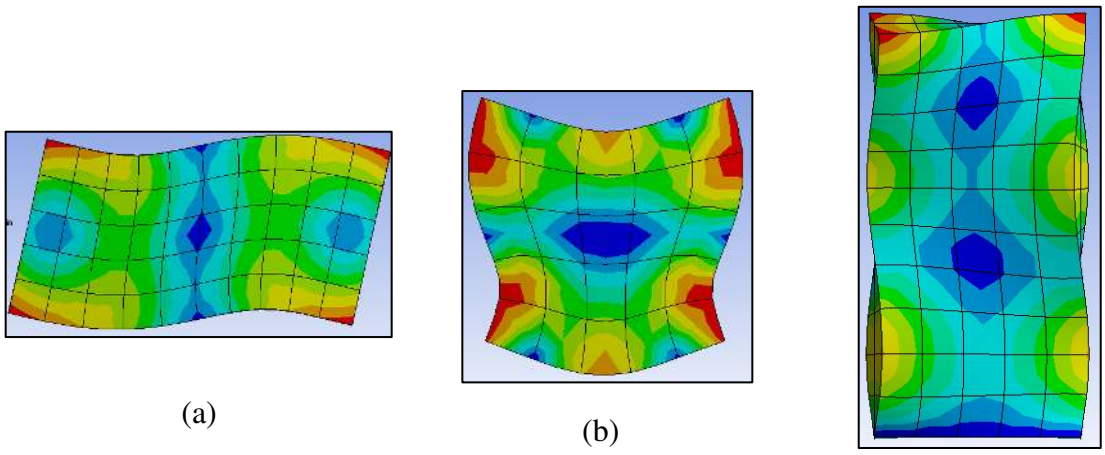

(a) (b) (c)

Figure 49: Various mode shapes for aspect ratios of (a) 0.6, (b) 1.0 , (c) 2.0

4.2.2 Modal Analysis of the Mortar Block (FEA Set 2)

This section provides the results and discussion pertaining to the finite element analysis conducted on the mortar block (Analysis D), which had an aspect ratio of 0.89. This FEA set was conducted to verify the FEA with experimental lab data, and eigenvalue analysis. Figure 50 through Figure 52 graph the predominant frequencies observed in FEA models with coarse, medium, and fine mesh, respectively. The theoretical eigenvalue modes of vibration (dashed lines) are also provided for visual comparison.

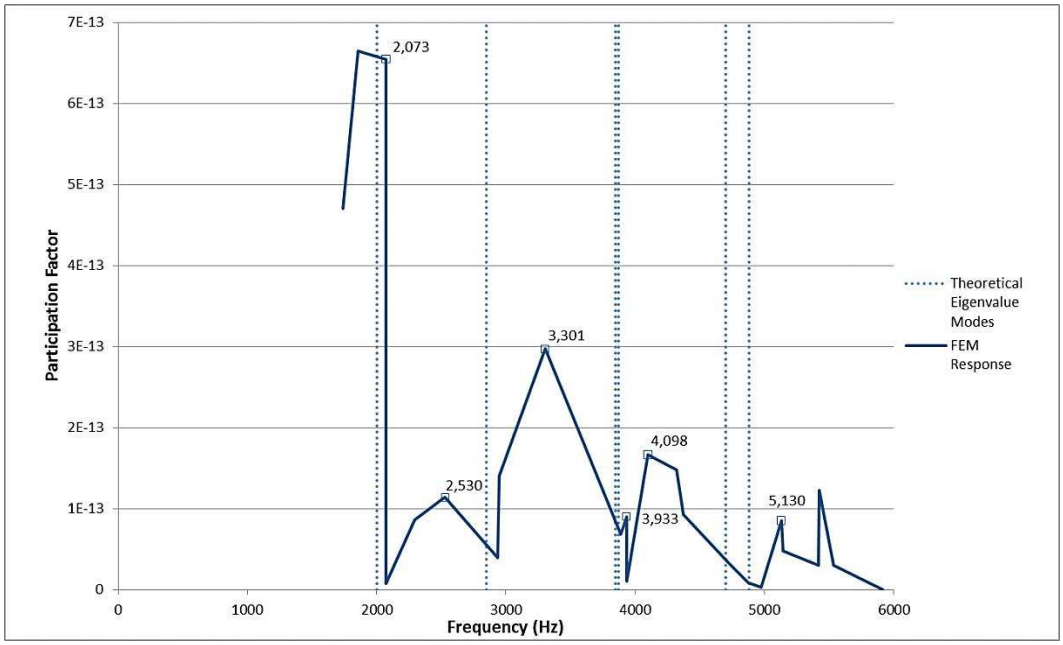

Figure 50: Coarse FEM mesh modal analysis resutls compared to theoretical values (aspect ratio 0.89-mortar block)

As seen in Figure 50, the first predominant frequency correlates closely to the theoretical values, while the remaining frequencies seem scattered.

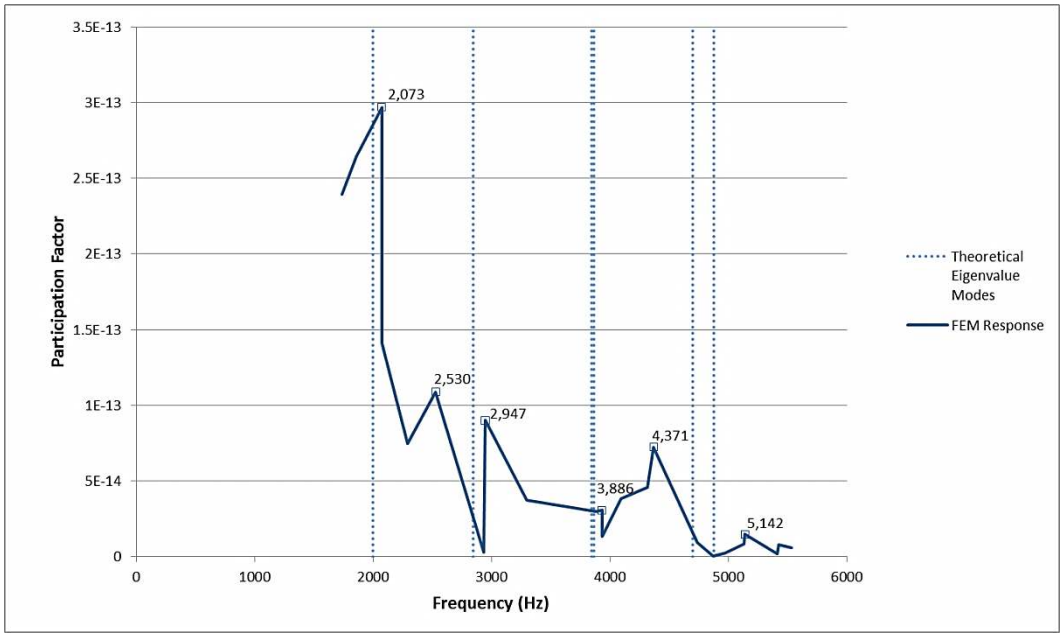

Figure 51: Medium FEM mesh modal analysis results compared to theoretical values (aspect ratio 0.89-mortar block)

Figure 51, showing results from the medium mesh, estimates the 1st mode with reasonable accuracy, but also begins to display a closer match the theoretical values for the next two modes.

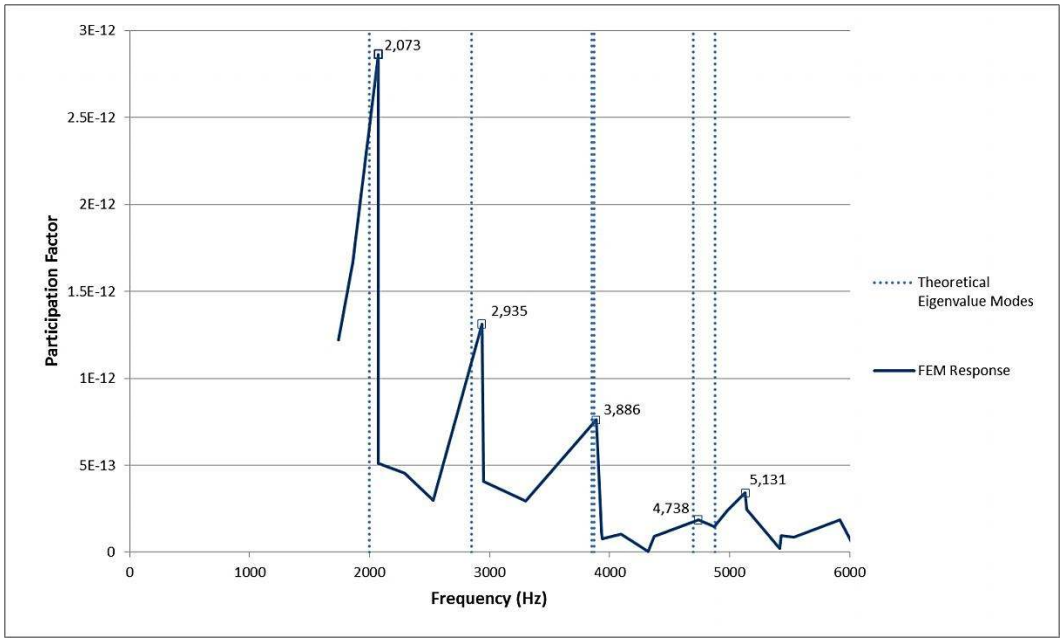

Figure 52: Fine FEM mesh modal analysis results compared to theoretical values (aspect ratio 0.89-mortar block)

As seen in Figure 52, the trend observed from coarse to medium meshes continues to evolve. The first predominant mode stays unaffected from mesh size, while the second and third modes distinguish themselves. In the case of the fine mesh, the first three modes of vibration closely correlate to the theoretical values, while the fourth and fifth, although relatively close, still lack clarity. The predominant frequencies, as seen in Figure 50, Figure 51, and Figure 52 are provided in Table 15.

Table 15: Theoretical and FEM results with varying mesh sizes

	Coarse Mesh	Medium Mesh	Fine Mesh
Mode 1 (Hz)	2073	2073	2073
Mode 2 (Hz)	2530	2947	2935
Mode 3 (Hz)	3301	3866	3886
Mode 4 (Hz)	3933	3866	3886
Mode 5 (Hz)	4098	4371	4738
Mode 6 (Hz)	5130	5142	5131

4.3 Comparison of Results and FEA Verification

After obtaining the results from each individual testing and analysis phase, both the finite element analysis results and the impact-echo testing results were compared with the theoretical eigenvalue results. The finite element comparative analyses consist of Analysis C, D, and E. The impact-echo testing comparative analysis consists of two typical impact-echo tests conducted on the mortar block.

4.3.1. Finite Element Analysis and Theoretical Eigenvalue Analysis

Predominant frequencies for the various modes of vibration, as seen in Table 13, are compared with the theoretical frequencies based on theoretical eigenvalue results. This comparative analysis can be seen in Table 16. Analysis C consisted of thin sections with non-optimized meshes subjected to modal analysis for each aspect ratio (0.6, 1, 0, and 2.0). The % error is calculated using theoretical eigenvalues as the baseline.

Table 16: Comparison of Analysis C and theoretical eigenvale results

	Aspect Ratio (D/B) 0.60			Aspect Ratio (D/B) 1.00			Aspect Ratio (D/B) 2.00		
	Theoretical Eigenvalue	FEM	% Error	Theoretical Eigenvalue	FEM	% Error	Theoretical Eigenvalue	FEM	% Error
Mode 1 (Hz)	1711	855	50.04%	2127	2004	5.78%	1173	791	32.59%
Mode 2 (Hz)	1831	1890	3.22%	2999	3107	3.61%	2124	2172	2.26%
Mode 3 (Hz)	2447	N/A	N/A	4041	3874	4.13%	2417	2437	0.82%
Mode 4 (Hz)	2533	2601	2.70%	5211	5137	1.42%	2617	2679	2.38%
Mode 5 (Hz)	3183	3079	3.27%	6019	5862	2.61%	3004	2843	5.36%
Mode 6 (Hz)	3269	3354	2.62%	4977	4972	0.10%	3426	3449	0.66%
		Average	12.37%		**Average**	2.94%		**Average**	7.34%

As seen in Table 16, the error ranges from 0.66% all the way up to 50.04%. For a majority of the vibrational modes, excluding the first mode, the errors are below 5.36%. On the contrary, the first predominant mode is often the major contribution to the calculated error.

Table 17, illustrates Analysis D (aspect ratio 0.89) results, where thickness and mesh size of each model was adjusted for optimization of the cross-sectional modes of vibration. The theoretical eigenvalue modes, calculated using the properties and dimensions of the mortar block, are provided for comparison. The % error for each mode and the average % error are provided using theoretical eigenvalues as the baseline.

Table 17: Comparison of Analysis D with varying mesh sizes and theoretical eigenvalue results

	Theoretical Eigenvalues	Coarse Mesh	% Error	Medium Mesh	% Error	Fine Mesh	% Error
Mode 1 (Hz)	1999	2073	3.70%	2073	3.70%	2073	3.70%
Mode 2 (Hz)	2849	2530	11.20%	2947	3.44%	2935	3.02%
Mode 3 (Hz)	3848	3301	14.22%	3866	0.47%	3886	0.99%
Mode 4 (Hz)	3868	3933	1.68%	3866	0.05%	3886	0.47%
Mode 5 (Hz)	4698	4098	12.77%	4371	6.96%	4738	0.85%
Mode 6 (Hz)	4878	5130	5.17%	5142	5.41%	5131	5.19%
		Average	8.12%	**Average**	3.34%	**Average**	2.37%

The coarse, medium, and fine meshes have average % errors of 8.12%, 3.34%, and 2.37%, respectively. It is important to consider the computation time required for each test, in order to assess the efficiency of the process. In this particular study, the coarse mesh analysis was completed in less than 5 minutes while the medium mesh analysis required 30 minutes to complete. The fine mesh required over an hour and a half to complete the analysis. While the computation time required is subjective to the computer hardware, for this study, it was determined that further analysis would provide minimal reduction in % error for the increased computation time. This conclusion is based on the reduction of error, between the medium mesh and the fine mesh, of 0.97% for an increased computation time of 1 hour.

Analysis E, which was completed based upon the mesh optimization developed in Analysis D, displayed a noticeable reduction in the error of the first mode of vibration for all aspect ratios between coarse and fine meshes (Table 17).

Table 18: Comparison of the FEM with varying optimized mesh sizes and theoretical results

	Aspect Ratio (D/B) 0.60			Aspect Ratio (D/B) 1.00			Aspect Ratio (D/B) 2.00		
	Theoretical Eigenvalue	FEM	% Error	Theoretical Eigenvalue	FEM	% Error	Theoretical Eigenvalue	FEM	% Error
Mode 1 (Hz)	1711	1804	5.42%	2127	2002	5.87%	1173	1284	9.42%
Mode 2 (Hz)	1831	1905	4.04%	2999	3104	3.51%	2124	2130	0.29%
Mode 3 (Hz)	2447	2503	2.28%	4041	4097	1.38%	2417	2375	1.75%
Mode 4 (Hz)	2533	2503	1.17%	5211	5303	1.77%	2617	2651	1.31%
Mode 5 (Hz)	3183	2786	12.47%	6019	5732	4.77%	3004	2770	7.79%
Mode 6 (Hz)	3269	3270	0.05%	4977	4870	2.15%	3426	3173	7.40%
		Average	4.24%		**Average**	3.24%		**Average**	4.66%

The % error from Analysis E, which included modal analysis of thin sections with optimized meshes, is 4.24%, 3.24%, and 4.66% for each aspect ratio of 0.6, 1.0, and 2.0,

respectively. These results when compared to the % error observed using coarse mesh models produced error at or below the previous values. For an aspect ratio of 1.0, the % error remained the same at 3%. In the case of the aspect ratios of 0.6 and 2.0, the % error decreased from 12.27% down to 4.24%, and from 7.34% down to 4.66%, respectively. The resulting decreases of 8.13% and 2.68% correspond to the aspect ratios of 0.6 and 2.0, respectively. This reduction in error is attributed to the newly discretized meshes, which further optimized the models.

Comparison of the FEA results and the theoretical eigenvalues provides a reliable measurement of their correlation resulting in verified FEAs (Erdogmus, Boothby, & Smith, 2007). When comparing the information from this study, the FEA and the theoretical eigenvalues, average % errors were less than 5% for the varying aspect ratios, and as low as 2.37% for the aspect ratio of 0.89. Now that confidence is gained in the analytical methods through cross verification, impact-echo results will be compared to theoretical results to validate the feasibility and accuracy of the proposed testing setup.

4.3.2. Impact-Echo Testing and Theoretical Eigenvalue Analysis

The impact-echo results discussed in section 4.1.2 were compared to the theoretical eigenvalues and the % error was calculated using the theoretical eigenvalues as a baseline. The comparison between two typical impact-echo tests and the theoretical values can be seen in Table 19.

Table 19: Impact-echo lab results compared to theoretical eigenvalues

	Theoretical Eigenvalues	Lab Test 1	% Error	Lab Test 2	% Error
Mode 1 (Hz)	1999	1910	4.45%	2130	6.55%
Mode 2 (Hz)	2849	3072	7.83%	3154	10.71%
Mode 3 (Hz)	3848	3468	9.88%	3468	9.88%
Mode 4 (Hz)	3868	3732	3.52%	4059	4.94%
Mode 5 (Hz)	4698	4467	4.92%	4631	1.43%
Mode 6 (Hz)	4878	4631	5.06%	4763	2.36%
		Average	5.94%	**Average**	5.98%

As seen in Table 19, the average % error for each test was just below 6%. The range of % error went from 1.43% up to 10.71%. When considering the variation between the theoretical eigenvalues and the impact-echo results, it is important to consider the many factors affecting the response spectrums. The variations in cross-sectional dimension of the mortar block as well as the limited length of the mortar block both affect the amplitude of the response and location of predominant frequencies. It is important to consider that the theoretical eigenvalues are based upon material properties measured from cylinders or assumed properties, in the case of Poisson's ratio. The theoretical values also assume a homogenous isotropic solid. Although this may have been replicated with the mortar block as closely as possible, it is extremely difficult to ensure that the block had a uniform composition throughout. Taking these factors into consideration, the variation between impact-echo results and the theoretical results of 6% is good. As a result, the current impact-echo testing equipment and setup can be assumed to be feasible within the range of this study.

A comparison between the FEM with the fine mesh and the impact-echo lab tests can be found in Table 20. These results illustrate the correlation between the FEA and the impact-echo testing conducted in the lab.

Table 20: Impact-echo lab results compared to FEA results from the fine mesh

	Fine Mesh	Impact-Echo Test 1	% Error	Impact-Echo Test 2	% Error
Mode 1 (Hz)	2073	1910	7.86%	2130	2.75%
Mode 2 (Hz)	2935	3072	4.67%	3154	7.46%
Mode 3 (Hz)	3886	3468	10.76%	3468	10.76%
Mode 4 (Hz)	3886	3732	3.96%	4059	4.45%
Mode 5 (Hz)	4738	4467	5.72%	4631	2.26%
Mode 6 (Hz)	5131	4631	9.74%	4763	7.17%
		Average	7.12%	**Average**	5.81%

Average errors of 7.12% and 5.81% were observed in this comparison and are also based on magnitude as in previous comparisons. A summary correlating the FEA results and the lab testing results with the baseline values (eigenvalue analysis), presented in results give further confidence between the FEA results, the theoretical eigenvalues, and the impact-echo results.

Table 21: Summary of error when comparing lab testing and FEA to theoretical eigenvalue analysis

	% Error from Eigenvalue Analysis	
Aspect Ratio	**Lab Testing**	**FEA**
0.89	5.96% (Table 19)	2.37% (Table 17)
0.60	n/a	4.24% (Table 18)
1.00	n/a	3.24% (Table 18)
2.00	n/a	4.66% (Table 18)

4.4 Real-time Impact-echo Analysis Program Development

The relatively low error encountered when comparing lab experiments and FEA results to theoretical eigenvalue analysis results, provide the necessary justification for the use of the theoretical method developed by Sansalone and Streett. As a result, the eigenvalue methodology was used in the creation of a real-time impact-echo analysis program (RIAP). RIAP was developed in Microsoft Excel for use in the field to allow for immediate comparison to theoretical results and assess the condition of rectangular blocks within certain dimensional limits. RIAP requires either a) P-wave velocity, or, b) raw dimension data and material properties in order to output the expected baseline response.

This program allows for comparison of field results and theoretical results in real-time. A user in the field will be required to measure the primary cross-section of the specimen and the overall length and then input this data into RIAP. Once dimensions are input, the modulus of elasticity, Poisson's ratio, and density are input or the P-wave speed may be used as a substitute for all three properties. Upon entering all of the required information, RIAP will output the shape factor, aspect ratio, and the first six frequencies of the expected response. Given this information, the tester can then compare their peak frequencies, obtained in the impact-echo test with the theoretical values and immediately determine the general structural status of the specimen. RIAP provides streamlined testing and aids in an efficient block assessment testing process.

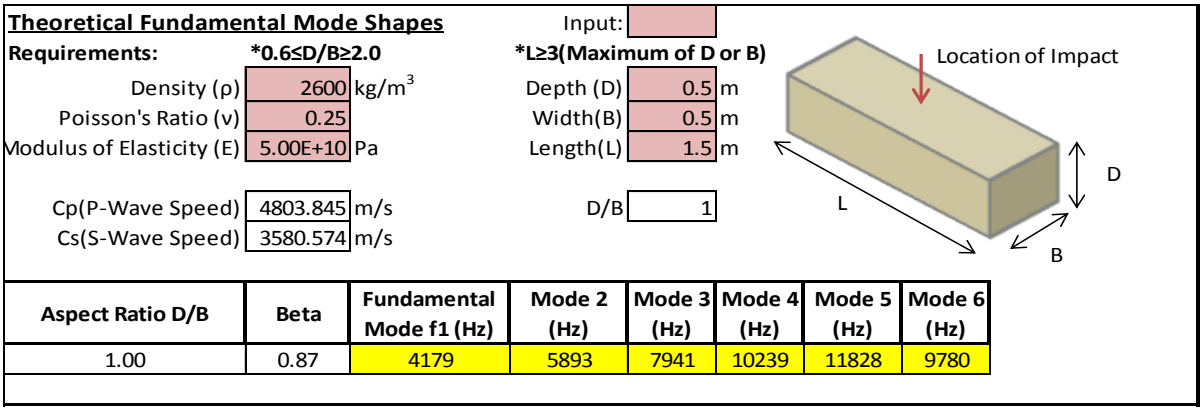

Figure 53: Real-time impact-echo analysis program user interface

RIAP functions by first taking the input data of depth and width and then calculating the aspect ratio (D/B). Once this is done, the program calculates the P-wave speed based upon the density, Poisson's ratio, and modulus of elasticity by Equation 1. As an alternative, the P-wave speed can be directly input on an alternative user-interface. Once the P-wave speed is calculated, RIAP selects β, based on the aspect ratio, and calculates the first fundamental mode based on Equation 7. After the fundamental mode of vibration is calculated, the fundamental frequency is multiplied by the coefficients from Table 1. Once the first six modes are calculated, the program displays these on the main user interface. All these calculations are done simultaneously and require no other user input.

It is important to consider that the functionality of this program is restricted by a few assumptions. First, in order to use this program, the user must be able to measure the P-wave speed or the required properties. The user can make engineering judgment to select these parameters, but must consider how they will affect the accuracy of the

results. The specimen must also be within the specified aspect ratio range of 0.6 to 2.0. If the user is beyond this range, the program will display an error message. These two requirements must both be satisfied for RIAP to output a predicted response. Assuming the user is within the required range of aspect ratios and is able to provide adequate information for a predicted response, it is also important to consider the applicability of the results obtained from the program.

4.5 Special Considerations for Impact-Echo Testing

RIAP, while limiting some possible sources of error, cannot eliminate all errors. In this specific experiment, the mortar block is assumed to have homogenous and isotropic properties. This is not always a reliable assumption given the metamorphic nature of many stones. As described previously, marble and other metamorphic stone is a material with varying mineral composition. This characteristic of marble and metamorphic stones cannot be ignored in impact echo testing. Wave propagation will differ when testing marble perpendicular to the grain patterns or parallel to the grain patterns. This specific feature of marble will alter the wave speed and therefore the frequencies and mode shapes (Popovics, J. S., 1997). Therefore, impact-echo testing, wave propagation and wave speed variation need to be taken into consideration as RIAP assumes homogeneous and isotropic solids.

It is recommended that straight-line velocity tests be conducted prior to impact-echo testing to validate the properties of the test specimen. Completing straight-line velocity tests will provide direct velocity measurements, which can then be compared to calculated wave speeds based upon assumed specimen properties. This will allow for an

iterative evaluation of the specimen's material properties. Even with the evaluation of the wave speed in both directions, it is difficult to understand how wave speed variation and propagation will affect the impact-echo response due to the complex nature of wave reflections.

4.6 Additional Impact-Echo Testing Uses

Impact-echo testing not only applies to rectangular blocks, but can also be used to determine plate thickness, cracks in plates, shallow delaminations, surface cracks, bond-quality in concrete/asphalt overlays, structural integrity of hollow cylinders or circular sections, or thickness of walls. These are only a few of the examples of how impact-echo can be utilized.

In particular to this study, the use of impact-echo testing can be used to determine width or depth of in-situ stones or material composition. In order to determine the width or depth of an in-situ stone, a traditional impact-echo test can be conducted on the exposed face and the time between P-wave arrivals can be multiplied by the P-wave speed to determine the dimension of question. The material composition can be determined with regard to the modulus of elasticity, Poisson's ratio, and density by solving Equation 1 for E, ρ, or ν. Two of the parameters must be assumed in order to solve for the other, but often density can be easily measured and Poisson's ratio varies little within a single material type (Essom Equipment for Engineering, 2007). This procedure can be iterative to determine the most accurate material properties.

While simple in process, in-situ thickness determinations must also consider the nature and location of the unexposed contact surfaces. Different materials have varying acoustic impedances and will therefore affect the degree of wave reflection. Air has very high acoustic impedance, where soil has much lower impedance producing the possibility of minimal wave reflection (Carino, 2001). In this case, if the unexposed surfaces of a specimen are in close contact with soil, or any material with low acoustic impedance, a decreased wave reflection may occur, altering the response spectrum.

Chapter 5: Conclusions and Recommendations for Future Work

In this chapter first the conclusions drawn from the study are presented followed by recommendations for future work.

5.1 Conclusions

1. Field testing provided experience with impact-echo testing methodologies and exposure to a range of field conditions significant to the study

Field testing at Antiochia ad Cragum created an environment for rapid knowledge acquisition from exposure to the archaeological site and initial attempts at impact-echo testing. A preliminary survey of the building stones provided an understanding and appreciation of the various building stone conditions. In this survey, the building stone sample illustrated a large variation with regard to their dimensions, degrees of damage, and surface conditions. While many small variances were observed between stones, the majority of the wall blocks of the temple are of similar cross-sectional dimensions (aspect ratio of 1.0) and of similar material characteristics. This allowed for a more focused approach while assessing the applicability of NDT techniques. Another benefit to field testing was the exposure to environmental conditions and restrictions including the weather and availability of power. Experiencing the heat provided insight into hardware sensitivity and mounting adhesive difficulties.

2. Impact-echo testing is chosen as the most applicable non-destructive testing (NDT) method

Given the large sample of stones on the job site, it was important to select a NDT method that could satisfy the general structural assessment required, but was cost effective and readily available. In addition, it was important to select a NDT method that could provide future assessment beyond the existing study.

The availability of impact-echo testing equipment provided a clear path for the direction of this study. Ultrasonic pulse velocity testing was considered, but deemed to be too costly and labor intensive. As a result of these considerations, the use of impact-echo testing was initially chosen and used in the field; however, its feasibility had to be proven as discussed in conclusion 1. Based on knowledge gained in the field and previous studies, new impact-echo equipment was obtained to further increase its accuracy and feasibility for the case at hand. Impact-echo testing subsequently commenced and amplitude spectrums obtained.

3. Impact-echo analysis methods compared well (within 2.37%) with theoretical results

The FEA on whole block models (Analysis A and B) provided little information into the response of each model while the participation factors of the whole block models lacked a definitive response in regard to its correlation with cross-sectional modes of vibration, using thin sections as finite element models (Analysis C, D, and E) provided more distinct responses. Originally, modal analysis on the thin sections with varying aspect ratios had errors of up to 12.37%. The modal analysis of the mortar block model (aspect ratio 0.89) saw its error reduced from 8.12% to 2.37% through mesh

optimization. This mesh optimization when applied to the varying aspect ratios reduced the original error from 12.37% to 4.66%. There was better correlation for the mortar block model (aspect ratio 0.89) because values could be experimentally validated.

4. Selected impact-echo equipment and utilized lab testing methods provide a reliable structural assessment tool to within 6% error.

The results gathered from impact-echo testing when compared to the theoretical eigenvalue analysis results saw errors at a maximum of 10.71% error between individual modes and averages just below 6%. Errors of 6%, although altering the amplitude spectrums, will not affect the overall general structural assessment of stones. This is due to the ability to detect flaws by comparing general trends between impact-echo responses rather than subtle variations.

Straight-line velocity tests, although a primary element of impact-echo testing, are not required to utilize impact-echo testing. However, straight-line velocity tests can be used to provide P-wave speeds for RIAP and allow for verification of the assumed properties. Therefore, the 33% error experienced in straight-line velocity tests has limited influence on the validity of impact-echo testing and results.

5. Proposed impact-echo testing methods in conjunction with RIAP allow for analysis of stones in real-time

Impact-echo testing equipment currently available to this study provides an adequate range for thorough frequency analysis within the scope of this study. As a result, the existing equipment can be viewed as satisfactory for the range of tests. The

impact-echo equipment, when employed with the prescribed testing methods, provided errors to within 6% when compared to theoretical values. In addition, RIAP proved to be a reliable assessment tool based on the 2.37% error between eigenvalue analysis and modal analysis. RIAP also provides real-time impact-echo response baselines. The limited error of RIAP, and the ability of RIAP to produce baseline response spectrums quickly and in real-time for a number of blocks will make it a very useful tool in large and complex condition assessment projects, such as the archaeological site used in this study.

5.2 Recommendations for Future Research

Recommendations pertaining to the continued research and continued use of impact-echo testing is covered in this section. Impact-echo testing as it applies to metamorphic stones and impact-echo testing at Antiochia ad Cragum is discussed.

5.2.1 Impact-Echo Testing of Metamorphic Stones

Although this study correlates the use of impact-echo testing with theoretical eigenvalue analysis and provides a reliable structural assessment method for rectangular stone blocks, questions regarding its application to metamorphic stones remain unanswered. The specific effect of bedding planes in metamorphic stones should be studied further. The effects that the environment may have on impact-echo testing also remain unanswered. In addition, the straight-line velocity testing conducted was subjective and requires additional consideration. Straight-line velocity testing would best be studied with a different signal analyzer.

Metamorphic stones are often times foliated, meaning that they have layers of varying mineral crystals within their composition (Plummer, Carlson, & McGeary, 2007). This foliation does not always occur in metamorphic rocks, but may potentially be present in the field at Antiochia ad Cragum or other archaeological sites. In order to understand the effects of foliation in specimens, further research will need to be conducted. Studying the wave speeds perpendicular and parallel to the foliation planes may provide an understanding as to the behavior of the specimen. Foliation planes of substantial separation may present premature reflections when conducting impact-echo testing. If foliation planes with substantial separation between players are present, they most likely will manifest themselves in the amplitude spectrum by unusually high peak frequencies. This result will be similar to a thin surface delamination. In addition, the varying minerals in each foliation plane may have different characteristics from one another which may affect wave speed, and as a result, alter the vibration response.

Environmental effects were limited in the laboratory setting and temperatures were monitored as was the temperature of the mortar block during testing. In the field, it is not uncommon for ambient temperatures to exceed 100 degrees Fahrenheit. In such conditions, when ambient temperatures and surface temperatures increase, the wax adhesive may become pliable and the connection between the specimen and the accelerometer may be diminished. Future impact-echo testing conducted in varying environmental conditions should help assess this concern.

As previously mentioned, the straight-line velocity testing conducted in the lab was subjective and contingent upon the sampling interval. The results from the straight-

line velocity tests remain subjective due in part to the sampling interval from the signal analyzer, but also to the availability of accelerometers. In order to completely validate straight-line velocity testing, a new signal analyzer is required with a smaller sampling interval to eliminate intrinsic error. A maximum frequency range of 150 kHz is recommended for the signal analyzer and the accelerometer (Sadri, 2003). In addition, the lack of a spacer device for the accelerometers provides an opportunity for error between tests. Future research regarding the procurement of a spacing device should be conducted. Procuring a completely new impact-echo setup would be beneficial given the recent advancements in stress wave instrumentation. The AndeScope is a stress wave testing setup that can operate in ultrasonic through transmission mode, ultrasonic pulse-echo mode, and impact-echo mode (Sadri, 2003).

While impact-echo testing can provide an adequate assessment for the internal structure of a specimen, additional testing methods can always benefit the assessment, and further the level of the assessments. In particular, GPR testing should be considered in conjunction with impact-echo testing, as it has the ability to identify "hidden voids, inclusions, and flaws…" (Binda, Lualdi, & Saisi, 2008).

5.2.2 Field Testing at Antiochia ad Cragum

In order to reach the goal of structurally analyzing the building stones at the temple in Antiochia ad Cragum, and assuming the existing setup is used in conjunction with the impact-echo manual developed in this research (Appendix E), investigators will need to take special consideration to document the structural composition and integrity of the stones in the field.

Researchers will need to measure each stone's dimensions and input a sufficient amount of information about the specimen's internal properties into RIAP to output predicted responses for comparison. Either the wave speed (C_p) or the specimen's properties (ρ, ν, and E) must be input for the program to function correctly. If the specimen's properties are unknown, the researchers can conduct straight-line velocity tests to determine the P-wave speed. With this information, the researchers will be able to input this data into RIAP and view the predicted response of a solid block through its fundamental modes of vibration. In order to limit the variance between measured properties and measured P-wave speed, a baseline set of results, particular to a sample of specimens, should be conducted if possible (Boothby, Kremer, & Trujillo, 2011).

After satisfactorily determining the predicted response, researchers will need to test the block in traditional impact-echo testing and compare those results with the predicted response. This analysis should be conducted in the field and comparisons drawn in real-time. Researchers will then be able to classify and record the building stones' structural integrities. The determination of each stone's structural integrity will provide the project with illuminating information regarding the restoration possibilities, and the need for structural rehabilitation.

Considering that the bedding planes in metamorphic stones, as seen in the field, were unable to be studied in the lab, special testing should be completed to determine the effect of foliation planes on the stress waves. It is possible for the waves to reflect or split on foliation planes. Research on this topic would provide information beneficial to

the continued use of impact-echo testing as a viable non-destructive testing technique for metamorphic stone specimens.

Existing impact-echo testing equipment when coupled with post-processing imagery can produce spectral tomography. Spectral tomography provides the user with a more detailed map of the internal structure by analyzing prevalent frequencies at different locations and then analyzing each individual test. Those individual analyses are then mapped and a structural assessment grid is developed, providing a map of the structural conditions (Liu & Yeh, 2010). The resulting image gives a detailed view of the internal structure but still relies on the analysis of amplitude spectrums, which are often subjective, as seen in this study.

Another study that utilizes impact-echo methods requires an accelerometer array and provides reconstructed images similar to Liu and Yeh. This method is more focused on the individual discontinuities than an overall assessment (Sridharan, Muralidharan, Balasubramaniam, & Krishnamurthy, 2006). This method is quicker than the spectral tomography method and may provide a more efficient analysis method. Further research into these two methods would further the benefits of the methodology proposed here.

Future research requiring a more detailed internal assessment of stones may want to adopt ultrasonic pulse velocity testing (UPVT). UPVT allows for an internal map of the specimen by measuring travel-time between a transducer and an excitation device (Dilek, 2007). While ultrasonic pulse velocity provides a very detailed assessment of the

internal characteristics of a specimen, it is, at the current time, more expensive than impact-echo testing and more labor intensive.

References

ANSYS, I. (2009). Stuctural Analysis Guide. In I. ANSYS, *ANSYS User's Guide Release 12.1* (pp. 1-117). Canonsburg, Pennsylvania, United States of America: ANSYS, Inc.

ANSYS, I. (2011). ANSYS Mechanical APDL. (13). Canonsburg, Pennsylvania, United States of America. Retrieved 2012

ANSYS, I. (2011). ANSYS Workbench. Canonsburg, Pennsylvania, United States of America. Retrieved 2012

ASTM International. (2008). *Standard Specification for Mortar for Unit Masonry Designation C270-08a.* West Conshohocken: ASTM International.

ASTM International. (2010). *Standard Test Method for Measuring the P-Wave Speed and the Thickness of Concrete Plates Using the Impact-Echo Method Designation C1383-04.* West Conshohocken: ASTM International.

ASTM International. (2010). *Standard Test Method for Static Modulus of Elasticity and Poisson's Ratio of Concrete in Compression Designation C469/C469M-10.* West Conshohocken: ASTM International.

Binda, L., Lualdi, M., & Saisi, A. (2008). Investigation strategies for the diagnosis of historic structures: on-site tests on Avio Castle, Italy and Pisece Castle, Solvenia. *Canadian Journal of Civil Engineering*, 555-566.

Boothby, T., Kremer, P., & Trujillo, N. (2011). Air-Coupled Impact Echo Analysis of Historic Brick Masonry: From Beverly Minster to Wright-Patterson AFB. *Eleventh NAMC*, 1-13.

Carino, N. (2001). The Impact-Echo Method: An Overview. *Stuctures Congress & Exposition* (pp. 1-18). Reston: National Institute of Standards and Technology.

Chopra, A. K. (2007). *Dynamics of Structures Theory and Applications to Earthquak Engineering.* Upper Saddle River, NJ: Pearson Prentice Hall.

Dilek, U. (2007). Ultrasonic Pulse Velocity in Nondestructive Evaluation of Low Quality and Damagned Concrete and Masonry Construction. *Journal of Performance Constructed Facilities*, 337-344.

Erdogmus, E. (2004). *Structural Appraisal of the Florentine Gothic Construction System.* State College: Pennsylvania State University.

Erdogmus, E., Boothby, T. E., & Smith, E. B. (2007). Structural Appraisal of the Florentine Gothic Construction System. *Journal of Architectural Engineering*, 9-17.

Essom Equipment for Engineering. (2007). *MODULI OF ELASTICITY AND POISSON'S RATIO*. Retrieved December 1, 2011, from ESSOM: http://www.essom.com/backend/data-file/engineer/engin23_1.pdf

Hill, M., McHugh, J., & Turner, J. D. (2000). Cross-Sectional Modes in Impact-Echo Testing of Concrete Structures. *Journal of Structural Engineering*, 228.

Hsiao, C., Cheng, C.-C., Liou, T., & Juang, Y. (2008). Detecting Flaws in Concrete Blocks Using the Impact-Echo Method. *NDT & E International*, 98-107.

Krautkramer, J., & Krautkramer, H. (1990). *Ultrasonic Testing of Materials.* New York: Springer-Verlag.

Liu, P.-L., & Yeh, P.-L. (2010). Spectral tomograph of concrete structures based on impact echo depth spectra. *NDT&E International*, 692-702.

PCB Piezotronics. (2002). 352C68 Installation and Operating Manual. In *Model 352C68 ICP Accelerometer* (pp. 1-15). Depew: PCB Group, Inc.

PCB Piezotronics. (2002). 353B33 Installation and Operating Manual. In *Model 353B33 ICP Accelerometer* (pp. 1-15). Depew: PCB Group, Inc.

PCB Piezotronics. (2002). 393A03 Installation and Operating Manual. In *Model 393A03 ICP Accelerometer* (pp. 1-15). Depew: PCB Group, Inc.

PCB Piezotronics. (2007). 086C01 Installation and Operation Manual. In *Model O86C01 Impact Hammer* (pp. 1-13). Depew: PCB Group, Inc.

PCB Piezotronics. (2007). 086D20 Installation and Operatin Manual. In P. Piezotronics, *Model 086D20 Impact Hammer* (pp. 1-13). Depew: PCB Group Inc.

Plummer, Carlson, & McGeary. (2007). Physcial Geology. In Plummer, Carlson, & McGeary, *Physical Geology* (pp. 171-193). New York: McGraw Hill.

Popovics, J. S. (1997). Effects of poisson's ratio on impact-echo test analysis. *Journal of Engineering Mechanics*, 843.

Robison, T. (2010). *Assessment of Nondestructive Testing Methods for Bridge Deck Evaluations.* Laramie: University of Wyoming.

Sadri, A. (2003). Application of impact-echo technique in diagnoses and repair of stone masonry structures. *NDT&E International*, 195-202.

Sansalone, M. J., & Streett, W. B. (1997). *Impact-Echo: Nondestructive Evaluation of Concrete and Masonry.* Ithaca, NY: Bullbrier Press.

SPECMIX. (2011). *Portland Lime & Sand Masonry Mortar.* Mendota Heights: SPECMIX, Inc.

Spectral Dynamics, I. (2001). *SIGLAB User's Guide.* San Jose: Spectral Dynamics, Inc.

Sridharan, C., Muralidharan, A., Balasubramaniam, K., & Krishnamurthy, C. (2006). A simulation study on the impact echo array technique for concrete structure NDT. *Nondestructive Testing and Evaluation*, 123-140.

Tuan, C. Y. (2004). Sympathetic vibration due to co-ordinated crown jumping. *Journal of Sound and Vibration*, 1083-1098.

Appendix A: Supplemental Field Testing Reference Material

Table 22: Typical SIGLAB setup used in field testing

Channel Setup		Coupling	Units	Full Scale
1	Impact Hammer	Bias	890 lb/Volt	±5.0 V
2	Accelerometer	Bias	1.0417 Gs/Volt	±1.25 V
3	Accelerometer	Bias	0.99404 Gs/Volt	±1.25 V

Bandwidth	10 KHz
Record Length	8192
df(frequency resolution)	3.125 Hz

Trigger	Channel 1
Trigger Sensitivity	18%

No Delay	No Reject
No Filter	No Overlap
	Boxcar

Appendix B: Supplemental Lab Testing Reference Material

Table 23: Typical SIGLAB setup used in field testing

Channel Setup		Coupling	Units	Full Scale
1	Impact Hammer	Bias	890 lb/Volt	±10.0 V
2	Accelerometer	Bias	1.0417 Gs/Volt	±2.5 V
			0.99404 Gs/Volt	±2.5 V

Bandwidth	10 KHz
Record Length	8192
df(frequency resolution)	3.125 Hz

Trigger	Channel 1
Trigger Sensitivity	9%

No Delay	Ovld Reject
No Filter	No Overlap
	Boxcar

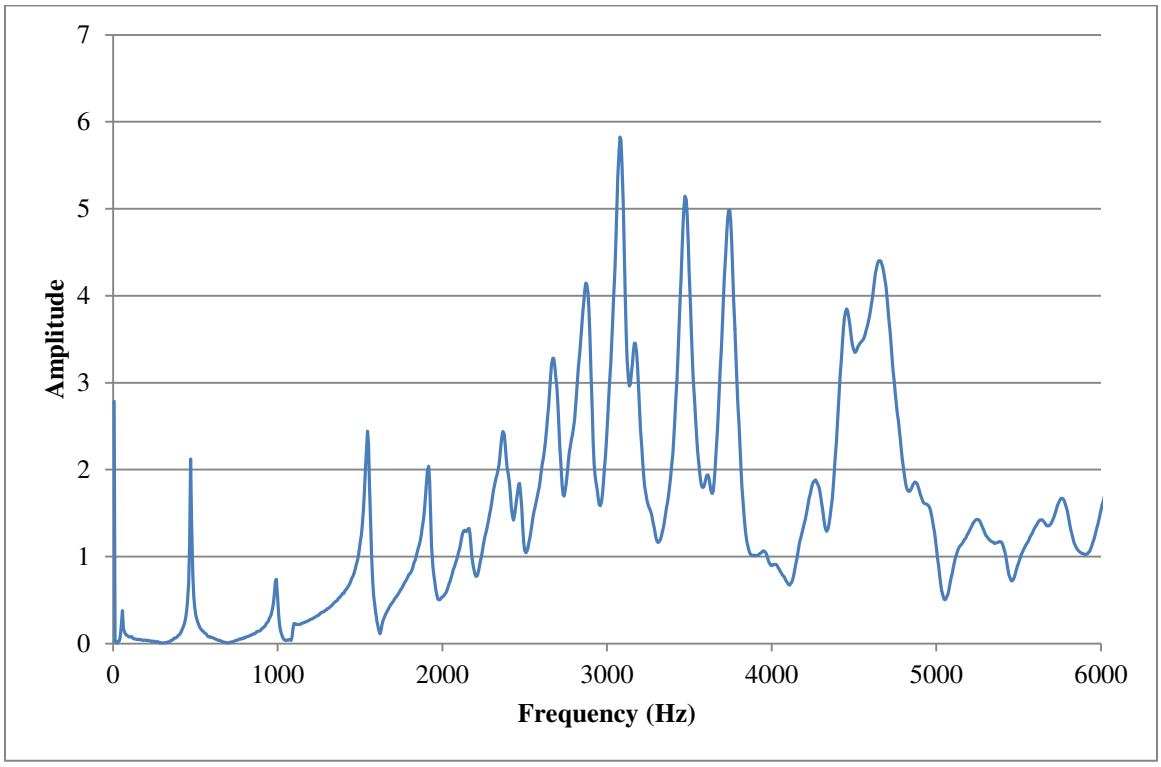

Figure 54: Complete amplitude spectrum for impact-echo lab test 1

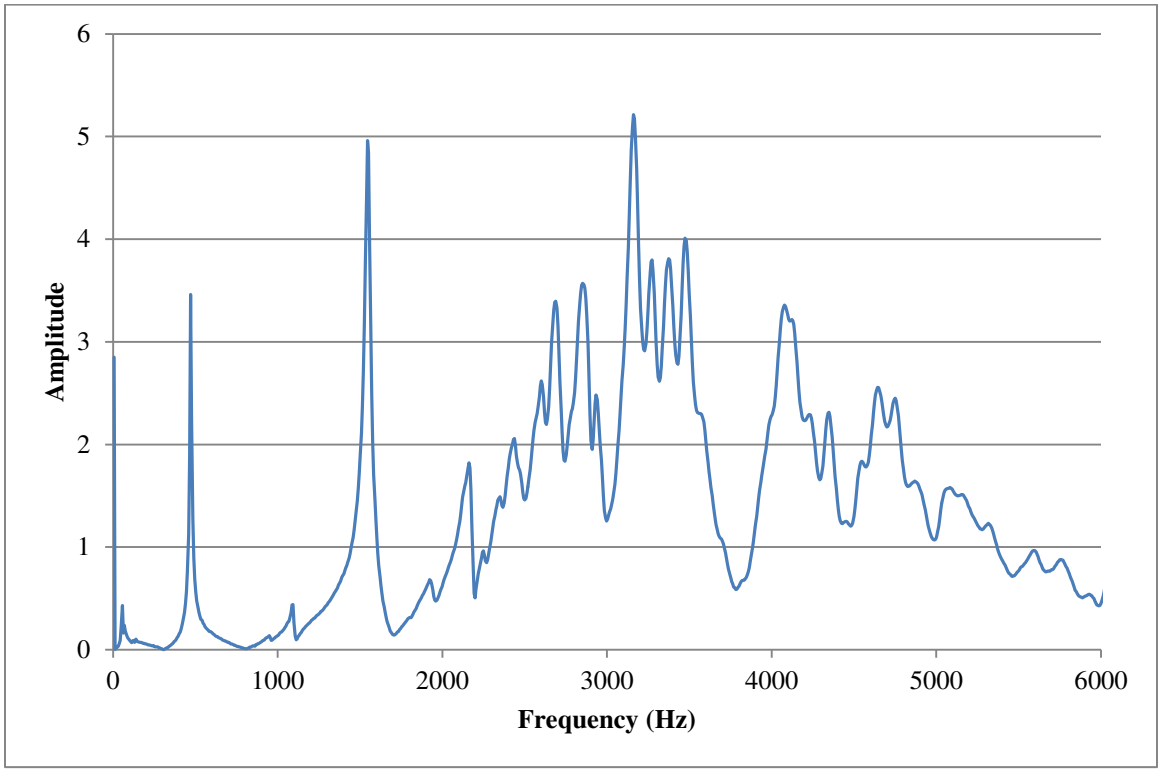

Figure 55: Complete amplitude spectrum for impact-echo lab test 2

Appendix C: ANSYS Participation Factors for Various Aspect Ratios

Table 24: Modal participation factors corresponding to a ratio of 0.6 using a length of 0.05m for element discretization

***** CUMULATIVE	PARTICIPATION RATIO	FACTOR EFF.MASS	CALCULATION	*****	Y	DIRECTION		
MODE	FREQUENCY	PERIOD	PARTIC.FACTOR	RATIO	EFFECTIVE	MASS	MASS	MAG PARTIC. FACTOR
1	0	0	5.1576	0.642549	26.6006	0.177337	0.177337	0
2	0	0	7.6792	0.956705	58.9706	0.570475	0.393138	0
3	0	6655	-8.0268	1	64.4287	1	0.429525	0
4	0	1.17E-03	5.07100E-13	0	2.57E-25	1	1.71E-27	0
5	0	8.37E-04	-3.03E-13	0	9.19E-26	1	6.12E-28	0
6	1270.1	7.87E-04	3.69E-13	0	1.36E-25	1	9.06E-28	3.6858E-13
7	1753.21	5.70E-04	1.72E-15	0	2.94E-30	1	1.96E-32	1.7156E-15
8	1804.3	5.54E-04	2.54E-14	0	6.43E-28	1	4.29E-30	2.5355E-14
9	1889.69	5.29E-04	-9.81E-14	0	9.63E-27	1	6.42E-29	9.8138E-14
10	1905.73	5.25E-04	-4.05E-14	0	1.64E-27	1	1.09E-29	4.0502E-14
11	1998.88	5.00E-04	6.63E-14	0	4.40E-27	1	2.93E-29	6.6334E-14
12	2039.12	4.90E-04	3.35E-14	0	1.12E-27	1	7.47E-30	3.3482E-14
13	2479.94	4.03E-04	5.25E-14	0	2.76E-27	1	1.84E-29	5.2495E-14
14	2503.58	3.99E-04	1.76E-14	0	3.10E-28	1	2.07E-30	1.7616E-14
15	2598.58	3.85E-04	-4.35E-14	0	1.89E-27	1	1.26E-29	4.3472E-14
16	2705.43	3.70E-04	-5.38E-15	0	2.89E-29	1	1.93E-31	5.3789E-15
17	2786.74	3.59E-04	1.97E-14	0	3.87E-28	1	2.58E-30	1.9674E-14
18	3073.63	3.25E-04	4.63E-14	0	2.15E-27	1	1.43E-29	4.6336E-14
19	3266.8	3.06E-04	-9.06E-15	0	8.21E-29	1	5.47E-31	9.0622E-15
20	3270.52	3.06E-04	7.59E-15	0	5.76E-29	1	3.84E-31	7.5877E-15
21	3346.84	2.99E-04	3.43E-14	0	1.18E-27	1	7.84E-30	4.3472E-14
22	3509.04	2.85E-04	1.15E-14	0	1.32E-28	1	8.81E-31	5.3789E-15
23	3661.46	2.73E-04	2.51E-14	0	6.28E-28	1	4.19E-30	2.5063E-14
24	3674.7	2.72E-04	-3.22E-14	0	1.04E-27	1	6.93E-30	3.2231E-14
25	3787.2	2.64E-04	7.51E-15	0	5.64E-29	1	3.76E-31	7.5079E-15
26	3876.02	2.58E-04	-5.62E-15	0	3.16E-29	1	2.10E-31	5.6175E-15
27	3964.46	2.52E-04	-3.73E-15	0	1.39E-29	1	9.26E-32	3.7279E-15
28	4017.61	2.49E-04	7.79E-16	0	6.07E-31	1	4.04E-33	7.7889E-16
29	4051.18	2.47E-04	-9.08E-15	0	8.25E-29	1	5.50E-31	9.0834E-15
30	4074.76	2.45E-04	7.80E-16	0	6.08E-31	1	4.05E-33	7.7976E-16
31	4307.5	2.32E-04	-3.91E-15	0	1.53E-29	1	1.02E-31	3.9144E-15
32	4447.25	2.25E-04	3.21E-15	0	1.03E-29	1	6.87E-32	3.2101E-15
33	4449.86	2.25E-04	9.90E-15	0	9.81E-29	1	6.54E-31	9.9035E-15
34	4466.69	2.24E-04	-7.11E-15	0	5.05E-29	1	3.37E-31	7.1054E-15
35	4572.51	2.19E-04	2.42E-15	0	5.87E-30	1	3.92E-32	2.4234E-15
36	4750.75	2.10E-04	-9.52E-16	0	9.07E-31	1	6.05E-33	9.5236E-16
37	4816.1	2.08E-04	-1.35E-14	0	1.81E-28	1	1.21E-30	1.3456E-14
38	4866.84	2.05E-04	6.51E-16	0	4.24E-31	1	2.83E-33	6.5117E-16
39	5000.77	2.00E-04	-1.30E-15	0	1.70E-30	1	1.14E-32	1.3049E-15
40	5042.27	1.98E-04	6.01E-15	0	3.61E-29	1	2.41E-31	6.0108E-15
41	5063.65	1.97E-04	-2.77E-15	0	7.67E-30	1	5.12E-32	2.7704E-15
42	5196.13	1.92E-04	1.32E-14	0	1.74E-28	1	1.16E-30	1.3174E-14
43	5253.29	1.90E-04	-6.45E-16	0	4.16E-31	1	2.78E-33	6.4532E-16
44	5337.67	1.87E-04	3.50E-15	0	1.23E-29	1	8.17E-32	3.5011E-15
45	5374.36	1.86E-04	-8.29E-15	0	6.87E-29	1	4.58E-31	8.2902E-15
46	5427.56	1.84E-04	5.45E-16	0	2.97E-31	1	1.98E-33	5.447E-16
47	5529.64	1.81E-04	1.71E-15	0	2.94E-30	1	1.96E-32	1.7148E-15
48	5546.6	1.80E-04	-1.05E-15	0	1.09E-30	1	7.30E-33	1.0461E-15
49	5649.91	1.77E-04	1.06E-14	0	1.12E-28	1	7.46E-31	1.0577E-14
50	5811.86	1.72E-04	4.12E-12	0	1.69E-23	1	1.13E-25	4.1156E-12
51	5898.49	1.70E-04	2.55E-12	0	6.51E-24	1	4.34E-26	2.5522E-12
52	6012.68	1.66E-04	1.26E-12	0	1.59E-24	1	1.06E-26	1.2627E-12

Table 25: Modal participation factors corresponding to a ratio of 1.0 using a length of 0.05m for element discretization

***** PARTICIPATION FACTOR CALCULATION ***** Y DIRECTION CUMULATIVE RATIO EFF.MASS								
MODE	FREQUENCY	PERIOD	PARTIC.FACTOR	RATIO	EFFECTIVE	MASS	MASS	MAG PARTIC. FACTOR *Scaled by factor of 100
1	0	0	0	0	0	0.162974	0.162974	0
2	0	0	0	0	0	0.583673	0.420699	0
3	9.35E-05	10695	0	0	0	1	0.416327	0
4	1950.6	5.13E-04	-1.67E-15	1.6688E-15	1.6688E-13	1	3.81E-32	1.67E-13
5	2002.53	4.99E-04	-3.35E-14	3.3463E-14	3.3463E-12	1	1.70E-29	3.35E-12
6	2002.53	4.99E-04	8.55E-15	8.5487E-15	8.5487E-13	1	1.08E-30	8.55E-13
7	2218.63	4.51E-04	6.76E-15	6.7561E-15	6.7561E-13	1	7.30E-31	6.76E-13
8	2403.75	4.16E-04	9.09E-15	9.09E-15	9.09E-13	1	1.32E-30	9.09E-13
9	2602.11	3.84E-04	-2.38E-15	2.3835E-15	2.3835E-13	1	9.09E-32	2.38E-13
10	3104.69	3.22E-04	5.55E-17	5.5511E-17	5.5511E-15	1	1.06E-31	5.55E-15
11	3104.69	3.22E-04	-3.91E-15	3.9083E-15	3.9083E-13	1	7.43E-32	3.91E-13
12	3533.35	2.83E-04	-2.21E-15	2.2066E-15	2.2066E-13	1	3.73E-32	2.21E-13
13	4097	2.44E-04	1.24E-14	1.2386E-14	1.2386E-12	1	2.34E-30	1.24E-12
14	4097	2.44E-04	-5.44E-15	5.4366E-15	5.4366E-13	1	4.07E-31	5.44E-13
15	4166.97	2.40E-04	-3.37E-15	3.3688E-15	3.3688E-13	1	2.86E-31	3.37E-13
16	4360.05	2.29E-04	3.83E-15	3.832E-15	3.832E-13	1	2.71E-31	3.83E-13
17	4437.26	2.25E-04	-6.51E-16	6.5052E-16	6.5052E-14	1	1.61E-32	6.51E-14
18	4870.85	2.05E-04	1.94E-15	1.9394E-15	1.9394E-13	1	3.68E-17	1.94E-13
19	4870.85	2.05E-04	-3.37E-15	3.3688E-15	3.3688E-13	1	2.27E-18	3.37E-13
20	4981.16	2.01E-04	-3.71E-15	3.7054E-15	3.7054E-13	1	2.87E-31	3.71E-13
21	5303.78	1.89E-04	-4.56E-15	4.5554E-15	4.5554E-13	1	1.14E-19	4.56E-13
22	5303.78	1.89E-04	-2.22E-15	2.2204E-15	2.2204E-13	1	3.13E-17	2.22E-13
23	5464.04	1.83E-04	3.34E-15	3.3445E-15	3.3445E-13	1	9.60E-32	3.34E-13
24	5732.76	1.74E-04	4.29E-15	4.2882E-15	4.2882E-13	1	1.98E-31	4.29E-13
25	5768.74	1.73E-04	-3.26E-16	3.2613E-16	3.2613E-14	1	2.91E-30	3.26E-14
26	5768.74	1.73E-04	2.64E-15	2.6368E-15	2.6368E-13	1	2.15E-30	2.64E-13
27	6212.95	1.61E-04	2.49E-15	2.4911E-15	2.4911E-13	1	2.18E-29	2.49E-13
28	6464.57	1.55E-04	2.69E-15	2.6854E-15	2.6854E-13	1	2.88E-29	2.69E-13
29	6534.95	1.53E-04	-3.62E-15	3.6152E-15	3.6152E-13	1	6.15E-30	3.62E-13
30	6534.95	1.53E-04	2.66E-15	2.6576E-15	2.6576E-13	1	4.70E-30	2.66E-13
31	6656.02	1.50E-04	1.15E-15	1.1475E-15	1.1475E-13	1	2.10E-34	1.15E-13
32	6686.27	1.50E-04	1.37E-15	1.3685E-15	1.3685E-13	1	4.11E-31	1.37E-13

Table 26: Modal participation factors corresponding to a ratio of 2.0 using a length of 0.05m for element discretization

***** CUMULATIVE	PARTICIPATION RATIO	FACTOR EFF.MASS	CALCULATION	*****	Y	DIRECTION		
MODE	FREQUENCY	PERIOD	PARTIC.FACTOR	RATIO	EFFECTIVE	MASS	MASS	MAG PARTIC. FACTOR
1	0	0	2.1097	0.192227	4.451	3.56E-02	3.56E-02	0
2	0	0	10.975	1	120.456	0.999259	0.963651	0
3	1.14E-04	8769.1	0.30426	0.027722	9.26E-02	1	7.41E-04	0
4	790.669	1.26E-03	4.23E-14	0	1.79E-27	1	1.43E-29	0
5	1198.1	8.35E-04	3.05E-14	0	9.30E-28	1	7.44E-30	3.0489E-14
6	1353.95	7.39E-04	1.43E-14	0	2.05E-28	1	1.64E-30	1.4315E-14
7	1966.52	5.09E-04	-6.46E-15	0	4.18E-29	1	3.34E-31	6.4631E-15
8	1986.06	5.04E-04	2.02E-14	0	4.09E-28	1	3.27E-30	2.0227E-14
9	2104.3	4.75E-04	-6.47E-15	0	4.18E-29	1	3.35E-31	6.467E-15
10	2170.88	4.61E-04	-3.85E-14	0	1.48E-27	1	1.19E-29	3.8532E-14
11	2218.63	4.51E-04	3.18E-14	0	1.01E-27	1	8.11E-30	3.1833E-14
12	2437.22	4.10E-04	-9.04E-14	0	8.18E-27	1	6.54E-29	9.0421E-14
13	2572.47	3.89E-04	-1.24E-14	0	1.55E-28	1	1.24E-30	1.2441E-14
14	2675.29	3.74E-04	-2.60E-14	0	6.78E-28	1	5.42E-30	2.6033E-14
15	2686.91	3.72E-04	-1.80E-14	0	3.23E-28	1	2.58E-30	1.7961E-14
16	2841.22	3.52E-04	-2.99E-15	0	8.92E-30	1	7.14E-32	2.9872E-15
17	3106.47	3.22E-04	9.49E-15	0	9.01E-29	1	7.21E-31	9.4924E-15
18	3286.93	3.04E-04	3.04E-15	0	9.24E-30	1	7.39E-32	3.0392E-15
19	3527.99	2.83E-04	-1.68E-14	0	2.81E-28	1	2.25E-30	1.6768E-14
20	3595.97	2.78E-04	2.85E-15	0	8.13E-30	1	6.51E-32	2.8519E-15
21	3677.42	2.72E-04	2.23E-15	0	4.99E-30	1	3.99E-32	1.7961E-14
22	3723.61	2.69E-04	-2.78E-15	0	7.70E-30	1	6.16E-32	2.9872E-15
23	3740.34	2.67E-04	2.47E-15	0	6.10E-30	1	4.88E-32	2.4702E-15
24	4071.08	2.46E-04	2.50E-15	0	6.27E-30	1	5.02E-32	2.5049E-15
25	4170.59	2.40E-04	-2.32E-15	0	5.40E-30	1	4.32E-32	2.3245E-15
26	4189.17	2.39E-04	3.92E-16	0	1.54E-31	1	1.23E-33	3.9205E-16
27	4368.05	2.29E-04	-3.60E-15	0	1.29E-29	1	1.04E-31	3.5978E-15
28	4437.26	2.25E-04	-1.32E-15	0	1.74E-30	1	1.39E-32	1.3188E-15
29	4563.26	2.19E-04	3.92E-16	0	1.54E-31	1	1.23E-33	3.9205E-16
30	4740.63	2.11E-04	-1.31E-14	0	1.73E-28	1	1.38E-30	1.3142E-14
31	4808.88	2.08E-04	2.70E-15	0	7.29E-30	1	5.83E-32	2.6992E-15
32	4819.68	2.07E-04	-3.76E-15	0	1.41E-29	1	1.13E-31	3.76E-15
33	4862.83	2.06E-04	7.62E-15	0	5.80E-29	1	4.64E-31	7.6154E-15
34	4864.61	2.06E-04	5.07E-15	0	2.57E-29	1	2.06E-31	5.0741E-15
35	4871.45	2.05E-04	1.80E-15	0	3.25E-30	1	2.60E-32	1.8041E-15
36	5014.33	1.99E-04	-4.28E-15	0	1.83E-29	1	1.47E-31	4.283E-15
37	5179.82	1.93E-04	2.89E-15	0	8.37E-30	1	6.69E-32	2.8926E-15
38	5226.47	1.91E-04	-1.15E-14	0	1.31E-28	1	1.05E-30	1.1456E-14
39	5432.95	1.84E-04	-1.63E-15	0	2.67E-30	1	2.14E-32	1.6341E-15
40	5529.99	1.81E-04	3.68E-15	0	1.36E-29	1	1.09E-31	3.6846E-15
41	5563.85	1.80E-04	-8.61E-15	0	7.42E-29	1	5.93E-31	8.6112E-15
42	5601.9	1.79E-04	1.30E-15	0	1.69E-30	1	1.35E-32	1.301E-15
43	5652.68	1.77E-04	-1.99E-15	0	3.95E-30	1	3.16E-32	1.988E-15
44	5730.75	1.75E-04	-1.68E-15	0	2.82E-30	1	2.26E-32	1.6792E-15
45	5944.68	1.68E-04	-6.59E-15	0	4.34E-29	1	3.47E-31	6.5889E-15
46	6039.04	1.66E-04	4.01E-15	0	1.61E-29	1	1.28E-31	4.0072E-15

Appendix D: ANSYS Participation Factors for Mortar Block Model

Table 27: Modal participation factors corresponding to the mortar block finite element model using a length of 0.05m for element discretization

***** CUMULATIVE	PARTICIPATION RATIO	FACTOR EFF.MASS	CALCULATION	*****	Y	DIRECTION		
MODE	FREQUENCY	PERIOD	PARTIC.FACTOR	RATIO	EFFECTIVE	MASS	MASS	MAG PARTIC. FACTOR
1	0	0	5.6707	0.975637	32.1565	0.464734	0.464734	5.6707
2	0.000554253	1804.2	1.804	0.310374	3.25435	0.511767	0.0470327	1.804
3	0.00125681	795.67	5.8123	1	33.7825	1	0.488233	5.8123
4	1739.07	0.00057502	4.7027E-13	0	2.21157E-25	1	3.19621E-27	4.7027E-13
5	1856.47	0.00053866	-6.6453E-13	0	4.41597E-25	1	6.38207E-27	6.6453E-13
6	2072.95	0.0004824	-6.5475E-13	0	4.28703E-25	1	6.19573E-27	6.5475E-13
7	2073.83	0.0004822	-7.283E-15	0	5.30424E-29	1	7.66581E-31	7.283E-15
8	2291.28	0.00043644	-8.5752E-14	0	7.35339E-27	1	1.06273E-28	8.5752E-14
9	2529.62	0.00039532	1.1391E-13	0	1.2975E-26	1	1.87518E-28	1.1391E-13
10	2934.93	0.00034072	3.9401E-14	0	1.55244E-27	1	2.24363E-29	3.9401E-14
11	2947.39	0.00033928	-1.4075E-13	0	1.98105E-26	1	2.86306E-28	1.4075E-13
12	3301.32	0.00030291	2.9692E-13	0	8.8162E-26	1	1.27414E-27	2.9692E-13
13	3885.65	0.00025736	6.8089E-14	0	4.63611E-27	1	6.70022E-29	6.8089E-14
14	3932.74	0.00025428	9.0103E-14	0	8.11858E-27	1	1.17332E-28	9.0103E-14
15	3935.68	0.00025409	-9.9774E-15	0	9.95477E-29	1	1.43869E-30	9.9774E-15
16	4097.58	0.00024405	1.6638E-13	0	2.76828E-26	1	4.00079E-28	1.6638E-13
17	4318.2	0.00023158	1.4772E-13	0	2.18199E-26	1	3.15346E-28	1.4772E-13
18	4370.51	0.00022881	9.2492E-14	0	8.55475E-27	1	1.23635E-28	9.2492E-14
19	4735.77	0.00021116	3.1391E-14	0	9.85369E-28	1	1.42408E-29	3.1391E-14
20	4873.53	0.00020519	8.7165E-15	0	7.59778E-29	1	1.09805E-30	8.7165E-15
21	4975.26	0.00020099	-3.1221E-15	0	9.74731E-30	1	1.40871E-31	3.1221E-15
22	5129.61	0.00019495	8.5019E-14	0	7.22831E-27	1	1.04465E-28	8.5019E-14
23	5141.93	0.00019448	4.7389E-14	0	2.24571E-27	1	3.24555E-29	4.7389E-14
24	5415.09	0.00018467	-2.9737E-14	0	8.84267E-28	1	1.27796E-29	2.9737E-14
25	5425.59	0.00018431	1.2219E-13	0	1.49313E-26	1	2.1579E-28	1.2219E-13
26	5536.72	0.00018061	3.0061E-14	0	9.03652E-28	1	1.30598E-29	3.0061E-14
27	5912.52	0.00016913	2.5963E-16	0	6.74055E-32	1	9.74161E-34	2.5963E-16

Table 28: Modal participation factors corresponding to a ratio of 0.89 using a length of 0.025m for element discretization

***** PARTICIPATION FACTOR CALCULATION ***** Y DIRECTION CUMULATIVE RATIO EFF.MASS								
MODE	FREQUENCY	PERIOD	PARTIC.FACTOR	RATIO	EFFECTIVE	MASS	MASS	MAG PARTIC. FACTOR
1	0	0	1.7435	0.218863	3.03991	4.39E-02	4.39E-02	1.7435
2	2.67E-04	3746	7.9663	1	63.4623	0.961106	0.917172	7.9663
3	3.90E-04	2565.2	1.6405	0.205929	2.69122	1	3.89E-02	1.6405
4	1739.07	5.75E-04	2.39E-13	0	5.74E-26	1	8.29E-28	2.3949E-13
5	1856.48	5.39E-04	2.65E-13	0	7.00E-26	1	1.01E-27	2.645E-13
6	2072.95	4.82E-04	2.97E-13	0	8.81E-26	1	1.27E-27	2.9689E-13
7	2073.83	4.82E-04	1.41E-13	0	1.99E-26	1	2.88E-28	1.4109E-13
8	2291.28	4.36E-04	7.45E-14	0	5.55E-27	1	8.02E-29	7.4512E-14
9	2529.63	3.95E-04	1.09E-13	0	1.18E-26	1	1.71E-28	1.0877E-13
10	2934.94	3.41E-04	-2.84E-15	0	8.05E-30	1	1.16E-31	2.8371E-15
11	2947.39	3.39E-04	9.00E-14	0	8.10E-27	1	1.17E-28	8.9999E-14
12	3301.36	3.03E-04	3.71E-14	0	1.37E-27	1	1.98E-29	3.7051E-14
13	3885.69	2.57E-04	2.99E-14	0	8.94E-28	1	1.29E-29	2.9907E-14
14	3932.8	2.54E-04	-3.05E-14	0	9.29E-28	1	1.34E-29	3.0483E-14
15	3935.71	2.54E-04	1.31E-14	0	1.71E-28	1	2.47E-30	1.3079E-14
16	4097.62	2.44E-04	-3.83E-14	0	1.47E-27	1	2.12E-29	3.828E-14
17	4318.27	2.32E-04	-4.59E-14	0	2.11E-27	1	3.05E-29	4.5904E-14
18	4370.52	2.29E-04	-7.23E-14	0	5.23E-27	1	7.55E-29	7.2289E-14
19	4735.91	2.11E-04	9.10E-15	0	8.28E-29	1	1.20E-30	9.1004E-15
20	4873.57	2.05E-04	3.17E-16	0	1.01E-31	1	1.45E-33	3.1702E-16
21	4975.36	2.01E-04	-2.17E-15	0	4.73E-30	1	6.83E-32	2.1745E-15
22	5129.68	1.95E-04	-8.31E-15	0	6.90E-29	1	9.98E-31	8.308E-15
23	5142.01	1.94E-04	1.45E-14	0	2.10E-28	1	3.04E-30	1.4498E-14
24	5415.27	1.85E-04	-1.96E-15	0	3.85E-30	1	5.57E-32	1.9633E-15
25	5425.88	1.84E-04	7.52E-15	0	5.65E-29	1	8.17E-31	7.5166E-15
26	5536.83	1.81E-04	-5.53E-15	0	3.06E-29	1	4.42E-31	5.5303E-15
27	5912.93	1.69E-04	1.93E-11	0	3.72E-22	1	5.38E-24	1.9287E-11
28	6020.1	1.66E-04	-3.04E-11	0	9.21E-22	1	1.33E-23	3.0354E-11
29	6235.7	1.60E-04	6.43E-11	0	4.14E-21	1	5.98E-23	6.4341E-11
30	6306.34	1.59E-04	2.97E-12	0	8.81E-24	1	1.27E-25	2.9683E-12
31	6327.21	1.58E-04	2.97E-13	0	8.81E-26	1	1.27E-27	2.9688E-13
32	6458.49	1.55E-04	-1.53E-12	0	2.34E-24	1	3.38E-26	1.5282E-12
33	6633.9	1.51E-04	-2.16E-12	0	4.66E-24	1	6.73E-26	2.1583E-12
34	6773.38	1.48E-04	1.12E-11	0	1.26E-22	1	1.82E-24	1.123E-11
35	6943.94	1.44E-04	3.64E-13	0	1.33E-25	1	1.92E-27	3.6425E-13
36	6978.67	1.43E-04	1.77E-12	0	3.13E-24	1	4.52E-26	1.7691E-12
37	6995.68	1.43E-04	-9.31E-13	0	8.67E-25	1	1.25E-26	9.3104E-13

Table 29: Modal participation factors corresponding to a ratio of 0.89 using a length of 0.025m for element discretization

***** PARTICIPATION FACTOR CALCULATION ***** Y DIRECTION CUMULATIVE RATIO EFF.MASS								
MODE	FREQUENCY	PERIOD	PARTIC.FACTOR	RATIO	EFFECTIVE	MASS	MASS	MAG PARTIC. FACTOR
1	0	0	5.9708	1	35.6507	5.15E-01	5.15E-01	597.08
2	8.27E-05	12097	1.747	0.292596	3.05215	0.559343	0.0441104	174.7
3	1.36E-04	7331.5	5.5218	0.924803	30.4906	1	4.41E-01	552.18
4	1739.11	5.75E-04	2.79E-14	0	7.76E-28	1	1.12E-29	2.786E-12
5	1856.51	5.39E-04	1.22E-14	0	1.49E-28	1	2.15E-30	1.2199E-12
6	2072.95	4.82E-04	-1.67E-14	0	2.78E-28	1	4.02E-30	1.6685E-12
7	2073.92	4.82E-04	2.86E-14	0	8.20E-28	1	1.19E-29	2.8644E-12
8	2291.25	4.36E-04	-5.09E-15	0	2.59E-29	1	3.75E-31	5.0931E-13
9	2529.64	3.95E-04	4.55E-15	0	2.07E-29	1	2.99E-31	4.5484E-13
10	2935.06	3.41E-04	-2.98E-15	0	8.86E-30	1	1.28E-31	2.9768E-13
11	2947.44	3.39E-04	-1.31E-14	0	1.72E-28	1	2.49E-30	1.3117E-12
12	3301.84	3.03E-04	4.07E-15	0	1.66E-29	1	2.40E-31	4.0731E-13
13	3886.32	2.57E-04	-2.95E-15	0	8.70E-30	1	1.26E-31	2.949E-13
14	3933.67	2.54E-04	-7.61E-15	0	5.78E-29	1	8.36E-31	7.605E-13
15	3936.18	2.54E-04	-1.11E-15	0	1.24E-30	1	1.79E-32	1.112E-13
16	4098.2	2.44E-04	7.63E-16	0	5.83E-31	1	8.42E-33	7.6328E-14
17	4319.44	2.32E-04	-1.04E-15	0	1.07E-30	1	1.55E-32	1.0365E-13
18	4370.73	2.29E-04	5.07E-17	0	2.57E-33	1	3.72E-35	5.0741E-15
19	4737.96	2.11E-04	8.88E-16	0	7.89E-31	1	1.14E-32	8.8818E-14
20	4874.07	2.05E-04	-1.86E-15	0	3.45E-30	1	4.99E-32	1.8579E-13
21	4976.75	2.01E-04	1.48E-15	0	2.21E-30	1	3.19E-32	1.4849E-13
22	5130.81	1.95E-04	-2.38E-15	0	5.66E-30	1	8.19E-32	2.38E-13
23	5143.11	1.94E-04	3.40E-15	0	1.16E-29	1	1.67E-31	3.4018E-13
24	5417.75	1.85E-04	2.45E-15	0	5.98E-30	1	8.65E-32	2.446E-13
25	5429.96	1.84E-04	2.12E-16	0	4.48E-32	1	6.47E-34	2.1164E-14
26	5538.45	1.81E-04	9.58E-16	0	9.17E-31	1	1.33E-32	9.5757E-14
27	5919.12	1.69E-04	-8.78E-16	0	7.72E-31	1	1.12E-32	8.7842E-14
28	6024.75	1.66E-04	1.84E-15	0	3.38E-30	1	4.89E-32	1.8388E-13
29	6241.22	1.60E-04	4.65E-16	0	2.16E-31	1	3.12E-33	4.6491E-14
30	6307.27	1.59E-04	1.07E-16	0	1.14E-32	1	1.64E-34	1.0669E-14
31	6336.1	1.58E-04	-2.77E-15	0	7.65E-30	1	1.11E-31	2.7651E-13
32	6463.55	1.55E-04	-1.97E-15	0	3.87E-30	1	5.59E-32	1.9672E-13
33	6635.38	1.51E-04	2.50E-16	0	6.27E-32	1	9.07E-34	2.5045E-14
34	6781.65	1.47E-04	-1.60E-15	0	2.57E-30	1	3.71E-32	1.6029E-13
35	6951.96	1.44E-04	-5.38E-16	0	2.89E-31	1	4.18E-33	5.3776E-14
36	6982.32	1.43E-04	1.91E-16	0	3.64E-32	1	5.26E-34	1.9082E-14

Appendix E: Impact-Echo Testing Reference Manual

Impact-Echo testing procedure based on known specimen properties

1. Document the environmental conditions, specify a block identification, and sketch the block
2. Determine the ideal location for testing considering surface roughness and location on the specimen
3. Clear the surface of debris that may affect the impact-echo test
4. Connect accelerometers into signal analyzer
5. Connect impact-hammer into signal analyzer
6. Set sensitivities for each instrument according to the manufacturer's recommendation and specify the impact-hammer as the triggering mechanism
7. Set desired bandwidth to ensure adequate sampling frequency and select record length
8. Attach accelerometer to specimen
    a. If applying an accelerometer with adhesive, ensure adequate adhesive is applied and slide the accelerometer into place.
    b. Do not slam the accelerometer onto the specimen, this can damage the accelerometer
9. Sketch test setup and record location of testing
10. Perform impact-echo test with a minimum of 5-test averaging by impacting the specimen with the impact hammer
11. Ensure no overloading of the instruments was encountered

12. Analyze coherence graph to ensure reliable data
13. Analyze response spectrum and record observed modes
14. Input dimensions and specimen properties into RIAP.
15. Compare recorded modes with the expected response spectrum from RIAP
16. Make structural assessment conclusions based on general trends between the expected response and the experimental response.

Impact-Echo testing procedure based on P-wave speed measurement

1. Document the environmental conditions, specify a block identification, and sketch the block
2. Determine the ideal location for testing considering surface roughness and location on the specimen
3. Clear the surface of debris that may affect the impact-echo test
4. Connect accelerometers into signal analyzer
5. Connect impact-hammer into signal analyzer
6. Set sensitivities for each instrument according to the manufacturer's recommendation and specify the impact-hammer as the triggering mechanism
7. Set desired bandwidth to ensure adequate sampling frequency and select record length
8. Attach accelerometers to specimen 300 mm apart
    a. If applying accelerometers with adhesive, ensure adequate adhesive is applied and slide the accelerometer into place.
    b. Do not slam the accelerometer onto the specimen, this can damage the accelerometer
9. Sketch test setup and record location of testing
10. Impact the specimen at least 150mm from the first accelerometer
11. Perform individual tests with one impact per test and save the time-series data
12. Repeat step 11 for desired number of tests

13. Analyze time series data and determine P-wave speed according to ASTM C1383-04 for every test and average those results

Now that P-wave speeds have been determined, conduct impact-echo tests:

14. Adjust sensitivities for each instrument according to the manufacturer's recommendation and specify the impact-hammer as the triggering mechanism
15. Adjust desired bandwidth to ensure adequate sampling frequency and select record length
16. Adjust accelerometer location for an impact-echo test
17. Sketch test setup and record location of testing
18. Perform impact-echo test with a minimum of 5-test averaging by impacting the specimen with the impact hammer
19. Ensure no overloading of the instruments was encountered
20. Analyze coherence graph to ensure reliable data
21. Analyze response spectrum and record observed modes
22. Input average P-wave speed and dimensions into RIAP.
23. Compare recorded modes with the expected response spectrum from RIAP
24. Make structural assessment conclusions based on general trends between the expected response and the experimental response.

Optional verification:

25. Validate P-wave speed by assuming material properties for the specific specimen and compared the calculated P-wave speed with the measured P-wave speed.

26. Calculate material properties by fixing the values of 2 properties (either ρ, ν, or E) and then varying one property until the calculated P-wave speed correlates with the measured average P-wave speed from straight line velocity tests

Specimen depth determination:

1. Complete steps 1-21 from *Impact-Echo testing procedure based on P-wave speed measurement*
2. Insert the primary mode into the fundamental frequency impact-echo equation (Equation 7 Page 12), calculate the β, based on Table 1, insert the P-wave speed, and solve for D.

$$f = \beta \frac{C_p}{2D}$$